

The irradiated atmospheres of brown dwarf companions to white dwarf stars

Emma S. Longstaff

Supervisors:

Sarah Casewell

Graham Wynn

Thesis to be submitted for the degree of
Doctor of Philosophy
at the University of Leicester.

X-ray & Observational Astronomy Group
Department of Physics and Astronomy
University of Leicester

November 29, 2018

Abstract

Currently there are 1000's of known exoplanets, many of which are hot-jupiters (Jupiter-like planets close in to their host star), but very few have had their atmospheres characterised. The study of close non-interacting white dwarf - brown dwarf binaries offers a unique opportunity to observe a planet-like atmosphere without the observational challenges faced when investigating exo-atmospheres. In this work I investigate two systems: WD0137-349 and NLTT5306. The former displays irradiation induced metal emission lines in a substellar atmosphere. I investigated the lines strengths of the $H\alpha$ and Ca II line and found these to vary with orbital phase and almost completely disappear on the dark-side of the brown dwarf; implying that heat redistribution around this tidally locked companion is likely to be poor. replication of this result will be necessary in future planetary atmosphere models. NLTT6306 is almost identical to WD0137-349 in component mass and orbital period, the main difference being the age and temperature of the white dwarf primary. This system however, is very different. NLTT5306 displays $H\alpha$ emission and Na I absorption associated with the white dwarf which indicates accretion is happening. However, there are no high energy emissions, Zeeman splitting, or evidence of a disc. An X-ray non-detection gives a maximum accretion rate of $2 \times 10^{-15} M_{\odot} \text{ yr}^{-1}$ which would only require a magnetic field of 0.45 kG to prevent a disc from forming whilst still too low produce detectable Zeeman splitting. I have concluded that the observations can be explained by a light wind from the brown dwarf being magnetically funnelled onto the white dwarf surface. Finally, I have analysed Gemini near-infrared spectra from 8 white dwarfs with photometrically confirmed infrared excesses. I compared the spectra to composite models and I was able to spectroscopically confirm 3 new white dwarf - brown dwarf binaries.

Contents

1	Introduction	1
1.1	White dwarfs	4
1.2	Brown dwarfs	5
1.3	Stellar binary evolution	11
1.4	Using brown dwarfs as exoplanet analogues.	12
1.5	Known close white dwarf – brown dwarf binary systems	13
1.5.1	Non-interacting	14
1.5.2	Interacting	17
1.6	Aims and objectives going forward	25
2	Instrumentation	26
2.1	XSHOOTER	27

2.2	Gemini Near-Infrared Spectrograph	27
2.3	Neil Gehrels Swift Telescope	30
3	Data reduction and analysis techniques	31
3.1	Spectroscopic reduction techniques	31
3.1.1	Gasgano	34
3.1.2	SpeXTool	36
3.2	Data Analysis	37
3.2.1	MOLLY	38
3.2.2	Initial processing	38
3.2.3	Measuring radial velocity	40
3.2.4	Refining the ephemeris	45
3.2.5	Measuring equivalent width	46
3.2.6	Modelling white dwarf spectra using TLUSTY	48
4	Emission lines in the atmosphere of the irradiated brown dwarf: WD0137-349B	51
4.1	Abstract	52
4.2	Introduction	52
4.3	Observations	53
4.4	Data Reduction	53

4.5	Data Analysis	54
4.6	Results	54
4.6.1	Spectral features	56
4.7	Comparison to similar systems	61
4.7.1	Low mass companions	61
4.7.2	Emission from non-irradiated brown dwarfs	62
4.8	Discussion	63
4.8.1	Characterising the line profiles	66
4.8.2	Heat redistribution of irradiated sub-stellar objects	71
4.9	Conclusion	72
5	Possible accretion in NLTT5306	74
5.1	Introduction	74
5.2	Data from XSHOOTER	75
5.2.1	Observations	75
5.2.2	Data reduction and analysis	76
5.2.3	Refinement of the ephemeris	76
5.2.4	Measuring H α emission line strength	79
5.3	Data from <i>Swift</i>	81

5.3.1	ToO observations and analysis	81
5.3.2	GI observations and analysis	83
5.3.3	Modelling the spectra and photometry	85
5.3.4	Placing an upper limit on the accretion rate	86
5.3.5	Accretion mechanisms	88
5.4	Discussion	91
5.4.1	Accretion rate	91
5.5	Conclusions	93
6	Spectroscopically classifying white dwarf + brown dwarf candidate systems using the Gemini near-infrared spectrograph	94
6.1	Introduction	95
6.1.1	Discovering white dwarfs with infrared excesses	95
6.2	Data reduction	98
6.3	Data Analysis	99
6.4	Results & Discussion	102
6.5	Conclusion	114
7	Conclusions	115
7.1	Chapter 4: Emission lines in WD0137-349B	116

7.1.1	Conclusions	116
7.1.2	Future Work	117
7.2	Chapter 5: Possible accretion in NLTT5306	117
7.2.1	Conclusions	118
7.2.2	Future Work	119
7.3	Chapter 6: New white dwarf - brown dwarf systems	119
7.3.1	Conclusions	120
7.3.2	Future Work	120
7.4	Summary	121

List of Figures

- 1.1 An illustration of a Hertzsprung-Russell diagram showing how a solar mass main sequence star evolves into a white dwarf. The number denote key points in a main sequence stars' evolution. Main sequence hydrogen burning (1), exhausting all hydrogen in the core, and the beginning of hydrogen shell burning (2), the ignition of helium burning in the core known, as the Helium Flash (3), helium shell burning (4–5), expulsion of outer layers by a stellar wind forming a planetary nebula (5–6), core of the star cools to a white dwarf (7). 6

- 1.2 This figure has been taken from Helling & Casewell (2014). It shows the near-infrared spectra of M-dwarfs through to Y-dwarfs for a wavelength range of 1 – 4 μm . Each spectrum has been normalised and offset by a constant to better display the spectral features caused by the presence of atoms and molecules listed along the top of the plot. 9

- 1.3 This plot has been taken from Dieterich et al. (2014). It shows the low-mass end of the main sequence in the Hertzsprung-Russell diagram with temperature decreasing from 3000 K to 1500 K. It includes late M–dwarfs through to mid-L–dwarfs whose luminosities decrease with decreasing temperature. 10

1.4	This shows the progression of CE evolution. As the star evolves off the main sequence (a) and moves up the red giant branch it will overflow its Roche lobe leading to dynamically unstable mass transfer. The brown dwarf, unable to accept all the material, is engulfed by the stars outer layers, forming a contact binary, and the drag causes it to spiral in and surrender its orbital energy to the gaseous envelope. The envelope is then expelled into space leaving a close white dwarf – brown dwarf binary (c).	12
2.1	A schematic overview of the XSHOOTER instrument mounted at the VLT-UT3 telescope in Paranal, Chile. This illustrates the three arms: UVB, VIS, and NIR and how incoming lights is split to provide simultaneous observations in all three arms, thus covering a wavelength range of $0.3 - 2.4\mu\text{m}$. (Credit: ESO, https://www.eso.org/sci/facilities/paranal/instruments/xshooter/overview.html)	28
2.2	A schematic overview of the Gemini Near-Infrared Spectrograph (GNIRS) instrument mounted at Mauna Kea, Hawai'i. This illustrates how the incoming light passes through a filter and slit before reaching the detector.	29
3.1	UVB (top) and VIS (bottom) XSHOOTER reduced spectra before being normalised. The red sections were masked out when fitting the polynomial (green) that was used to normalise the data.	39
3.2	NIR XSHOOTER spectra before being normalised. The large number of bad pixels made clear in this plot are due to the bad pixels in the original frame. Their presence does not affect the results of this work. This plot is to illustrate the regions masked out to fit a polynomial.	40
3.3	An example of an emission line (grey) being red- and blue-shifted about its rest wavelength (black vertical line) and the models fitted to each line to measure radial velocity (red).	41

3.4	Each horizontal slice is one spectrum and by stacking these slices above one another one can see how the spectral features move with time; this is known as trailing. This trail shows the $H\alpha$ line, the absorption feature is black and the emission feature is white. The x-axis is radial velocity with 0 centred on the central wavelength of the $H\alpha$ line at 6562.76 \AA	42
3.5	The three Gaussians required to model the $H\alpha$ absorption line with the total model over-plotted (black). The $H\alpha$ line has this shape because the line has been pressure broadened within the white dwarf atmosphere.	43
3.6	Three example fits of the full model of the $H\alpha$ line. Each fit includes the three Gaussians from Figure 3.5 with the addition of a fourth Gaussian for the emission line.	45
3.7	Upper: An example spectrum of a Ca II emission line (grey) that has been normalised to put the continuum flux level at 1 and this has been highlighted in red. This plot demonstrates the area that is determined when calculating the equivalent width of a line.	47
3.8	The original spectrum (red) centred on the $H\alpha$ line with the fit to just the absorption feature (black). This fit was subtracted from the total spectrum to leave only the emission feature (blue).	47
3.9	Example white dwarf models created using TLUSTY and synthesised with SYN-SPEC. The top plot shows models with consistent effective temperature and different surface gravities. The bottom plot shows models with the same surface gravity but different temperatures. The y-axis for both plots is in $f\nu$ units which means energy per frequency. the inserts in both plots highlight the results of varying the surface gravity and temperature, respectively.	49

4.1	The measured radial velocity values of the H α emission (red '+') and absorption (black 'x'). These have been fit with equation (5.1) using the best fitting values for γ and K from tables 4.3 – 4.5.	58
4.2	Trailed spectra demonstrating the binary nature of the system. Left: The H α emission (white) and absorption (black) line demonstrating the emission line is in anti-phase with the absorption feature. Right: The 8662.14 Å Ca II emission line (white). The Ca II emission closely resembles the H α emission indicating they originate from the same place: the brown dwarf.	61
4.3	Chemical equilibrium results for a Drift-Phoenix model atmosphere ($T_{\text{eff}} = 2000$ K, $\log(g) = 5.0$, solar metallicity) with an artificially added chromosphere-like temperature increase for atmospheric heights $z < 10^4$ cm (z decreases outwards). The top panel shows the temperature of the brown dwarf (black, steeper line) due to a chromosphere or external energy input and the degree of thermal ionisation (blue, flatter line) that these higher temperatures induce. The second, third, and fourth panels show the chemical equilibrium results plotted for a selected number of atoms (solid lines) and ions (dashed lines) each with a corresponding label. As expected, the inner part of the atmosphere is dominated by the atomic form of an element but an outward increasing temperature (e.g. resulting from a chromosphere or corona) will cause different ions to appear height-dependently.	65
4.4	Equivalent width of the H α emission (red '+') and the Ca II 8662 Å line (black 'x') as a function of phase. The horizontal black line at an equivalent width of 0 Å marks the point where a spectral feature is no longer present. The strength of the emission lines varies with orbital phase, going to zero at $\phi=0.5$ i.e. when the dark-side of the brown dwarf is in view. The data has been duplicated over two phases.	67

4.5	A comparison of our measured equivalent widths to three other brown dwarfs that display this type of emission and whose equivalent width had been measured. V471 Tau has also been included as it has day (red, lower) and night (blue, higher) side equivalent widths with a clear phase dependency similar to WD0137-349B.	68
4.6	The FWHM of the H α line (red '+') and the Ca II line (black 'x') with respect to phase. The horizontal lines indicate the FWHM calculated from the $v\sin(i)$ for each line in the corresponding colour. The strength of the Ca II line between $\phi = 0.35 - 0.7$ was too weak to get a reliable FWHM measurement. This has been duplicated over two orbits for clarity.	69
4.7	Left: A trail plot observed spectra centred on the Ca II 8662 Å emission line with orbital phase going from 0 to 1 vertically and radial velocity on the x-axis. Right: Simulated data trail plots of the Ca II 8662 Å emission line. The black bar on the left plot is due to bad pixels that were masked out of that spectrum, they do not affect the data in any way.	70
5.1	Radial velocity measurements made using MOLLY <i>mgfit</i> routine have been fit using Equation 5.1 with best fitting values listed in Table 5.2. The H α absorption (top) with Steele et al. (2013) data folded onto the new ephemeris (red '+'), H α emission (middle), and Na I absorption (bottom) lines are all present in the NLTT5306 atmosphere.	78
5.2	Left: The trailed spectrum of the H α line. The emission (white) traces the path of the absorption (dark grey). Right: The trailed spectrum of the 5889.95 Å and 5895.92 Å Na I lines.	80

5.3	Left shows the original spectrum (red) with the fit to the absorption feature (black) that was subtracted to leave only the emission feature (blue). Right shows how the $H\alpha$ measured equivalent widths vary with phase a phase shift of ~ 0.25 can clearly be seen. This has been duplicated over two phases with the duplicate data plotted in grey.	81
5.4	The white dwarf model and the three filter profiles uvw1 (red), uvm2 (blue), and uvw2 (yellow). SDSS photometry has been plotted in blue (+) in the five filter bands, u , g , r , i , and z	82
5.5	Example image of the ToO reduction showing the selection of the target and a background region.	83
5.6	Measured magnitudes in three filters: uvw1, uvm2, and uvw2. Observations were taken covering as much of an orbit as possible. The horizontal lines are the average of the data points in each filter.	86
5.7	A composite of the white dwarf model spectrum (blue line) and a sequence of brown dwarf template spectra from L3 – L7 (labelled). Swift photometry is plotted in purple (+), SDSS <i>ugriz</i> in blue (x), UKIDSS Y , J , H and K in green (*) and Wise W1 and W2 in red (o).	87
6.1	This shows the colour-colour plots illustrating the location of the SDSS spectroscopic objects; DA white dwarfs are shown in blue. The table beneath the plot lists the polynomials used to perform the colour cuts to select white dwarfs; these are overlaid as red lines. Credit: DA white dwarfs in Sloan Digital Sky Survey Data Release 7 and a search for infrared excess emission. Mon Not R Astron Soc. 2011;417(2):1210-1235. doi:10.1111/j.1365-2966.2011.19337.x	97

6.2	A DBA white dwarf model (blue) and composite white dwarf - brown dwarf models for three spectral types, L3 (purple), L4 (yellow), and L5 (pink). The observed photometry from SDSS and UKIDSS are plotted in red and the SDSS visible and GNIRS near-infrared spectra are plotted in grey.	105
6.3	A DA white dwarf model (blue) and composite white dwarf - brown dwarf models for three spectral types, L5 (pink), L6 (yellow), and L7 (purple). The observed photometry from SDSS and UKIDSS are plotted in red and the SDSS visible and GNIRS near-infrared spectra are plotted in grey.	106
6.4	A DA white dwarf model (blue) and composite white dwarf - brown dwarf models for three spectral types, L3 (purple), L4 (yellow), and L6 (pink). The observed photometry from SDSS and UKIDSS are plotted in red and the SDSS visible and GNIRS near-infrared spectra are plotted in grey.	108
6.5	A DA white dwarf model (blue) and composite white dwarf - brown dwarf models for two spectral types, M8 (purple), and L0 (pink). The observed photometry from SDSS and UKIDSS are plotted in red and the SDSS visible and GNIRS near-infrared spectra are plotted in grey.	109
6.6	A DA white dwarf model (blue) and composite white dwarf - brown dwarf models for three spectral types, L5 (purple), L6 (yellow), and L7 (pink). The observed photometry from SDSS and UKIDSS are plotted in red and the SDSS visible and GNIRS near-infrared spectra are plotted in grey.	110
6.7	A DA white dwarf model (blue) and composite white dwarf - brown dwarf models for three spectral types, L5 (purple), L6 (yellow), and L7 (pink). The observed photometry from SDSS and UKIDSS are plotted in red and the SDSS visible and GNIRS near-infrared spectra are plotted in grey.	111

6.8 A DA white dwarf model (blue) and composite white dwarf - brown dwarf models for three spectral types, L2 (purple), L3 (yellow), and L4 (pink). The observed photometry from SDSS and UKIDSS are plotted in red and the SDSS visible and GNIRS near-infrared spectra are plotted in grey. 112

6.9 A DA white dwarf model (blue) and composite white dwarf - brown dwarf models for three spectral types, M8 (purple), and M9 (pink). The observed photometry from SDSS and UKIDSS are plotted in red and the SDSS visible and GNIRS near-infrared spectra are plotted in grey. 113

List of Tables

1.1	A summary of the current known white dwarf - brown dwarf non-interacting close binary systems discovered so far. The names, orbital period and properties (mass, temperature) of the white and brown dwarf are listed, as well as a brown dwarf spectral type estimate, where available.	18
1.2	A summary of the current known polars, low accretion rate polars (LARPs), and CVs with brown dwarf donors.	23
1.3	A continuation of Table 1.2	24
2.1	The minimum, maximum, and effective wavelengths of the three UVOT filters used (Rodrigo et al., 2012).	30
4.1	XSHOOTER data from the first night of observations. There are three main columns date, radial velocity of the absorption feature, and radial velocity of the emission feature. This is then duplicated in the neighbouring three columns. . . .	55
4.2	XSHOOTER data from the second night of observations. The columns are identical to Table 5.1	56

4.3	The best fit radial velocity parameters (cf. equation 5.1) to the emission lines. The period and zero ephemeris were determined by fitting the white dwarf radial velocity data and can be found in Table 4.6. P and T_0 and were then held constant for all subsequent emission lines. The equivalent widths of the emission lines were determined, where possible, from the line profiles.	57
4.4	A continuation of Table 4.3. The best fit radial velocity parameters to the K I, Ca I & II, and Ti I emission lines.	59
4.5	A continuation of Tables 4.3 and 4.4. The best fit radial velocity parameters to the Fe I & II emission lines.	60
4.6	The values obtained from fitting Equation (5.1) to the measured radial velocities of the $H\alpha$ absorption and emission lines. The error on the final digit of the period is shown in parentheses. We list the corrected semi-amplitude for the brown dwarf used to correct for the light from the emission being offset from the centre of mass of the brown dwarf; we used this value to calculate the masses of the white dwarf and brown dwarf.	71
5.1	The measured XSHOOTER radial velocity data for all 20 frames taken on 2014-Aug-29.	77
5.2	The parameters of the orbit of NLTT5306 found by fitting Equation 5.1 to a combined data set of our measured radial velocities and the radial velocities published in Steele et al. (2013). Zero phase is defined as when the white dwarf is furthest from the observer. The values below the centre line are taken from Steele et al. (2013) and listed here for convenience due to their use in this work.	79
5.3	The predicted magnitudes for observations using UVOT in three wavebands. The effective wavelengths have been taken from Rodrigo et al. (2012).	82

5.4	Details of all <i>swift</i> observations of NLTT5306. ¹ This observation was split into 4 smaller snapshots therefore a fourth observation was done to compensate for this.	84
5.5	The predicted magnitudes compared to the measured magnitudes from observations using UVOT in three wavebands. The effective wavelengths have been taken from Rodrigo et al. (2012).	85
5.6	The results of Roche Lobe radius calculations for four different inclinations	88
6.1	This table summarises key properties of the eight white dwarf - brown dwarf candidate systems investigated. This distances have been updated according to Gaia DR2. References: Eisenstein et al. (2006) (1), Steele et al. (2011) (2), Girven et al. (2011) (3), Kepler et al. (2015) (4), Kepler et al. (2016) (5)	96
6.2	The observing schedule for each target and the average air mass for each night. The final column lists the signal-to-noise achieved from combining all OBs into one final spectrum.	100
6.3	All brown dwarf standard spectra, of spectral types pertinent to this work, from the IRTF Spectral Library. The associated references are Burgasser & McElwain (2006)(1), (Burgasser et al., 2007)(2), Burgasser et al. (2008) (3), Kirkpatrick et al. (2010) (4), and Burgasser et al. (2010) (5). For each spectral type the H band flux was calculated from the mean 2MASS absolute magnitudes (Dupuy & Liu, 2012).	102
6.4	The H band absolute magnitudes estimated from the T_{eff} and $\log g$ of each system and compared to Pierre Bergeron's cooling models. I have also calculated the corresponding flux values in each case.	103
6.5	The SDSS ugriz and UKIDSS YJHK magnitudes, where available, for all eight candidate white dwarf - brown dwarf systems in this Chapter.	104

1

Introduction

Over the last few decades the discovery of exoplanets has risen to the forefront of astronomical research. We have discovered 1000's of planets and, to a certain extent, they have been characterised (mass, radius, density). It is clear that planets are rife within our galaxy however characterising their atmospheres is extremely difficult. The currently available telescopes and observatories both in space and on Earth are not yet capable of fully characterising a planetary atmosphere¹. This is largely due to the fact planets are very small and faint in comparison to their host stars thus spectroscopic observations are dominated by stellar activity. It is therefore very difficult to separate the planetary atmospheric fluctuations (weather, clouds etc.) from the larger, brighter stellar

¹The Hubble Space Telescope does have the capability to perform transmission spectroscopy, however this is still very much in it's infancy

fluctuation e.g. sun-spots and flares.

There is a class of objects known as brown dwarfs which are thought of as a bridge between planets and stars. They do not burn hydrogen so their atmospheres are akin to planets, but due to their larger mass, they are brighter than planets, thus their atmospheres have been observed, analysed, and modelled. Brown dwarf atmospheres are better understood (REF). To compare an exoplanet to a brown dwarf requires observations of both in similar environments i.e. close in to their host star. As previously mentioned, a main sequence stellar host contaminates the observed spectra making isolating the companion atmosphere very difficult. Brown dwarf companions to main sequence stars suffer from this in much the same way a Hot Jupiter does.

The study of brown dwarfs around white dwarf stars offers a unique opportunity to observe a planet-like atmosphere without these observational challenges. A white dwarf, having burnt all its fuel, has a much more stable atmosphere than a main sequence star and emits primarily in the blue. Brown dwarfs are larger in radius than white dwarf stars thus dominating the red end of the observed spectrum. These differences make separating the brown dwarf and white dwarf spectra much easier. Thus white dwarf - brown dwarf binary systems provide an excellent test bed for understanding the effect of stellar irradiation on a planetary-like atmosphere.

The main challenge is the fact brown dwarf companions in close orbits with main sequence stars are extremely rare; this dearth is known as the brown dwarf desert. The reasons for the existence of this desert are not currently known. It may be due to difficulty in forming extreme mass ratio binaries within such close proximity. It could also be due to the inward migration (or lack thereof) of a brown dwarf from a larger separation. A consequence of the brown dwarf desert is that close brown dwarf companions to white dwarf stars are rarer still (Steele et al., 2011).

Nevertheless a small number have been discovered and in this work I investigate two systems: WD0137-349 and NLTT5306. The former displays irradiation induced metal emission lines in a substellar atmosphere. I investigated the line strengths of the $H\alpha$ and Ca II line and found these to vary with orbital phase and almost completely disappear on the dark-side of the brown dwarf. This implies that heat redistribution around this tidally locked companion is likely to be poor. This

result informs, and will have to be replicated by, future planetary atmosphere models.

NLTT6306 is almost identical to WD0137-349 in component mass and orbital period, the only difference being the age and therefore temperature of the white dwarf primary. This system, despite being cooler, displays $H\alpha$ emission and Na I absorption associated with the white dwarf which indicates accretion is happening. Using the Ultra-Violet Optical Telescope (UVOT) and X-Ray Telescope (XRT) on board *Swift* I calculated an upper limit on the mass accretion rate of $2 \times 10^{-15} M_{\odot} \text{ yr}^{-1}$. From this I calculated the critical magnetic field required, to prevent a disk forming from matter accreting at this rate, to be 0.45 kG. This field strength and mass transfer rate are too low to produce detectable Zeeman line splitting or cyclotron humps and indicates that it is possible a light wind from the brown dwarf is being magnetically funnelled from the white dwarf onto the white dwarf surface.

The effects of insolation in creating a temperature inversion that gives rise to metal emission lines in a sub-stellar atmosphere informs us on what is to be expected from planet-like atmospheres. Whilst a seemingly almost identical system, NLTT5306, shows none of these signs but is a good laboratory for understanding the transition from detached close binary to semi-detached/interacting binary, allowing for investigation into the early period of a cataclysmic variable with a sub-stellar companion. The next step is to find more of these systems; in my third chapter I analyse Gemini near-infrared spectra from 8 white dwarfs with photometrically confirmed infrared excesses. I compared the spectra to composite models I produced by combining white dwarf models created using TLUSTY, with brown dwarf spectral standards from the InfraRed Telescope Facility (IRTF). From this I was able to identify

In this chapter I provide an introduction into degenerate objects focussing on white dwarf stars and substellar brown dwarfs. I will explain their evolution, individual classification, and then go on to describe how a close white dwarf - brown dwarf binary forms. Finally I will discuss the differences and similarities between brown dwarfs irradiated by white dwarfs and Hot Jupiters irradiated by main sequence stars.

1.1 White dwarfs

White dwarfs are the final stage of stellar evolution for the majority of stars; approximately 97% of all stars in the Milky Way will become white dwarfs (Fontaine et al., 2001). After formation their stellar evolution begins on the main sequence where a star burns hydrogen in its core Figure 1.1 - (1). When the star runs out of hydrogen to burn in its core, the internal pressure is overpowered by gravity and it begins to collapse. This collapse releases gravitational potential energy that ignites a shell of hydrogen around the core and the star moves off of the main sequence along the Red Giant Branch (RGB) Figure 1.1 - (2). The gravitational pressure causes hydrogen burning in the shell to happen more rapidly which increases the star's luminosity by an order of magnitude. This in turn causes the star to expand and cool. The hydrogen burning shell moves radially outwards as each subsequent shell runs out of hydrogen and the helium ash falls to the core. For low mass stars ($\approx 0.4 M_{\odot}$) and those with companions this is where evolution stops. Either due to being not massive enough for the gravitational pressure to ignite further burning or due to their horizontal branch (HB) phase being disrupted by a low mass companion (see Section 1.3).

For a stars with masses between $0.6 - 10 M_{\odot}$ evolution continues. The pressure on the helium core causes the helium to become degenerate and ignite in what is known as the helium flash at the top of the RGB, Figure 1.1 - (3).

Following the Helium flash the core expands which exerts a pressure that pushes against gravitational collapse and reduces the pressure at the core/shell boundary. This weakens the hydrogen shell burning which allows the star to contract and thus increase in temperature (Carroll & Ostlie, 1996). Once the star has exhausted its supply of helium in the core the star collapses again. This ignites helium shell burning but the majority of the energy is still being generated by hydrogen burning shells at larger radii (Hansen & Kawaler, 1994). This maintains the hydrostatic equilibrium of the star. Helium ash falling from a hydrogen burning shell onto a helium burning shell causes periodic thermal pulses (Cox, 1980). This is known as the Asymptotic Giant Branch (AGB) Figure 1.1 - (4-5). A star reaches the tip of this branch when it runs out of fuel to burn in all of its shells. During the AGB phase the stars large radius leads to a significant mass loss as the

outer layers are expelled by stellar wind; this forms a planetary nebula Figure 1.1 - (5–6) (Iben & Renzini, 1983). At the center of this nebula is the core of the star which cools for the remainder of its existence and is known as a white dwarf.

Without the energy generation of fusion, the star collapses under its own gravity until electron degeneracy halts the collapse and the white dwarf then cools for the remainder of its life Figure 1.1 - (7). There is a critical mass beyond which electron degeneracy no longer holds against gravity and the star collapses further into a neutron star. This mass limit is known as the Chandrasekar mass limit and is found to be $\approx 1.44 M_{\odot}$ (Chandrasekhar, 1931). Chandrasekhar (1935) then went on to determine the relationship between the mass, M and radius, R of a white dwarf,

$$M^{1/3}R = \text{constant}. \quad (1.1)$$

So the more massive the star, the smaller its radius (Sweigart et al., 1990; Beccari & Carraro, 2015). For example, a white dwarf of similar mass to the Sun will have approximately the same volume as the Earth (Shipman, 1979). A newly formed white dwarf has an effective temperature of $\approx 100,000 - 200,000$ K (McCook & Sion, 1999) and this thermal energy is gradually radiated away over a very large time-scale (longer than the current age of the universe).

There are many different classes of white dwarf depending on their temperature and composition. They are separated into two main groups: hydrogen rich DA stars and helium rich non-DA stars (non-DA white dwarfs are further divided into subclasses). All the white dwarfs discussed in this chapter are DA white dwarfs (Luyten, 1952; Greenstein, 1960).

1.2 Brown dwarfs

Brown dwarfs bridge the formation gap between stars and planets (Kumar 1963; Burrows et al. 2001). They are thought to form like stars due to some brown dwarfs having been observed with

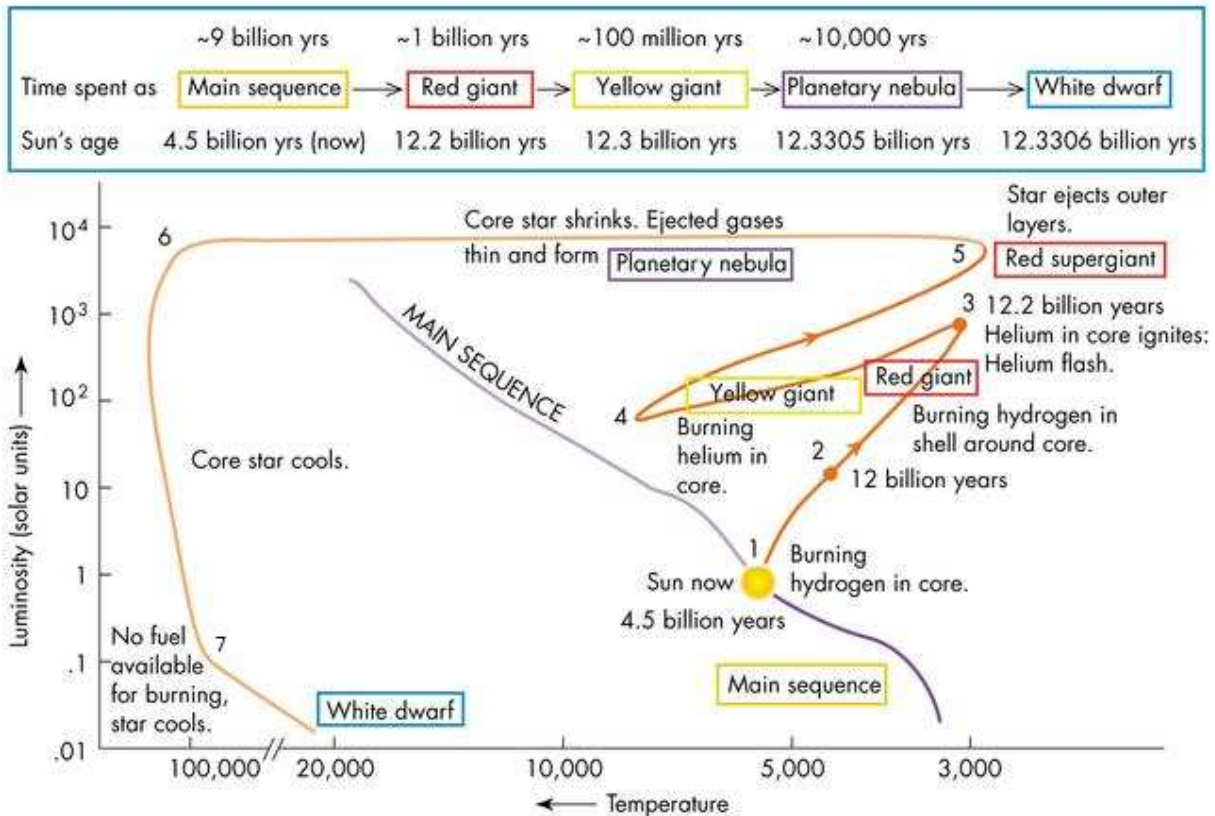


Figure 1.1: An illustration of a Hertzsprung-Russell diagram showing how a solar mass main sequence star evolves into a white dwarf. The number denote key points in a main sequence stars' evolution. Main sequence hydrogen burning (1), exhausting all hydrogen in the core, and the beginning of hydrogen shell burning (2), the ignition of helium burning in the core known, as the Helium Flash (3), helium shell burning (4–5), expulsion of outer layers by a stellar wind forming a planetary nebula (5–6), core of the star cools to a white dwarf (7).

jets and discs akin to those seen in stellar formation, for example Sterzik et al. 2004; Luhman et al. 2007. Brown dwarfs have masses below $0.072 M_{\odot}$ and therefore achieve hydrostatic equilibrium, from electron degeneracy pressure, before reaching the critical temperature required to ignite hydrogen in the core (Hayashi & Nakano, 1963; Kumar, 1963).

They do, however, have a period of deuterium burning of about $\approx 10^7$ years (Chabrier et al., 2000; Dantona & Mazzitelli, 1985; Kroupa, 2001; Chabrier et al., 2014). Deuterium burning is where a heavy hydrogen atom, made from one proton and one neutron, combines with another proton to form helium-3. Lithium burning also occurs within higher mass brown dwarfs; Lithium in the atmosphere is transported to the core via convection where burning occurs through a collision of Lithium-7 with a proton producing two helium-4 nuclei. In this way the Lithium in the brown dwarf atmosphere is depleted (Basri, 1998). The temperature necessary for this reaction is just below that for hydrogen fusion so stars deplete their Lithium rapidly after formation; thus the 'Lithium Test' is a method used to determine if an object is substellar.

After that brief phase they cool for the rest of their lifetime. The mass limit for deuterium burning is often quoted as $\approx 13 M_{\text{Jup}}$ where $\approx 50\%$ of the deuterium is burned (Burrows et al., 1997). However Spiegel et al. (2011) found that this mass limit can range from $11.4 - 14.4 M_{\text{Jup}}$ depending on the mass, metallicity, and initial deuterium abundance of the sub-stellar object resulting in $10 - 90\%$ of the initial deuterium being burned, respectively. For this reason deciding where to draw the boundaries between, brown dwarfs and planets is still being debated.

There are four types of brown dwarf: M ($T_{\text{eff}} \approx 2500 - 3500$), L ($T_{\text{eff}} \approx 1400 \text{ K} - 2500 \text{ K}$), T ($T_{\text{eff}} \approx 600 \text{ K} - 1400 \text{ K}$), and Y-type dwarfs ($T_{\text{eff}} \approx 250 \text{ K} - 600 \text{ K}$) (Burrows et al., 2003) this is also the evolutionary sequence of many brown dwarfs as they cool over time. A brown dwarf would be classified into one of these groups based on its observed spectra; Figure 1.2 illustrates the observable absorption features for a range of brown dwarf spectral types.

The M class can include low mass stars and brown dwarfs this is because many young brown dwarfs are classified as M-dwarfs due to their temperature and therefore youth. Later spectral types (M6 onwards) will have substellar masses and therefore brown dwarfs (Burrows et al.,

1997). It is very difficult to distinguish between an M-class brown dwarf and M-dwarf star *at the same temperature*. The L, T, and Y classes contain only brown dwarfs. Each group is characterised by the different absorption features observed in its spectrum demonstrated in Figure 1.2. To classify brown dwarfs, broadband photometry and brown dwarf spectra are compared to spectral standards and/or brown dwarf models.

Using broadband photometry alone only allows for an initial test to find good candidate brown dwarfs. If the photometry lines up well with spectral standards then follow up spectroscopy is performed. This allows the brown dwarf spectrum to be compared with known spectral templates or brown dwarf models. Spectroscopic observations are therefore the most important for accurately determining the physical properties of young objects (e.g. Weights et al. (2009)).

Early M-dwarfs are often magnetically active, and characterised mainly by the presence of titanium oxide (TiO), vanadium oxide (VO), iron hydride (FeH), and calcium monohydride (CaH) absorption lines. This category contains low mass stars and high mass sub-stellar objects, brown dwarfs. Figure 1.3 from (Dieterich et al., 2014) shows the low-mass end of the Hertzsprung–Russell diagram; there is a continuum of M-dwarf stars through to sub-stellar objects.

L-dwarfs exhibit strong TiO, VO, and FeH absorption features as well as water (H₂O), carbon monoxide (CO), potassium (K), and sodium (Na). As an L-dwarf cools the Na and K lines weaken and broaden while the water and FeH lines strengthen (see Fig. 1.2). Below ≈ 2500 K the various chemical species in the photosphere of L-dwarfs condense into clouds causing the brown dwarf to redden and some molecular absorption features appear (Allard et al., 2001). The dwarf cools further and the CO lines weaken as methane begins to form. The near-infrared colour of the brown dwarf changes with this atmospheric composition change but its temperature stays almost constant (Kirkpatrick et al., 1999). This is referred to as the L–T transition region and is associated with atmospheric variability attributed to variable, or patchy, cloud coverage (Marley et al. 2010; Apai et al. 2013).

Early T-dwarfs have Na and K absorption features as well as methane (CH₄). The condensate clouds present in L-dwarfs abruptly disappear during the L–T transition; it has been suggested

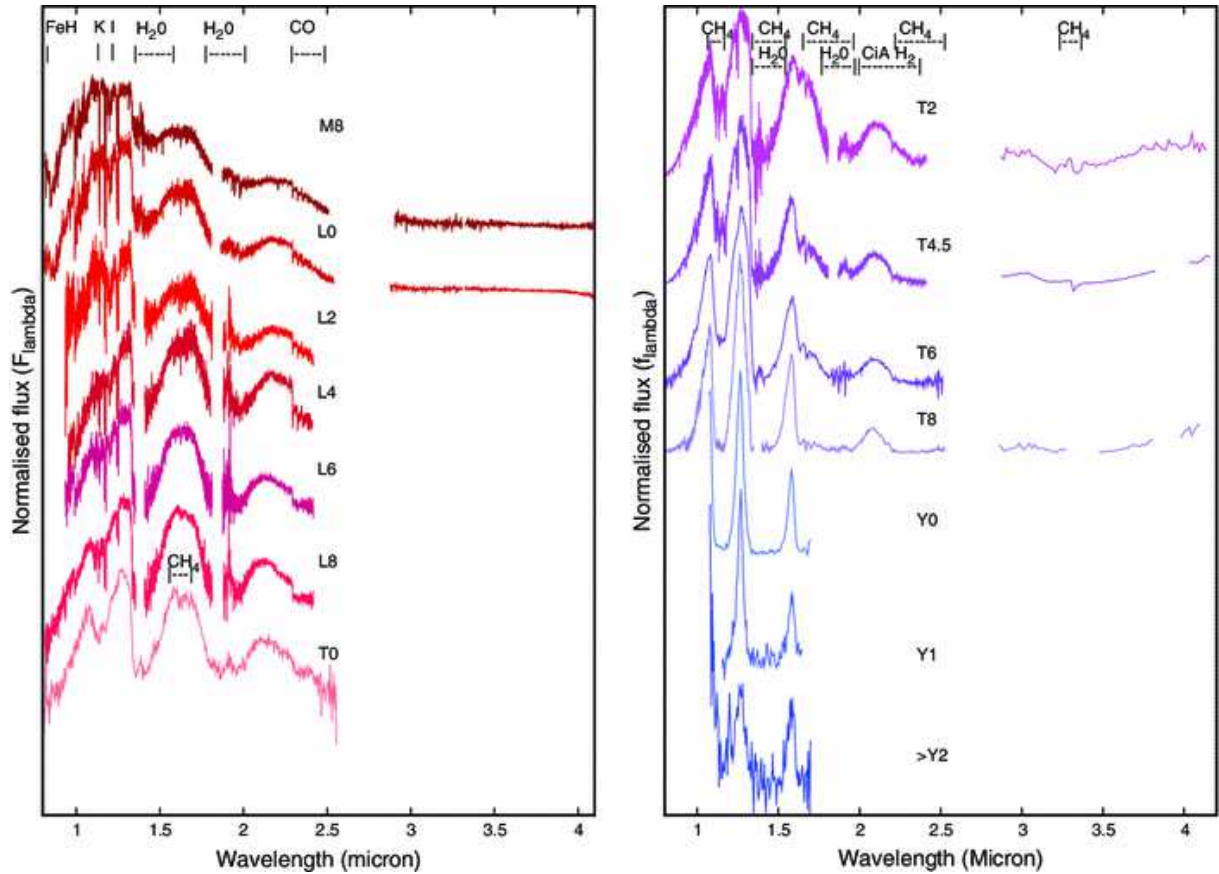


Figure 1.2: This figure has been taken from Helling & Casewell (2014). It shows the near-infrared spectra of M-dwarfs through to Y-dwarfs for a wavelength range of 1 – 4 μm . Each spectrum has been normalised and offset by a constant to better display the spectral features caused by the presence of atoms and molecules listed along the top of the plot.

that the clouds sink below the photosphere as the dwarf cools thus 'hiding' any absorption features (Ackerman & Marley, 2001; Cooper et al., 2003). This is indicative of dynamic effects driving cloud evolution (Cushing et al., 2008). As T-dwarfs cool the Na and K lines weaken leaving only strong methane absorption lines.

The coolest class of brown dwarf is a Y-dwarf which emits the majority of its flux in the mid-infrared. The first Y0 class brown dwarf was discovered using the Wide-field Infrared Survey Explorer (WISE) (Cushing et al., 2011). These objects display very deep CH_4 and H_2O absorption features. The water condenses in the upper atmosphere and forms ice clouds which greatly

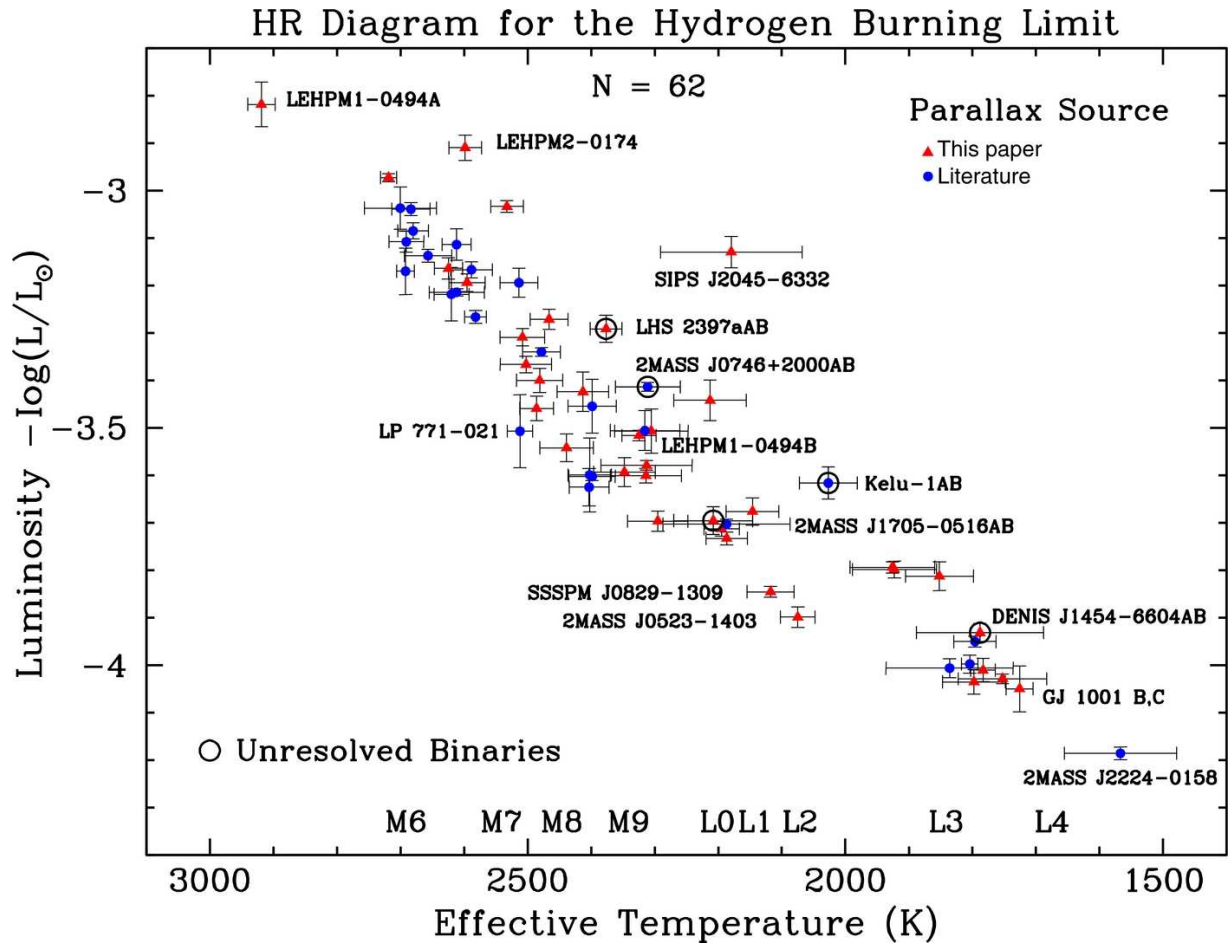


Figure 1.3: This plot has been taken from Dieterich et al. (2014). It shows the low-mass end of the main sequence in the Hertzsprung-Russell diagram with temperature decreasing from 3000 K to 1500 K. It includes late M-dwarfs through to mid-L-dwarfs whose luminosities decrease with decreasing temperature.

affect the Y-dwarfs effective temperature which is estimated to be between 225 – 260 K (Morley et al., 2014). As their effective temperature drops ammonia (NH_3) absorption dominates over the methane and water.

Though rare close white dwarf - brown dwarf systems do exist and I will describe their formation in the following section. I will also describe the evolutionary trajectory of such systems.

1.3 Stellar binary evolution

A stellar binary is a system containing two stars, typically of equal mass. These systems are relatively common (Abt & Levy, 1976) and begin life as two detached objects orbiting their centre of mass. Each star exists with its own Roche Lobe which is the boundary within which any orbiting material is gravitationally bound to that star (Eggleton, 1983).

More massive stars evolve more rapidly following the process described in Section 1.1 i.e. the star will run out of hydrogen in its core and will evolve away from the main sequence. As it moves along the RGB and/or AGB its radius will increase to $\approx 20\text{--}100 R_{\odot}$. If the evolving star's Roche Lobe is filled, mass transfer occurs through the inner Lagrangian point (the point between the two objects where the gravitational pull is equal). This rapid phase of mass transfer results in the brown dwarf being unable to accept all the donated mass and thus becomes engulfed by the red giants envelope. This is known as a common envelope and is illustrated in Figure 1.4. This envelope exerts a drag force on the secondary causing it to lose angular momentum and spiral in towards the center of mass. This release of orbital angular momentum is transferred to the envelope as kinetic energy; ejecting it from the binary system (Iben & Livio, 1993).

The remaining binary system will consist of a white dwarf with a stellar companion at a much smaller separation than before (Meyer & Meyer-Hofmeister, 1979). Eventually the orbit of the secondary will decay enough to allow the gravity of the white dwarf to distort the companion and initiate mass transfer from the companion to white dwarf. This system is known as a cataclysmic variable (CV). The variability of CVs stems from the instability of the accretion disk surrounding the white dwarf leading to portions of the disk releasing its gravitational potential energy as radiation and falling onto the white dwarf.

If mass transfer is initiated due to the magnetic field of the white dwarf pulling material off the surface of the companion this is known as a Polar. Polars have phases of high and low accretion and the trigger for the changes from a low to a high state is still uncertain (Schwope et al., 2002). It is thought to be linked to changes in orbital separation (Webbink & Wickramasinghe, 2005). When they are in a low state they are known as Low Accretion Rate Polars (LARPs) (Schwope

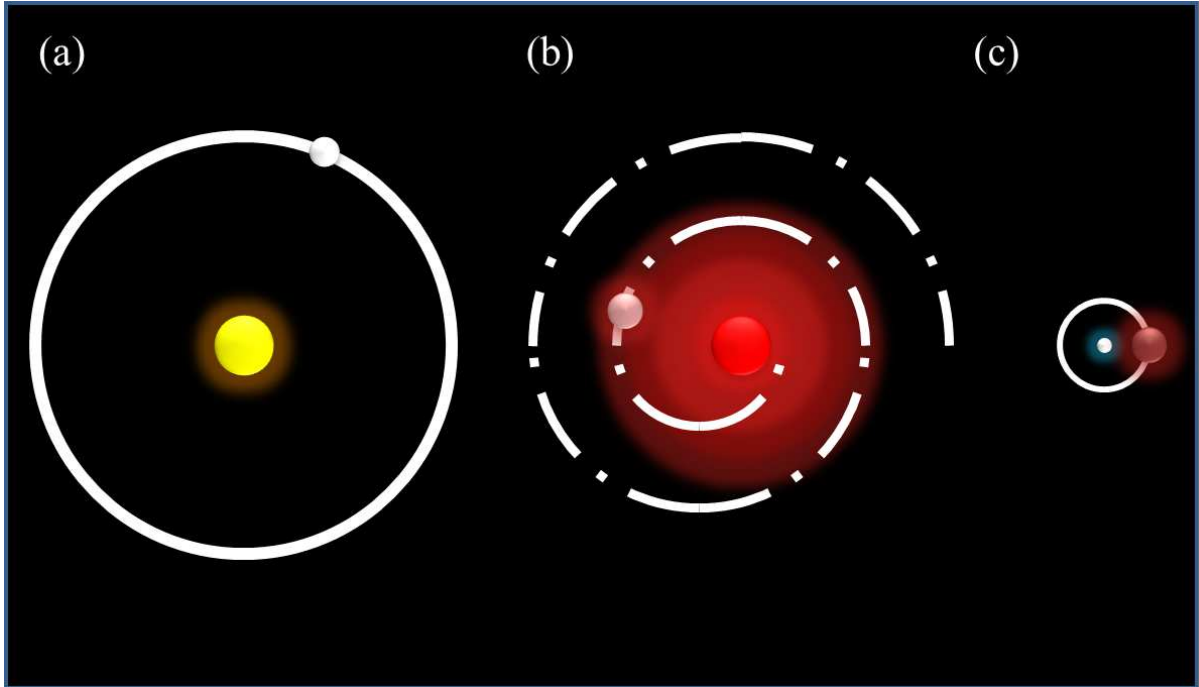


Figure 1.4: This shows the progression of CE evolution. As the star evolves off the main sequence (a) and moves up the red giant branch it will overflow its Roche lobe leading to dynamically unstable mass transfer. The brown dwarf, unable to accept all the material, is engulfed by the stars outer layers, forming a contact binary, and the drag causes it to spiral in and surrender its orbital energy to the gaseous envelope. The envelope is then expelled into space leaving a close white dwarf – brown dwarf binary (c).

et al., 2002).

1.4 Using brown dwarfs as exoplanet analogues.

I will now discuss the key differences between brown dwarfs orbiting white dwarfs and exoplanets orbiting main sequence stars.

One of the main differences between brown dwarfs and planets is their mass and therefore their atmospheric density. Brown dwarfs, by definition, are more massive than exoplanets however their radii are typically $\sim 1 R_{\text{Jup}}$ this means brown dwarfs have atmospheric densities typically

between 10 – 100 times more than planets. Another difference is the nature of the stellar host: main sequence stars (MS) vs white dwarfs. White dwarf stars typically peak in the blue UV (200 - 300 nm) end of the spectrum whereas MS stars typically peak in the visible (400 - 700 nm) region. Therefore the energy of the photons incident on a white-dwarf-irradiated brown dwarf would be higher than that of a Hot Jupiter + main sequence star. The final significant difference is the relative sizes of the objects within each system. A Jupiter-like exoplanet around a Sun-like MS star would be \sim a tenth of the size of the star; this is reversed in the case of a brown dwarf - white dwarf binary. The brown dwarfs much larger radius than it's white dwarf stellar host means that the irradiation is not evenly distributed across the whole hemisphere of it's surface facing the white dwarf.

Despite these differences brown dwarfs atmospheric chemistry has strong similarities with planetary atmospheres such as Jupiter (Helling & Casewell, 2014). Indeed water and carbon monoxide have been detected in a number of exoplanet atmospheres (e.g., Konopacky et al. 2013; Kreidberg et al. 2014; Sing et al. 2016). As such, brown dwarfs and gas giant exo-planets are often thought of as a continuum of objects despite their distinct origins and evolutions. Thus the observation driven study of short period irradiated brown dwarf atmospheres can give us insights into the interiors of hot Jupiters (Beatty et al., 2014; Showman et al., 2015).

1.5 Known close white dwarf – brown dwarf binary systems

As mentioned earlier brown dwarf companions to main sequence stars within 3 AU are rare compared to planetary or stellar companions to main sequence stars (Grether & Lineweaver, 2007). This is known as the brown dwarf desert and does not appear to extend out to larger radii (Metchev, 2006). Brown dwarf companions to white dwarf stars are even rarer with only 0.5% of white dwarfs having a brown dwarf companion (Steele et al., 2011). There are many candidate systems (e.g. Girven et al. 2011; Debes et al. 2011; Steele et al. 2011) however only a few have been confirmed.

Here I will introduce all currently known close white dwarf - brown dwarf binary systems I will divide the into two groups: non-interacting and interacting. I will order them chronologically by discovery date.

1.5.1 Non-interacting

GD1400

The presence of a sub-stellar mass companion was first indicated through spectroscopic and photometric observations of GD 1400 (Farihi & Christopher, 2004). They estimated the brown dwarf spectral type be L5.5 or later. Further IR spectroscopy was obtained by Dobbie et al. (2005) putting the spectral type at L7. Further observations with UVES provided radial velocity curves of the white dwarf placing the period at 9.98 hours (Burleigh et al., 2011); they also put lower limits on the white and brown dwarf masses, $0.55 M_{\odot}$ and $0.06 M_{\odot}$, respectively.

WD0137-349

WD0137-349 is a non-interacting, non-eclipsing white dwarf - brown dwarf binary system. WD0137 - 349 was first recorded in a survey for metal poor stars conducted by Preston et al. (1991) and was perceived to be an unremarkable faint, blue star. Improved spectroscopy by Beers et al. (1992) revealed it to be a white dwarf. WD0137-349 was observed by the ESO Ia Progenitor survey conducted by Napiwotzki et al. (2001) and found to be a radial velocity variable. 2MASS photometry revealed an infrared excess and Maxted et al. (2006) determined the systems mass ratio to be $0.134 \pm 0.0002 M_{\odot}$, the white dwarf effective temperature of 16 500 K, $\log g$ of 7.49 ± 0.08 (c.g.s. units) and period of 0.0803 ± 0.0002 days. Burleigh et al. (2006) then obtained additional spectra, using the Gemini telescope and the Gemini Near-Infrared Spectrograph, to better characterise the brown dwarf. They estimate the brown dwarf spectral type to be L6 –

L8 giving a temperature estimate of $1300 < T_{\text{eff}} < 1400$ K. This temperature coupled with the brown dwarf mass of $0.053 M_{\odot}$ is consistent with a cooling age of ≈ 10 Gyr suggesting that the brown dwarf was unaffected by the common envelope evolution. The brown dwarf intercepts 1% of the primarily UV white dwarf radiation and is tidally locked to its 16 500 K host. This results in one side being continually irradiated giving the brown dwarf a temperature difference of 500 K between its "night-" and "day" – side (Casewell et al., 2015).

WD0837+185

Casewell et al. (2012) present the discovery of a close ($a \approx 0.006$ AU, $P = 4.2$ hrs) substellar companion and they classify it as a T8 brown dwarf. The primary star was found to have a massive white dwarf progenitor ($3.5 - 3.7 M_{\odot}$). This large mass means the brown dwarf must have been engulfed by the white dwarf progenitor's envelope whilst on the late AGB. Casewell et al. (2012) identified it as a member of the Praesepe star cluster and conclude that the substellar companion was probably captured by the white dwarf progenitor early in the life of the cluster, rather than forming in situ.

SDSS J141126.20+200911.1

The first non-interacting eclipsing white dwarf - brown dwarf system to be discovered was SDSS J141126.20+200911.1 (SDSS 1411) with a period of 121.73 mins (Beuermann et al., 2013), a white dwarf mass of $0.53 \pm 0.03 M_{\odot}$ with an effective temperature of $13\,000 \pm 300$ K. The companion has a white dwarf model dependent mass of $0.050 \pm 0.002 M_{\odot}$ and a spectral type of T5 determined from a flux excess in the K_s band (Littlefair et al., 2014). This system is not hugely dissimilar to WD0137-349. They conclude that the irradiation could be causing a temperature increase on one hemisphere of the brown dwarf, however no irradiation induced emission is detected.

SDSS J155720.77+091624.6

This object was initially thought to be a white dwarf with a dust disk due to an infrared excess (Farihi et al., 2012). Subsequent spectroscopy revealed a brown dwarf companion was also present within a circumbinary debris disk (Farihi et al., 2017). This system contains a 21800 ± 800 K $0.447 \pm 0.043 M_{\odot}$ white dwarf and 0.063 ± 0.002 brown dwarf orbiting with a period of 2.27 hours. SDSS J1557+0916 is in a steady state of accretion with an inferred accretion rate is $\dot{M} \simeq 9.5 \times 10^{-18} M_{\odot} \text{yr}^{-1}$ assuming a bulk Earth abundance for Mg (Farihi et al., 2017).

SDSS J123127.14+004132.9

Building on the work by (Rebassa-Mansergas et al., 2016), Parsons et al. (2017) found the primary white dwarf has a $T_{\text{eff}} = 37210 \pm 1140$ K and a $\log g = 7.77 \pm 0.15$. They also estimate the white dwarf mass to be $0.56 \pm 0.07 M_{\odot}$. Their lightcurves indicate a period of 72.5 mins and they observe 4 partial eclipses of the white dwarf. This allowed Parsons et al. to estimate the age of the system to be 1 Gyr and put an upper mass limit of $0.095 M_{\odot}$ on the brown dwarf.

SDSS J120515.80-024222.6

A similar system, SDSS J120515.80-024222.6, is a $0.39 \pm 0.02 M_{\odot}$ helium-core white dwarf which is totally eclipsed by a $0.049 \pm 0.006 M_{\odot}$ ($51 \pm 6 M_{\text{Jup}}$) brown dwarf companion (Parsons et al., 2017). The orbital period was measured to be 71.2 mins. From modelling the IR spectrum they estimate the companions spectral type to be an L0. follow-up photometry and spectroscopy of this pre-CV has provided white and brown dwarf masses: 0.415 ± 0.028 and 0.061 ± 0.010 , respectively (Rappaport et al., 2017).

EPIC212235321

This system was discovered by Casewell et al. (2018) to be the shortest-period (68.2 min), non-interacting, white dwarf-brown dwarf post-common-envelope binary known. They present VISTA magnitudes which indicate a significant reflection effect and XSHOOTER spectra of the brown dwarf that have emission features similar to WD0137-349B (Longstaff et al., 2017). They determine the white dwarf mass to be $0.47 \pm 0.01 M_{\odot}$ and estimate the brown dwarf mass to be $58 M_{\text{Jup}}$ which suggests the spectral type is likely to be L3.

I have summarised these non-interacting binary systems in Table 1.1.

1.5.2 Interacting

The non-interacting systems above are progenitors of CVs. In each system the orbit of the brown dwarf will eventually decay until the point where its radius is larger than its Roche Lobe radius; thus marks the zero age CV. There exists a small sub-group of CVs that have brown dwarf donors and these systems will be discussed individually below.

EF Eridani

EF Eridani (EF Eri) was first observed by Wheatley & Ramsay (1998) and there was no detection of the companion. Follow up analysis of the low-state spectrophotometry by Beuermann et al. (2000) showed that this non-detection indicated that the companion must have a spectral type later than M9. They went on to put limits on the mass of the secondary for a range of masses on the primary white dwarf. EF Eri was found to have an accretion rate of $3.2 \times 10^{-11} M_{\odot} \text{yr}^{-1}$ (Schwope et al., 2007) and further observation with X-shooter revealed emission lines from the secondary due to irradiation from the white dwarf (Schwope & Christensen, 2010). In the same

Name	Orbital period	White Dwarf		Brown Dwarf		
		Mass	Temperature	Mass	Temperature	Spectral Type
GD1400	9.98 hours	>0.55	11500	>0.06	-	L7
WD0137-349	114 mins	0.39 ± 0.04	16 500	>0.053	~1350	L6 - L8
WD0837+185	4.2 hours	0.798 ± 0.006	~15 000	>0.024	~1000	T8
SDSS J141126.20 +200911.1	121 mins	0.53 ± 0.03	13000 ± 300	0.050 ± 0.002	-	T5
SDSS J155720.77 +091624.6	2.27 hours	0.447 ± 0.043	21800 ± 800	0.063 ± 0.002	-	-
SDSS J123127.14 +004132.9	72.5 mins	0.56 ± 0.07	37210 ± 1140	>0.095	-	-
SDSS J120515.80 -024222.6	71.2 mins	0.415 ± 0.028	-	0.061 ± 0.010	-	L0
EPIC212235321	68.2 mins	0.47 ± 0.01	-	>0.056	-	L3

Table 1.1: A summary of the current known white dwarf - brown dwarf non-interacting close binary systems discovered so far. The names, orbital period and properties (mass, temperature) of the white and brown dwarf are listed, as well as a brown dwarf spectral type estimate, where available.

paper they went on to constrain the white dwarf mass to be $> 0.65 M_{\odot}$ and therefore put a limit on the companion mass of $< 0.06 M_{\odot}$.

WZ Sagittae

WZ Sagittae is a CV containing a white dwarf ($M_1 > 0.7 M_{\odot}$) and a brown dwarf ($M_2 < 0.1 M_{\odot}$; Steeghs et al. 2001) with an effective temperature of 1800 K (Harrison et al., 2013) and by directly detecting the companion, Harrison (2016) estimate a spectral type between L2 - L8. The only lines detected coming from the companion were CO absorption lines and $H\alpha$ emission lines due to irradiation (Steeghs et al., 2001).

SDSS J125044.42 +154957.4

This system was first identified by Vanlandingham et al. (2005) in SDSS DR3; they estimated the white dwarf temperature to be 10 000 K. Steele et al. (2011) describe it as a magnetic white dwarf with a mass of $\sim 0.60 M_{\odot}$ and a B field of 20 MG (Külebi et al., 2009). Steele et al. (2011) detect an infrared excess which lead to an estimate of the spectral type to be M8. Breedt et al. (2012) followed this up with phase resolved spectroscopy and found an orbital period of 86 mins using the $H\alpha$ emission from the brown dwarf companion. Without further spectroscopic analysis this system can not be categorically confirmed to be a brown dwarf but its late M spectral type suggests it could be a bona fide brown dwarf. However the large magnetic field present could mean the infrared excess is partly due to cyclotron emission as seen in SDSS J121209.31+013627.7 (Bailey et al. 1991; Farihi et al. 2008)

SDSS J151415.65 +074446.5

This system was identified as a magnetic white dwarf from SDSS spectra (Vanlandingham et al. 2005; Külebi et al. 2009) with a 36 ± 4 MG magnetic field (Külebi et al., 2009). Breedt et al. (2012) used the estimated temperature ($T_{\text{eff}} \sim 10\,000$ K; Vanlandingham et al. 2005; Külebi et al.

2009) and luminosity of the white dwarf to derive a distance of 211 ± 42 pc and from this they predict the companion is an L3 type brown dwarf or later. Assuming that this system is a LARP, Breedt et al. find the brown dwarf to have a mass of $0.04 < M/M_{\odot} < 0.12$ for and white dwarf mass of $0.75 M_{\odot}$ and a measured orbital period of 89 mins.

SDSS J121209.31+013627.7

SDSS J121209.31+013627.7 is the first magnetic (~ 13 MG) white dwarf + substellar companion binary system to be detected. It has a period of ~ 90 mins (Schmidt et al., 2005). A narrow $H\alpha$ emission feature has been detected coming from the brown dwarf atmosphere and is thought to be due to irradiation from the $\sim 10,000$ K white dwarf. Schmidt et al. (2005) mention (in a footnote) a possible detection of Na I (5893 \AA) but the infrared data is not good enough to confirm this. This system was thought to be accreting at a low rate via a wind from the brown dwarf (Debes et al. 2006; Burleigh et al. 2006). (Stelzer et al., 2017) confirmed accretion through their XMM-Newton detection of X-ray orbital modulation. This is proof of accretion from the substellar companion onto the magnetic white dwarf however the accretion rate of $3.2 \times 10^{-14} M_{\odot} \text{ yr}^{-1}$ is too large to be due to a wind therefore they conclude the mechanism of accretion is more likely to be Roche Lobe overflow.

SDSS J103532.98 +144555.8

This object was identified in the SDSS (Szkody et al., 2006) and follow up spectroscopy from the VLT and photometry from WHT revealed it to be an eclipsing binary. The companion was not directly detected, however, the eclipse allowed a full geometric and physical solution to be found (Littlefair et al., 2006). The orbital period is 82 mins and the mass of the white dwarf and its companion were found to be $0.94 M_{\odot}$ and $0.052 M_{\odot}$ respectively, thus placing the companion firmly in the sub-stellar regime. This is the first confirmed sub-stellar donor in a CV. An eclipse of the hot-spot (the region that matter is accreting onto) was also detected on the white dwarf. This confirmed the companion was overflowing its Roche Lobe and accretion was indeed occurring.

Littlefair et al. (2006) calculated an accretion rate of $(10 \pm 2) \times 10^{-12} M_{\odot} \text{yr}^{-1}$.

SDSS J150722.30 +523039.8

This system was the second confirmed CV with a brown dwarf donor; interestingly it has an orbital period of 67 min which is below the observed 'period minimum' of ~ 78 min for a CV (Littlefair et al., 2007). This suggests that the formation of this system is different from that of SDSS J103532.98 +144555.8. Littlefair et al. (2007) argue that this is because this system formed directly from a detached white dwarf–brown dwarf binary. However Uthas et al. (2011) have since shown that this is likely a halo object and the short period of this binary is due to the smaller radius of the metal-poor brown dwarf. This system is eclipsing which allowed the masses of the two bodies to be determined: $0.9 M_{\odot}$ white dwarf and a $0.056 M_{\odot}$ brown dwarf.

SDSS J105754.25 +275947.5

This system was first recorded as part of a search for CVs in the SDSS spectra released in 2006 (Szkody et al., 2009). It was found to present H and He emission lines and was eclipsing. (Southworth et al., 2015) found the orbital period to be 90.44 ± 0.06 mins and, using spectroscopy, they estimated the donor to be an L5 type brown dwarf. McAllister et al. (2017) used high speed multi-colour photometry to detect a bright spot eclipse on the white dwarf. From this the $13\,300$ K white dwarf was found to have a mass of $0.8 M_{\odot}$ and the brown dwarf, $0.04 M_{\odot}$. This is the lowest mass donor thus discovered.

NLTT 5306

NLTT5306 was identified by Girven et al. (2011) and Steele et al. (2011) who were searching for an infrared excess indicative of a substellar companion. Both Girven et al. (2011) and Steele et al. (2011) estimated the brown dwarf to be of spectral type dL5 with a mass of $58 \pm 2 M_{\text{Jup}}$ predicted by the DUSTY atmospheric models. The models were used because they account for

grain formation and dust in atmospheres < 5000 K. they take into account dust scattering and absorption in the radiative transfer equation, thus they are called DUSTY (Chabrier et al. 2000; Baraffe et al. 2002).

Follow up spectroscopy of this system by Steele et al. (2013) revealed NLTT5306 to be the shortest period white dwarf + brown dwarf binary system ($P = 101.88 \pm 0.02$ mins) known at the time. They found the white dwarf mass and effective temperature to be $0.44 \pm 0.04 M_{\odot}$ and 7756 ± 35 K, respectively and estimated the brown dwarf spectral type to be dL4 - dL7 with an effective temperature of ≈ 1700 K and a minimum mass of $56 \pm 3 M_{\text{Jup}}$. (Steele et al., 2013) discovered $H\alpha$ emission was present associated with the white dwarf and suggest it is due to accretion from the brown dwarf onto the white dwarf chromosphere.

SDSS J143317.78+101123.3

The first spectroscopically confirmed sub-stellar donor in a CV system was SDSS J143317.78 + 101123.3 with a $0.87 M_{\odot}$ WD and $0.055 M_{\odot}$ companion (Littlefair et al., 2013). The donor's spectral type was estimated to be $L1 \pm 1$ (Hernández Santisteban et al., 2016). K I absorption lines were detected coming from the companion atmosphere. Hernández Santisteban et al. (2016) also detected a temperature difference between the day and night side of ~ 60 K and found a maximum temperature difference between hottest and coolest parts of its surface to be ~ 200 K.

These rare white dwarf – brown dwarf are excellent systems for studying post-CE, pre-CV through to CV evolution. Furthermore, their mere existence demonstrates that an accreting white dwarf – brown dwarf binary is a viable configuration and these sub-stellar companions are well worth researching. The main system properties have been summarised in Tables 1.2 and 1.3 below.

Name	Type	WD mass (M_{\odot})	BD mass (M_{\odot})	WD T_{eff} (K)	BD T_{eff} (K)	Period (Min)	Reference
SDSS J121209.31 +013627.7	Polar	0.8	—	9500	< 1700	88.428 ± 0.001	Burleigh et al. 2006 Stelzer et al. 2017
EF Eridani	Polar	> 0.65	< 0.06	> 9500	< 2000	80.64	Beuermann et al. 2000 Schwope & Christensen 2010 Szkody et al. 2010
SDSS J151415.65 +074446.5	LARP	—	—	10 000	—	89	Külebi et al. 2009 Bredt et al. 2012
SDSS J125044.42 +154957.4	LARP	0.60	0.081 ± 0.005	10 000	—	86	Steele et al. 2011 Bredt et al. 2012

Table 1.2: A summary of the current known polars, low accretion rate polars (LARPs), and CVs with brown dwarf donors.

Name	Type	WD mass (M_{\odot})	BD mass (M_{\odot})	WD T_{eff} (K)	BD T_{eff} (K)	Period (Min)	Reference
SDSS J105754.25 +275947.5	CV	0.800 ± 0.015	0.0436 ± 0.0020	13300 ± 1100	–	90.44 ± 0.06	Szkody et al. 2009 Southworth et al. 2015 McAllister et al. 2017
SDSS J143317.78 +101123.3	CV	0.868 ± 0.007	0.0571 ± 0.0007	$12\,800 \pm 200$	2000 ± 200	78.11	Littlefair et al. 2008 Savoury et al. 2011 Littlefair et al. 2013 Hernández Santisteban et al. 2016
WZ Sagittae	CV	0.85 ± 0.04	0.078 ± 0.006	14 800	~ 1900	81.8 ± 0.90	Cheng et al. 1997 Ciardi et al. 1998 Patterson et al. 1998 Steeghs et al. 2007 Harrison 2016
SDSS J103532.98 +144555.8	CV	0.94 ± 0.01	0.052 ± 0.002	10100 ± 200	–	82.0896 ± 0.0003	Littlefair et al. 2006
SDSS J150722.30 +523039.8	CV	0.90 ± 0.01	0.056 ± 0.001	$11\,000 \pm 500$	< 2450	66.61	Littlefair et al. 2007

Table 1.3: A continuation of Table 1.2

1.6 Aims and objectives going forward

This work aims to address the following points,

- To spectroscopically investigate the close white dwarf - brown dwarf binaries WD0137-349 and NLTT5306.
- To determine if these systems can be used as exoplanet analogues to inform future exoplanet atmospheric models.
- To spectroscopically confirm new white dwarf - brown dwarf binary systems.

2

Instrumentation

The central aim of this thesis is to characterise brown dwarf atmospheres and see if the results can be used to inform our understanding of exoplanet atmospheres. Specifically, if brown dwarfs around white dwarfs can be used as exoplanet analogues. To do this requires spectra across a wide wavelength range that covers the UV (for the white dwarf) through to near-infrared (for the brown dwarf). For this reason nearly half of this work is based upon data taken using the XSHOOTER instrument on the Very Large Telescope (VLT), in Paranal, Chile. XSHOOTER was selected for its ability to observe in these three different wavelength ranges simultaneously: UVB, Visible (VIS), and Near-Infrared (NIR) covering a wavelength range of 300 – 2480 nm.

A third of this work is based upon spectra from the Gemini Near-Infrared Spectrograph (GNIRS)

also located in Chile. This instrument was also chosen for its large wavelength coverage (0.8 - 2.5 μm). It is a high quality, medium resolution spectrograph which is ideal for observing and spectral type-ing cool dwarfs, which is the aim of the final science chapter in this work.

Within this chapter I also discuss UV and X-ray observations obtain using *Swift*. Whilst the usefulness of high energy observations, with respect to exoplanet analogues, are not immediately obvious I discuss them because in Chapter 5 the XSHOOTER UV/optical data suggest a different research route needed to be explored. Specifically, the system may not address the initial aim of this project, it does prove very interesting as a laboratory for testing binary interaction with a substellar companion.

2.1 XSHOOTER

The XSHOOTER spectrograph is mounted at the ESO VLT-UT3 ('Melipal') telescope in Paranal, Chile (Vernet et al., 2011). XSHOOTER has three independent spectroscopic arms, UVB, VIS, and NIR. The incoming light is split into the different arms through two dichroics each arm is a cross dispersed echelle spectrograph. The UVB arm has a wavelength range of 300 – 559.5 nm, VIS has 559.5 – 1024 nm and NIR has 1024 – 2480 nm. A schematic can be seen in Figure 2.1.

2.2 Gemini Near-Infrared Spectrograph

The Gemini Near-infrared Spectrograph (GNIRS) is a multi-function spectrograph, covering a spectral range of 0.8-5.4 μm . It is mounted on one of two twin 8.1 m diameter optical/infrared telescopes and is located in and Chile.

Figure 2.2 is a schematic that demonstrates the optical path; for this work I used data taken with the short blue camera with a 32 l/mm grating, the short camera's cross-dispersing prism (SXD),

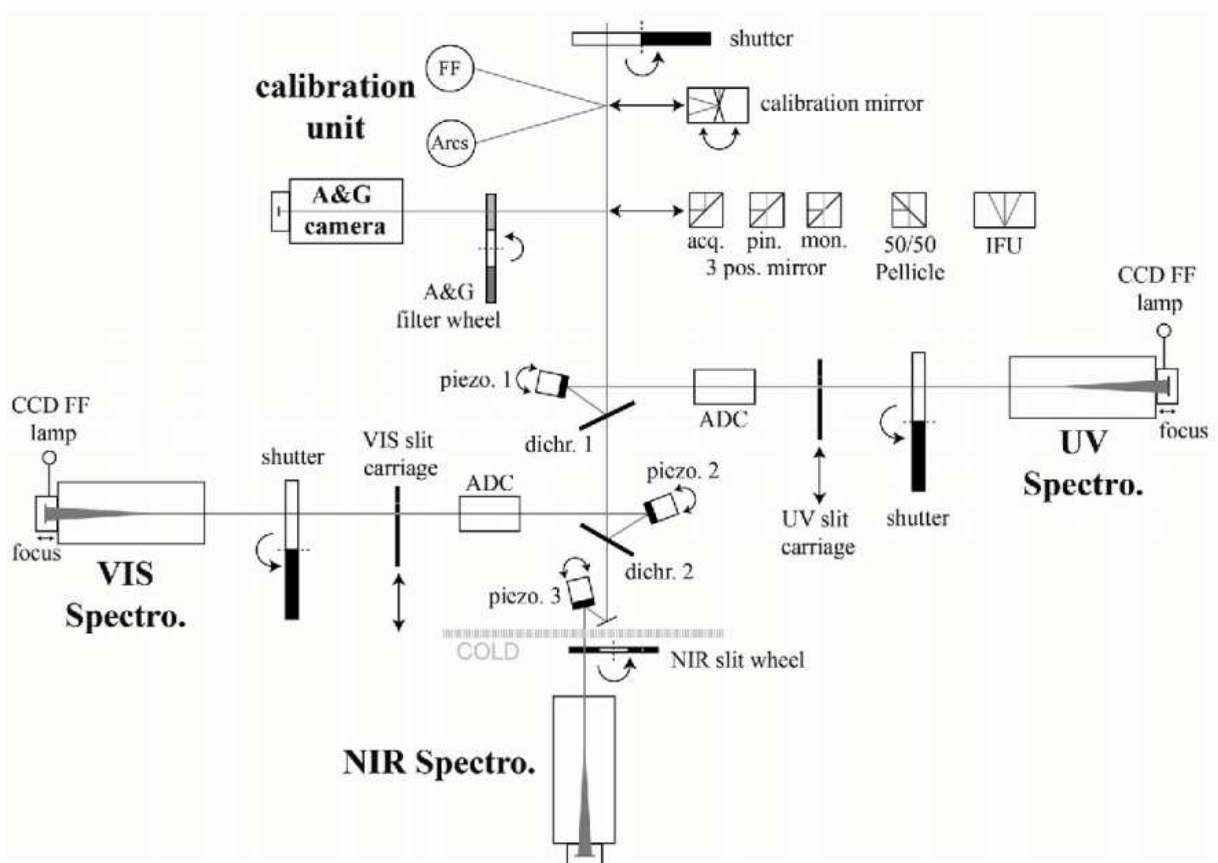


Figure 2.1: A schematic overview of the XSHOOTER instrument mounted at the VLT-UT3 telescope in Paranal, Chile. This illustrates the three arms: UVB, VIS, and NIR and how incoming lights is split to provide simultaneous observations in all three arms, thus covering a wavelength range of $0.3 - 2.4\mu\text{m}$. (Credit: ESO, <https://www.eso.org/sci/facilities/paranal/instruments/xshooter/overview.html>)

OPTICAL SCHEMATIC

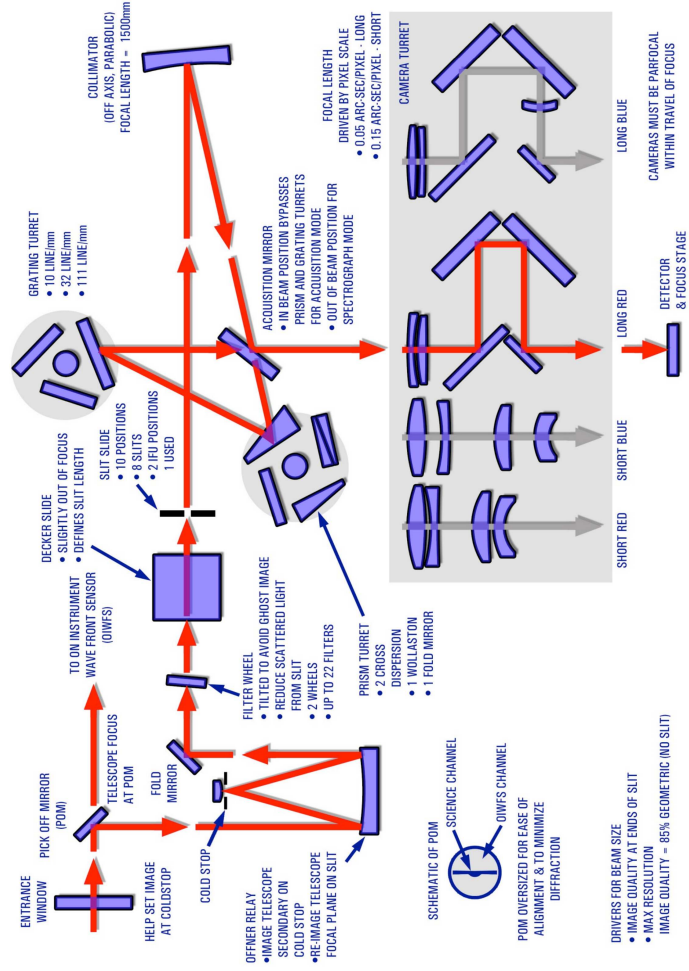


Figure 2.2: A schematic overview of the Gemini Near-Infrared Spectrograph (GNIRS) instrument mounted at Mauna Kea, Hawai'i. This illustrates how the incoming light passes through a filter and slit before reaching the detector.

Filter	Minimum wavelength (Å)	Maximum wavelength (Å)	Effective wavelength (Å)
W1	2589	1609	2589.1
M2	1679	2927	2254.8
W2	1593	3370	2613.7

Table 2.1: The minimum, maximum, and effective wavelengths of the three UVOT filters used (Rodrigo et al., 2012).

and a 7'' slit. In this mode short slit spectroscopy with full spectral coverage ($0.8 - 2.5\mu\text{ m}$) with resolution of up to 1,800 can be achieved.

2.3 Neil Gehrels Swift Telescope

Swift is a multi-wavelength space telescope in a 96 min low Earth orbit. It is known for its ability to slew rapidly onto new targets and is primarily used for the detection of gamma ray bursts. There are three instruments on board: UltraViolet/Optical Telescope (UVOT) (Roming et al., 2004), X-Ray Telescope (XRT) (Burrows et al., 2005), and the Burst Alert Telescope (BAT) (Barthelmy & Swift/BAT Instrument Team, 2004). Of these only UVOT and XRT were used in this work. UVOT has seven filters which gives a combined wavelength range of 170 - 650 nm. I made use of three of these filters, W1, M2, and W2 as they cover the shortest wavelengths (see Table 2.1). UVOT also has multiple modes of observation; image mode that takes a snapshot of the field of view (17×17 arcmin) for a given exposure time, and event mode which allows a single exposure to be split into smaller time bins. When an observation is performed with UVOT simultaneous observations are obtained with the XRT. The XRT has an energy range of 0.2 - 10 keV and a field of view of 23.6 arcmin square.

3

Data reduction and analysis techniques

In this chapter I will explain how I reduced and analysed the spectroscopic data for this work. First I will give a detailed description of the standard reduction techniques used. I will then demonstrate how I took these reduced data and further analysed them. For detailed observation specific information (e.g. dates, weather etc.) please see the relevant science chapter.

3.1 Spectroscopic reduction techniques

Spectroscopy refers to the measurement of incident flux as a function of wavelength. The reduction of the spectroscopic data in this work follows a specific procedure outlined below. For

XSHOOTER data I reduced it using the ESO pipeline and GASGANO (v2.4.3) (Izzo et al., 2004). For the GNIRS data I used the IDL-based data reduction package, Spextool 4.1 whose procedures are outlined in (Cushing et al., 2004) and Vacca et al. (2003a).

1. Bias correction

An image is taken with the telescope shutter closed the resulting image contains only noise from the electronics. Multiple bias frames are taken for each observation and combined to create a master bias frame which is subtracted from the data.

2. Flat field correction

Flat fielding removes the effect of the pixel-to-pixel sensitivity variations across the array, the effect of dust or scratches on the CCD, and vignetting by the telescope. This correction results in the throughput of each pixel on the CCD responding equally to the same flux input. The flat-field frames are obtained by imaging a continuum lamp at close range or the sky near dusk or dawn. Science data are then corrected by dividing the science data by the master flat. This way any temporal fluctuations can be attributed to the object and not the detector.

3. Flexure compensation

The direction and elevation of the telescope changes the temperature and pressure within it. Therefore the path of the light from the lens to the detector is dependent on the flexure induced by the pointing of the telescope. This can be compensated for by illuminating a pinhole with an arc-lamp and comparing the image with that of daily multi-pinhole calibrations; the small shift between the two can then be computed and corrected for. These are known as attached flexure compensation (AFC) frames and are usually taken before and after an observation, thus maintaining the pointing.

4. Flux calibration

A non-variable, standard star with a known and well defined spectrum is observed. Any de-

viations from the expected spectrum allow a response curve to be computed which converts non-calibrated counts into flux calibrated science frames. This process can also determine the overall efficiency of the detector.

5. Wavelength calibration

An arc lamp produces spectral lines of known wavelength. By taking an image of the lamp and determining if there is a shift. By applying this shift to all subsequent observations the spectra are wavelength calibrated. Images of the arc lamp at the beginning of a night's observation. Depending on the instrument and flexure, arc calibration frames may have to be taken whenever the pointing changes.

6. Telluric calibration

When observing from the ground the light from the source passes through the Earth's atmosphere. The atmosphere is mainly dominated by absorption lines known as telluric lines. These lines are caused by water, oxygen and hydroxide (OH) in the atmosphere and mainly affect the red and near-infrared wavelengths. Telluric absorption is spatially and temporally variable on short times scales; to account for this telluric standard stars are observed at approximately the same time, and therefore same airmass, as the science data. The telluric standards are typically Early to mid A, or B type stars and have very featureless spectra with few absorption lines in the wavelength regions where the telluric lines are present. A model spectrum is then divided by the telluric spectra to create a telluric correction function which is applied to the science data by multiplication. This process is not perfect; the affected wavelengths suffer due to low count rate therefore, the telluric wavelength ranges have lower signal-to-noise ratio than the less affected wavelength ranges.

7. Science frame reduction

Finally the results of the previous steps are applied to the science data typically in the order listed above.

In this work the spectra I have used have come from two instruments: XSHOOTER (Chapters 4

and 5) and Gemini Near-Infrared Spectrograph (Chapter 6). Each instrument comes with its own pipeline that performs these tasks, here I will describe each pipeline in turn and the individual steps I made for each.

3.1.1 Gasgano

Gasgano is a tool provided by ESO for the reduction of data from their telescopes. Gasgano automatically sorts all files into groups i.e. bias frames, flat frames, science frames, etc and these titles are clearly labelled. There is also a graphical user interface (GUI) that makes selecting the relevant files and executing the each step of the reduction process very straight-forward. The data reduction process is divided up into "recipes" that perform each reduction step in turn when given the correct input files. The outputs of each step cascade into the next step until you have a 1D extracted spectrum.

The first step is the creation of the master bias frame; all bias frames are input into the `xsh_ mbias` recipe along with a bad pixel map provided by ESO. Master bias frames are created for the UVB and VIS arms but for the NIR arm data a master bias is not computed, instead a master dark is created. This is done by giving all dark frames and a bad pixel map to the `xsh_ mdark` recipe and executing it.

To trace the orders Gasgano first generates guess line and order tables that predict the positions of arc-lines and order-edges on a format-check frame. This is done using a physical model of XSHOOTER that takes into account information on the atmospheric pressure, temperature and the instrument setting provided in the FITS header of the raw format-check frame. The format check frame, master bias (or dark) frame, and the arc line list are input into `xsh_ predict` and this recipe is executed. The output from this is fed into `xsh_ orderpos` which then accurately traces the order centres.

Once these steps had been completed it was possible to create a master flat for each of the arms using the `xsh_ flat` recipe. The data were taken in slit mode so I selected that mode for this recipe.

The master bias/dark and the table tracing order centres from previous recipes are required as well as all flat field frames taken during observations. This recipe creates a master flat frame, identifies hot and dead pixels, and traces the flat order edges.

For wavelength calibration `xsh_2dmap` recipe is used which determines the two-dimensional wavelength solution needed to resample the orders. This produces an image that contains the fitted wavelength corresponding to the centre of each pixel as well as an image that contains the position along the slit, in arcsec, relative to the slit's centre corresponding to the centre of each pixel.

Due to the size of XSHOOTER at different pointing the telescope flexes in different ways which subtly change the path of the light. To compensate for this the `xsh_flexcomp` recipe is used; it computes the instrument flexure. During observations attached flexure compensation (AFC) frames were taken, they are input into this recipe and output the flexure corrected model configuration and the flexure corrected dispersion table. This recipe is performed for each pointing and the output applied to the corresponding pointing i.e. individual science targets.

The data were taken in nod mode (where the telescope is nodded between two points to improve sky subtraction) so when computing the instrument response curve I used the `xsh_respon_slit_nod` recipe. This required a master bias frame, master flat frame, and a flux standard star and outputs the instrument response and the telescope + instrument + detector efficiency.

Each recipe thus far was performed for each of the arms, UVB, VIS, NIR unless otherwise stated. The final step is to combine the spectra and extract the 1D spectrum for each arm. The data were taken in nodding mode in an ABBA pattern, so for the NIR extraction I used `xsh_scired_slit_nod` which combines the four ABBA frames and extracts the spectrum. For the optical arms the signal-to-noise ratio was good enough for the ABBA frames to be extracted individually using `xsh_scired_slit_stare`. For this the file names need to be changed from `OBJECT_SLIT_NOD_ARM` to `OBJECT_SLIT_STARE_ARM`, this is very easily done within the recipe window. Also the `localize-slit-position` parameter needs to be changed to reflect the position of the object on the slit. For A frames I set it to 2.5 and for B frames I set it to -2.5. For both extraction recipes the

input science frames must all have the same exposure time.

In all recipes I matched the binning and read-out mode for all the input files. For example, I created three master bias frames: 1x1 binning and readout = 100k, 1x2 binning and readout = 100k, and 1x1 binning and readout = 400k. When a master bias frame was required in further steps I would select the relevant binning and readout based on the other key files being input into that recipe. For example in the extraction of the science data, the data were taken with 1x1 400k so I used the corresponding master bias and master flat. Again, the Gasgano GUI makes this selection very simple and the recipe will not execute successfully unless the correct files (with the correct binning and readout mode) have been selected.

3.1.2 SpeXTool

The reduction process for the Gemini data used an IDL based pipeline with three main recipes: *xspextool*, *xcombspec*, and *xtellcor_general*. I will detail each process in turn.

The raw Gemini data has a naming system of "rootname_ filenumber" and the file type with it's corresponding file number can be found in the observation logs. By inputting the root name into *xspextool* subsequent processes then only require the relevant numbers to complete the reduction tasks. *xspextool* first computes the master flat from the flat field frames by inputting the correct file numbers and pressing "construct flats". The wavelength calibration is performed by providing arc file numbers and pressing *createlinecalfile* this opens a separate window where the user can select spectral lines which creates a line calibration file and the wavelength calibration is performed by pressing "wavelength calibrate".

xspextool is a pipeline for many different types of extraction, for this work I selected "Point Source" as that is most appropriate for these data. This is where the science frames are flat-fielded, wavelength calibrated and then extracted. The data were taken in AB pairs and thus are reduced in pairs. I input the file numbers and the master flat and wavelength calibration files and press "Load Image" and then "Make Spatial Profile". The next step is to select the apertures which is triggered

by pressing, "Find/Store Ap Positions". A separate window will appear with the apertures plotted and the user can inspect the fits. If the signal-to-noise is too great and the fit has not found the aperture it can be selected by hand by changing the Aperture Mode to "per order" and pressing 's' to individually select each aperture. Once I was happy with the aperture selection I pressed "Fix" and "Find/Store Aperture positions" before pressing "Trace" and viewing the traces using "Show Apertures", and then pressing "Extract Spectra". I did this for all the science and telluric frames.

To combine the individual extracted spectra I used *xcombspec*. I selected the manual method and input the relevant file numbers to be combined. I pressed "Scale Spectra" and scaled the spectra to median so the order align. I did not perform any pruning of the spectra. I then pressed "Correct spectral shape" to apply the changes. By the end of this step I had 1D combined and extracted science and telluric data.

I performed the telluric correction using *xtellcor_general*. For each science object I used the relevant telluric spectrum. I input the B and V magnitudes of the telluric object and pressed "scale lines" and then "construct telluric spectra". This opens up a separate window where one can mask out the hydrogen lines from the telluric spectrum before it is applied. Then the telluric corrected science data are written to file by pressing "Write file".

3.2 Data Analysis

I made use of a software package called MOLLY. MOLLY reads in 1D spectral data and can perform simple arithmetic tasks. Given the relevant headers (MJD, HJD, etc.) MOLLY can also reorder the spectra. MOLLY has the ability to model individual spectral features with a routine called, MGFIT. This routine can fit multiple Gaussians to a spectral feature with a specified central wavelength, it uses Levenberg-Markquadt minimisation. As the routine runs each spectrum is taken in isolation thus the calculated errors are based upon how well the MGFIT is able fit that spectral line. For this reason I exported the measured radial velocities from MGFIT and did a more thorough statistical analysis to determine the ephemeris using an IDL routine, called MPFIT,

to measure the uncertainty on each radial velocity point. I will elaborate on this method in the following section.

3.2.1 MOLLY

MOLLY is a stand alone program written by Tom Marsh¹ and is used for handling 1D spectroscopic data. It is useful for handling large numbers of similar spectra and contains many standard operations used for spectrum analysis.

3.2.2 Initial processing

Data were read into MOLLY and corresponding headers including ra, dec, UTC, and airmass were applied to each file. A heliocentric correction was applied to account for the location of the telescope on Earth. Typical spectra can be seen in Figure 3.1. Next the spectra were normalised to a continuum level of 1; this was done by averaging all of the spectra, masking out large features like absorption lines (red sections fig. 3.1), and fitting a polynomial to that average (the green lines in fig 3.1). The individual spectra were then divided by this polynomial and the result can be seen in Figure 3.2. The data were rebinned onto a velocity scale in the heliocentric frame to account for the Earth's velocity and then put into phase order. Phase, ϕ , was calculated by subtracting the zero point of the ephemeris, T_0 in HJD, from the time of the observation, t also in HJD, and dividing by the period, P in days,

$$\phi = \frac{t - T_0}{P}. \quad (3.1)$$

The zero point of the ephemeris is selected by the observer and can be any point in an orbit. For binaries the zero point is typically selected to be when the lower mass object is closest to the observer.

¹<https://warwick.ac.uk/fac/sci/physics/research/astro/people/marsh/> University of Warwick, UK

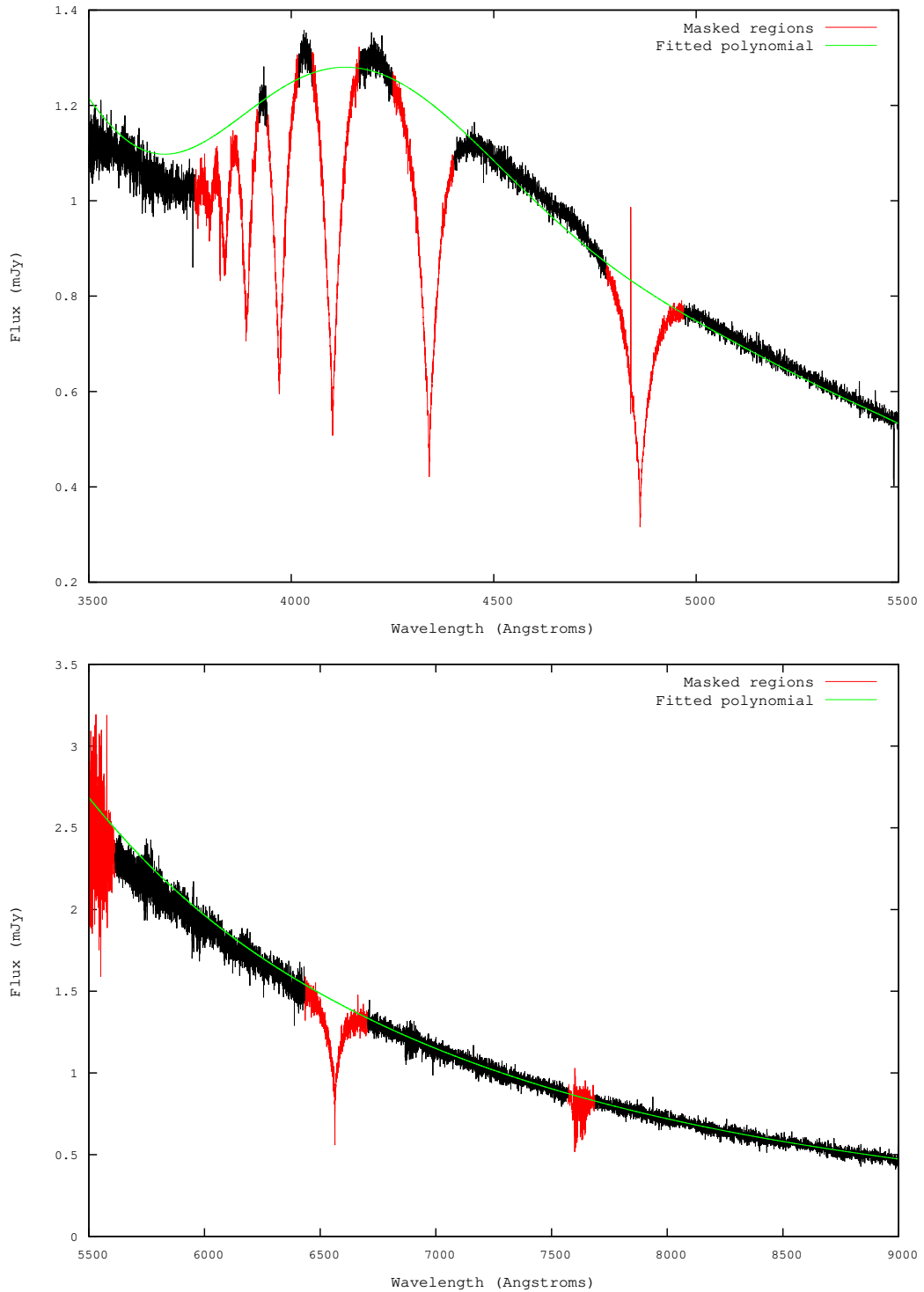


Figure 3.1: UVB (top) and VIS (bottom) XSHOOTER reduced spectra before being normalised. The red sections were masked out when fitting the polynomial (green) that was used to normalise the data.

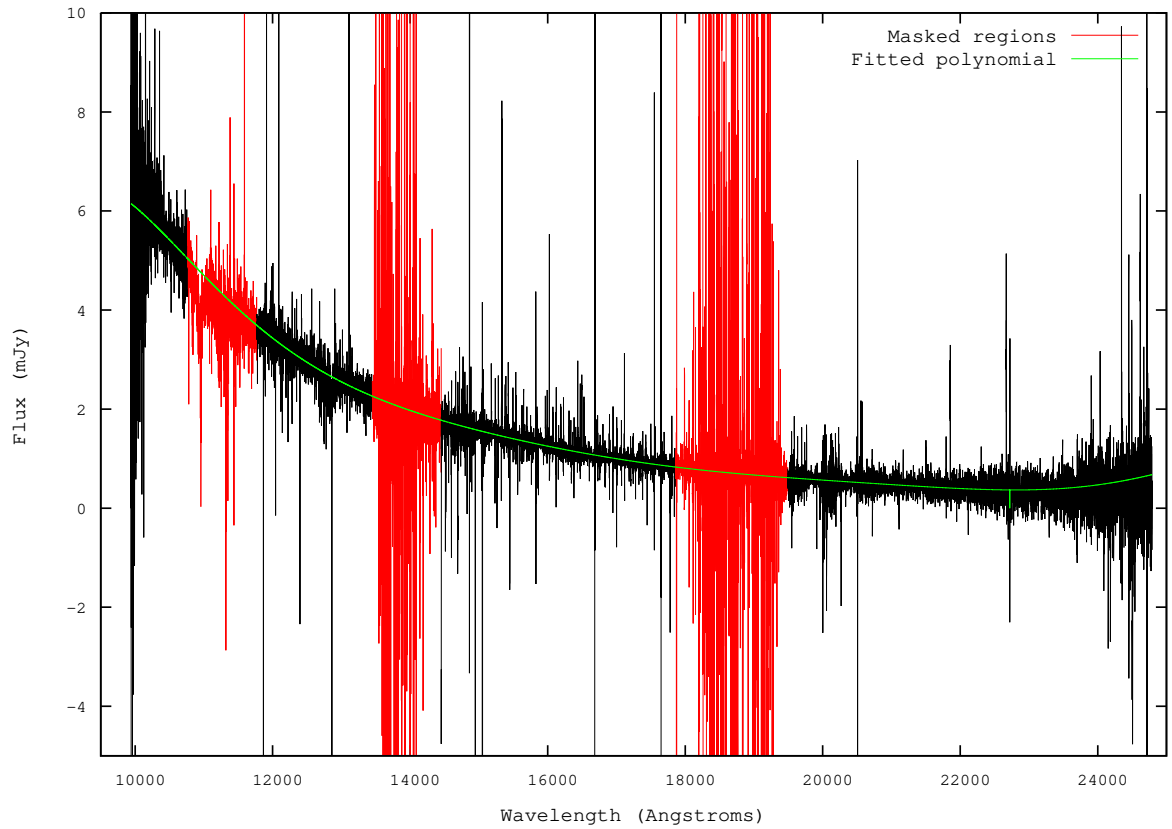


Figure 3.2: NIR XSHOOTER spectra before being normalised. The large number of bad pixels made clear in this plot are due to the bad pixels in the original frame. Their presence does not affect the results of this work. This plot is to illustrate the regions masked out to fit a polynomial.

3.2.3 Measuring radial velocity

Radial velocity is the the velocity of an object along the line of sight of the observer. As the object moves away from the observer the wavelength of the emitted light is lengthened (red-shifted), and as it moves towards the observer the wavelength is shortened (blue-shifted). Thus, at different phase points, spectral lines are detected at different wavelengths; this is also known as Doppler shift. It is clear from Figure 3.3 that the emission lines are being red- and blue-shifted about the black vertical line that indicates the rest wavelength. By measuring this shift the radial velocity can be determined using,

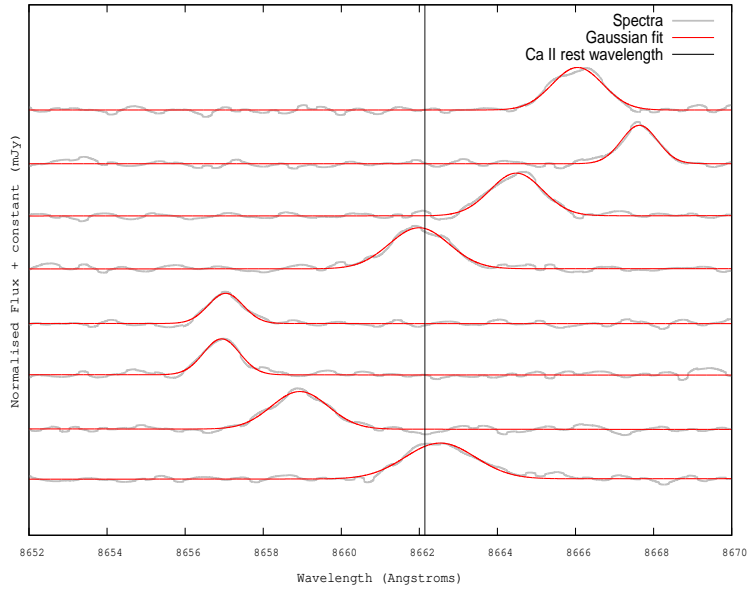


Figure 3.3: An example of an emission line (grey) being red- and blue-shifted about its rest wavelength (black vertical line) and the models fitted to each line to measure radial velocity (red).

$$\frac{\Delta\lambda}{\lambda_0} = \frac{v}{c} = z, \quad (3.2)$$

where $\Delta\lambda$ is the wavelength shift, λ_0 is the rest wavelength, v is the relative velocity, c is the speed of light, and z is the red-shift.

This method was used for all spectral line fitting in this work; for clarity I will use two key examples: a single emission line Ca II (8662.14 Å) and H α which can have both absorption and emission lines and therefore offers some complexity.

Figure 3.3 shows the Ca II 8662.14 Å emission line. To measure the radial velocity I used MGFIT within the MOLLY package. MGFIT uses an input file to define all the parameters used in the fit. The file includes the set up of a polynomial with a pivot wavelength and coefficients indicating the gradient and constant of the polynomial. This was for modelling the flat continuum. Next a Gaussian was set up with a central wavelength in Å, velocity offset in kms^{-1} , full width half maximum (FWHM) in Å, and a peak height in mJy. Each variable was given a starting value and MOLLY uses a Levenberg-Marquardt method of minimisation to fit the Gaussian to the emission

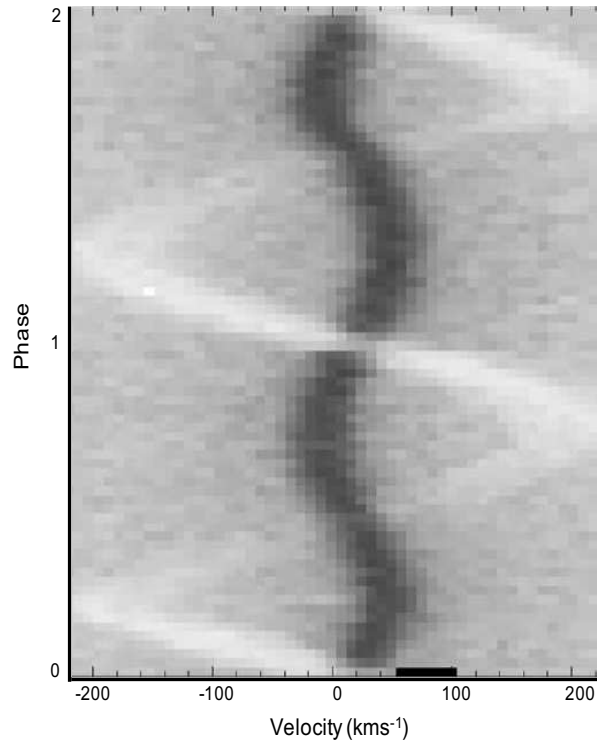


Figure 3.4: Each horizontal slice is one spectrum and by stacking these slices above one another one can see how the spectral features move with time; this is known as trailing. This trail shows the $H\alpha$ line, the absorption feature is black and the emission feature is white. The x-axis is radial velocity with 0 centred on the central wavelength of the $H\alpha$ line at 6562.76 \AA .

line. The fit was applied to each spectrum individually and reset to the initial values for each spectrum. Figure 3.3 shows 8 spectra with their associated fits.

The Ca II line is a relatively simple example because the continuum surrounding the emission line is mostly flat and there is only one line present and therefore only one Gaussian was required. The $H\alpha$ line at 6562 \AA however is more complex; it has both emission and absorption components. To visualise this I phase-folded and plotted each spectrum in a stacked fashion to trace or "trail" the movement of spectral lines. This is known as a trailed spectrum. This trail is plotted in velocity space so the movement of the two components of the $H\alpha$ line is much clearer. It can also be seen, from the bottom panel of Figure 3.1, that the $H\alpha$ absorption line has broad wings and a narrow core; a single Gaussian is not sufficient to model this. Figure 3.5 demonstrates how I used

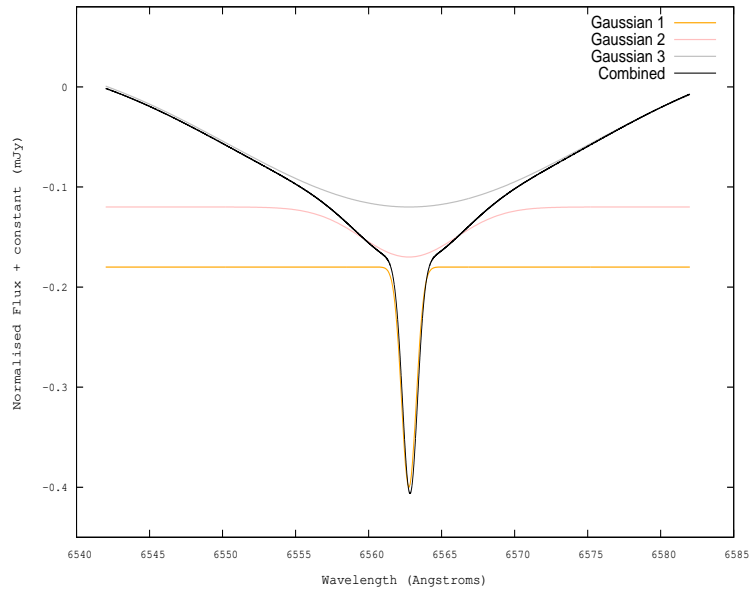


Figure 3.5: The three Gaussians required to model the $H\alpha$ absorption line with the total model over-plotted (black). The $H\alpha$ line has this shape because the line has been pressure broadened within the white dwarf atmosphere.

a combination of three Gaussians to model the absorption line: two for the wings (grey and pink) and one for the narrow core (orange). This model was combined with a fourth Gaussian to model the emission line.

To determine the parameters of each Gaussian I used a routine within MOLLY called *mgfit* to fit the $H\alpha$ absorption line. I created an input file in this form:

```
poly: 6562.76 $c0 $c1
gaussian: 6562.76 $rvwd $fwhm1 $height1
gaussian: 6562.76 $rvwd $fwhm2 $height2
gaussian: 6562.76 $rvwd $fwhm3 $height3
$c0 = 1.0
$c1 = 0.0
$rvwd = 0.0
$fwhm1 = 100
```

```

$fw hm2 = 10
$fw hm3 = 1
$height1 = -0.05
$height2 = -0.15
$height3 = -0.25

```

The first line sets the parameters for a polynomial that is fit to the continuum around the absorption line. The following three lines then set up each of the individual Gaussians with their central wavelengths in Å, and variables; radial velocity, full-width half maximum (FWHM), and height (or depth in this case). All three Gaussians have the same \$rvwd variable set this removes degeneracy. The values listed for each variable are examples of the initial values that *mgfit* uses as a starting point for each fit. I fit each spectrum individually and reset to initial values each time.

I performed a first test leaving all variables free and reviewed the calculated best fitting values for each variable, this way I determined which values needed to be changed/fixed. For example I found the narrowest Gaussian was not reaching the deepest point of the H α absorption line so I changed the \$height3 to -0.3 and put "F" for fixed after it and re-ran *mgfit*. This way I was able to get a much better fit to the H α absorption line.

From Figure 3.4 it is clear the H α emission line has a much larger radial velocity than the absorption line and therefore simply adding another Gaussian with a starting radial velocity of 0.0, as was done with the absorption feature, will not be sufficient because the starting value is too far from the solution.

To adequately fit the emission line the initial conditions of its radial velocity needed to be set to a value closer to the actual value in each spectrum. To get an estimate of the radial velocity of the emission line in each spectrum I used the *sine* routine within MOLLY which measures the sinusoidal velocity of the emission line given by,

$$v = \gamma - K_x \cos(2\pi\phi) + K_y \sin(2\pi\phi), \quad (3.3)$$

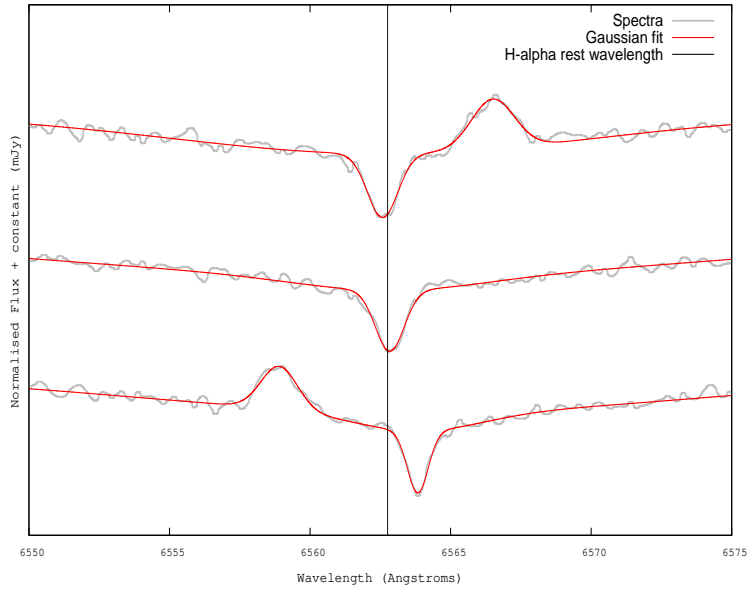


Figure 3.6: Three example fits of the full model of the H α line. Each fit includes the three Gaussians from Figure 3.5 with the addition of a fourth Gaussian for the emission line.

where v is the velocity, γ is the systemic velocity, K_x and K_y are the amplitudes of the cosine and sin, and ϕ is the orbital phase described in Equation 3.1. I used the systemic velocity and amplitude of the H α emission given in (Maxted et al., 2006). This provides a list of velocities which I added to the headers of each spectrum for *mgfit* to access when fitting the emission line. I edited the input file to include *gaussian: 6562.76 \$offset+BDRV \$fwhm4 \$height4* and set $\$offset = 0.0$. BDRV is the header value that estimates what the radial velocity of the emission feature is for that spectrum and then *mgfit* determines the $\$offset$. $\$offset+BDRV$ is therefore the radial velocity of the H α emission line. Figure 3.6 displays an the fit achieved via this method for three example spectra.

3.2.4 Refining the ephemeris

To determine the ephemeris of a system the radial velocity, V_r , and the time, t , of the observations are required for at least one spectral line. These values are then fit to,

$$V_r = \gamma + K_y \sin\left(2\pi\left(\frac{t - T_0}{P}\right)\right) = \gamma + K_y \sin(2\pi\phi), \quad (3.4)$$

to determine the systemic velocity in kms^{-1} , γ , the semi-amplitude in kms^{-1} , K_y , the zero point of the ephemeris, T_0 , and the orbital period of the system, P . To achieve this I used the IDL package MPFIT. This employed the Levenberg-Marquardt technique to solve the least-squares problem by fitting a given model (Equation 3.4) to the data (V_r and t) by adjusting a set of parameters (γ , K_y , T_0 , and P). MPFIT allows for upper and lower bounds to be placed on each parameter, alternatively the parameter can be held fixed.

3.2.5 Measuring equivalent width

A vast amount of information can be obtained simply from the shape of an individual spectral line. The shape can reveal the strength of the line and information about the environment from which it was formed. The strength of a particular line can be measured by calculating its equivalent width. The equivalent width is the width a rectangle would have if it has a height equal to the continuum emission and an area equal to the area of the spectral line. Mathematically it can be found by,

$$W = \int \frac{F_c - F_\lambda}{F_c} d\lambda, \quad (3.5)$$

where F_c is the continuum flux, F_λ is the flux of the spectral line, and the integral is taken from either side of the line. According to this definition an emission line would give a negative width as the area under the line is counted negatively. The reverse is therefore true for an absorption line.

For each emission line, other than the $H\alpha$ line, a flat continuum spectrum was defined as is demonstrated, in red, in Figure 3.7. I integrated over each emission line using equation 3.5. For the $H\alpha$ feature the absorption component had to be removed before EW could be determined. This was done by fitting only the absorption feature and then subtracting this from the total spectrum as

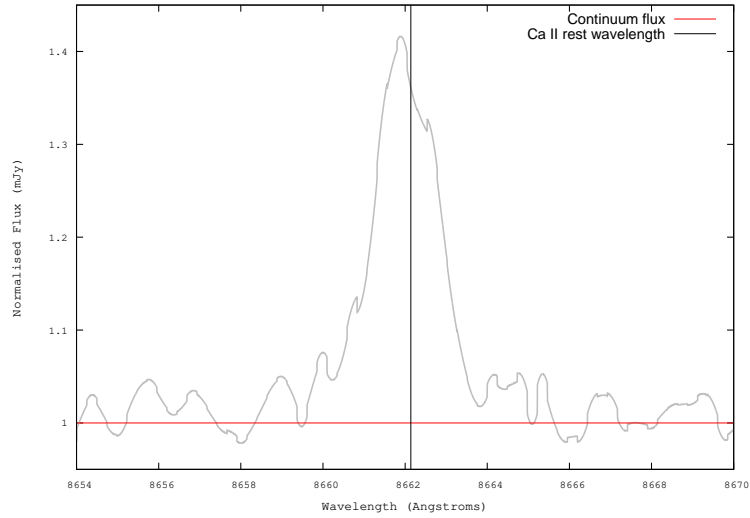


Figure 3.7: **Upper:** An example spectrum of a Ca II emission line (grey) that has been normalised to put the continuum flux level at 1 and this has been highlighted in red. This plot demonstrates the area that is determined when calculating the equivalent width of a line.

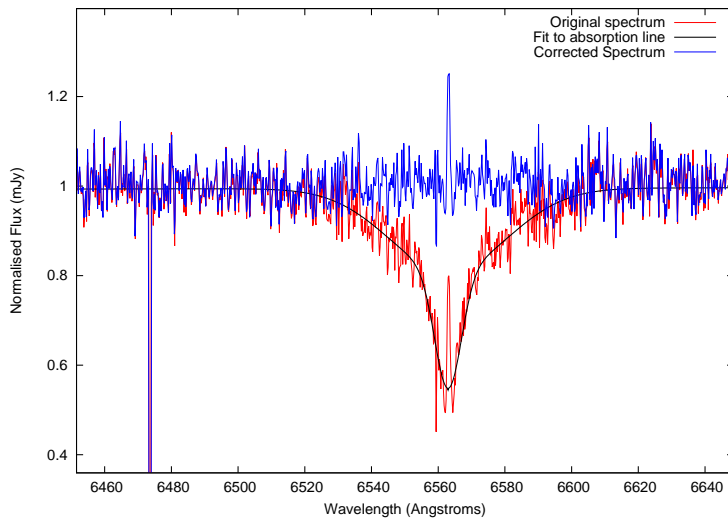


Figure 3.8: The original spectrum (red) centred on the $H\alpha$ line with the fit to just the absorption feature (black). This fit was subtracted from the total spectrum to leave only the emission feature (blue).

demonstrated by Figure 3.8. From this Figure it can be seen that the $H\alpha$ model does not quite reach the bottom of the absorption feature. This would mean that when subtracted the emission feature would be slightly larger. However, when calculating the EW the continuum is set so that this "extra" flux is not included in the final estimation of the line strength.

3.2.6 Modelling white dwarf spectra using TLUSTY

TLUSTY is a plane-parallel, hydrostatic, non-LTE atmosphere code that is used to model stellar atmospheres (Hubeny & Lanz, 1995; Lanz & Hubeny, 2003). TLUSTY solves the basic equations of radiative transfer, hydrostatic equilibrium (HSE), radiative equilibrium, statistical equilibrium, charge and particle conservation.

Typically TLUSTY models are fit to spectra to determine their T_{eff} and surface gravity, in this work however that is not the case. The T_{eff} and $\log g$ of the white dwarfs are already well known, so the TLUSTY models will be used to represent the white dwarf component of the candidate white dwarf - brown dwarf binaries. A mixing length parameter, $\alpha = 0.6$ has been adopted for all models which includes a treatment for convective energy transport according to the mixing length 2 (ML2) prescription of (Bergeron et al., 1992). Convective energy transport describes the bulk movement of particles from the stellar interior outwards due to a temperature gradient. The mixing length parameter can introduce some uncertainty because it effectively determines the amount of flux in the region being examined, by keeping this value the same for all allows fair comparisons to be made. These calculations utilised a model H atom which incorporates explicitly the eight lowest energy levels and represents levels $n = 9$ to 80 by a single super level. The ionisation levels of H are very well understood and therefore contribute negligible uncertainty to the final models produced.

To create a non-LTE model of a stellar atmosphere TLUSTY computes a series of models that increase in complexity; starting with a LTE model atmosphere with a non-frequency dependent (grey) opacity from given T_{eff} and $\log g$. Next TLUSTY self-consistently calculates the non-LTE population where all lines are assumed to be in detailed radiative balance. Finally the full non-

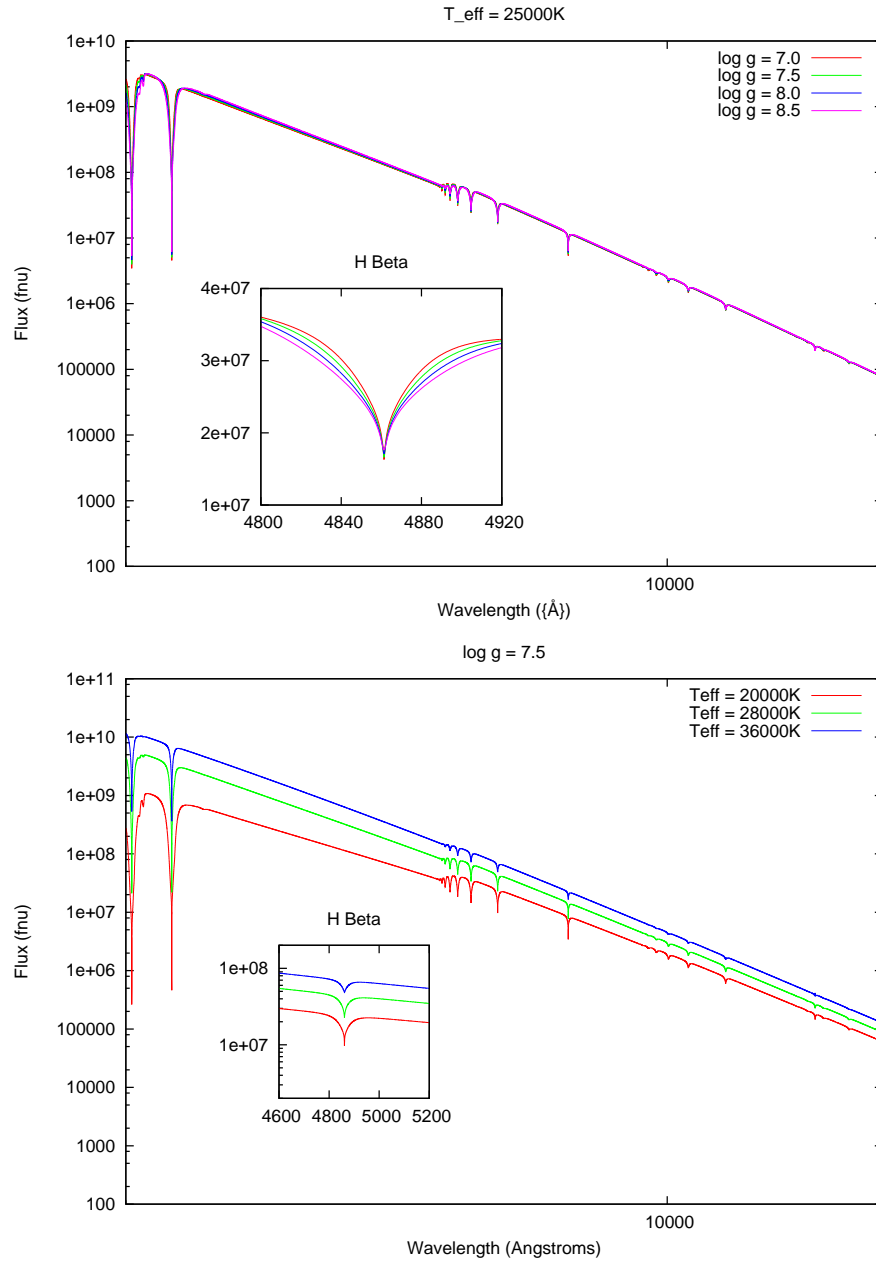


Figure 3.9: Example white dwarf models created using TLUSTY and synthesised with SYNSPEC. The top plot shows models with consistent effective temperature and different surface gravities. The bottom plot shows models with the same surface gravity but different temperatures. The y-axis for both plots is in $f\nu$ units which means energy per frequency. the inserts in both plots highlight the results of varying the surface gravity and temperature, respectively.

LTE model is computed where lines are considered explicitly. For DA white dwarfs only H needs to be considered when calculating the opacities. For this work I set the Rosseland optical depth to go from 1×10^{-8} to 500. Optical depth describes how opaque a medium is to radiation passing through it and is dependant on the mean free path of a photon: high optical depth indicates high opacity and a small mean free path. The Rosseland approximation defines an average absorption coefficient (or average opacity) which allows for an approximation of the total flux to be computed. These values were chosen to range from the high optical depth, where LTE effects are dominant, to low where non-LTE is true and all transitions are included.

Synthesising a spectrum using SYNSPEC

SYNSPEC (Hubeny & Lanz, 2011) is a general spectrum synthesis program that can take in model atmosphere computed by TLUSTY and synthesize a spectrum in the wavelength range required. This process is based on the physical parameters of the model atmosphere itself. The lines are broadened based on the Tremblay-Bergeron tables (Tremblay & Bergeron, 2009) as these are the most accurate for high density models such as white dwarfs. Figure 3.9 shows example synthetic spectra produced through the use of TLUSTY and SYNSPEC. The upper panel shows a series of spectra with a constant T_{eff} and different surface gravities at a first glance they look almost identical. From the insert it can be seen how surface gravity broadens the spectral lines. The bottom panel is a series of spectra with constant surface gravity and different T_{eff} ; here the line widths stay the same but the flux level changes. This change can be seen observationally in the strength of the lines. Another observational change is known as the Balmer jump. This is the difference in intensity of the stellar continuum on either side of the limit of the Balmer series of hydrogen at 3646 \AA . When electrons are completely ionized directly from the second energy level of a H atom a continuum absorption is created at wavelengths shorter than 3646 \AA . The strength of this continuum absorption, and therefore the size of the Balmer jump, depends on the temperature and density in the region of the star responsible for the absorption. At cooler stellar temperatures, the density most strongly affects the strength of the discontinuity from one side to another.

These codes are used in Chapter 6 to model eight new white dwarf - brown dwarf candidates.

4

Emission lines in the atmosphere of the irradiated brown dwarf: WD0137-349B

The work presented in this chapter is published in Longstaff et al. (2017). The aim of this chapter is to investigate the atmosphere of WD0137-349 and see if the results can be used to improve our understanding the irradiated atmospheres of other low mass objects i.e. gas giant planets.

4.1 Abstract

I present new optical and near-infrared spectra of WD0137-349; a close white dwarf - brown dwarf non-interacting binary system with a period of ≈ 114 minutes. I have confirmed the presence of $H\alpha$ emission and discovered He, Na, Mg, Si, K, Ca, Ti, and Fe emission lines originating from the brown dwarf atmosphere. This is the first brown dwarf atmosphere to have been observed to exhibit metal emission lines as a direct result of intense irradiation that has caused a temperature inversion in the brown dwarf atmosphere. The equivalent widths of many of these lines show a significant difference between the day and night sides of the brown dwarf. This is likely an indication that efficient heat redistribution may not be happening on this object, in agreement with models of hot Jupiter atmospheres. The $H\alpha$ line strength variation shows a strong phase dependency as does the width. I have simulated the Ca II emission lines using a model that includes the brown dwarf Roche geometry and limb darkening and I estimate the mass ratio of the system to be 0.135 ± 0.004 . I took the result of a gas-phase equilibrium code that used a prescribed DRIFT-PHOENIX model to examine how the chemical composition of a brown dwarf upper atmosphere would change given an outward temperature increase. Finally I discuss the possibility that this would induce a chromosphere above the brown dwarf atmosphere.

4.2 Introduction

WD0137-349 is described in detail in Chapter 1 Section 1.5.1. To summarise WD0137-349 is a non-interacting, non-eclipsing white dwarf - brown dwarf binary system. The white dwarf has an $T_{\text{eff}} = 16\,500$ K, a $\log g = 7.49 \pm 0.08$, and period of 114 minutes. The substellar companion has a spectral type of L6 – L8, a temperature of $1300 < T_{\text{eff}} < 1400$ K, and a mass of $0.053 M_{\odot}$. The brown dwarf is tidally locked resulting in one side being continually irradiated giving the brown dwarf a temperature difference of 500 K between its "night-" and "day" – side (Casewell et al., 2015).

4.3 Observations

78 spectra (3.7 orbits) of WD0137-349 were obtained using the XSHOOTER telescope mounted at the ESO VLT-UT3 ('Melipal') in Paranal, Chile (Vernet et al., 2011) (See Chapter 2 for full description of XSHOOTER specifications). The observations took place on the nights of 2014-08-28 between 04:45 – 09:45 and 2014-08-29 between 04:35 – 07:12 universal time. Bias and flat-fields were taken at the beginning of each night. Flexure compensation frames were taken every two hours. The flux standard used was GD71; a hot DA1 white dwarf.

The 78 exposures, each 300 s long, were taken covering 2.4 orbits on the first night and 1.3 orbits on the second night. This gave 21 spectra per full orbit. The weather conditions on the first night were good with an airmass ranging between 1.02 – 1.33 and seeing of 0.98". The second night the weather was not as good due to a high wind of 13 ms^{-1} at the start of the night and slowing to 8 ms^{-1} . The airmass ranged between 1.02 – 1.58 and the seeing between 0.63 – 1.1 arcsec.

4.4 Data Reduction

The data were reduced and calibrated using GASGANO (v2.4.3) (Izzo et al., 2004) and ESO's XSHOOTER pipeline (v2.5.2) using the spectroscopic data reduction procedures described in Chapter 3. The science data were taken in slit nodding mode in the sequence A-B-B-A where the localised slit position is -2.5 arcsec for A and 2.5 arcsec for B frames. The signal-to-noise ratio is sufficiently high in UVB and VIS wavelengths that each frame could be reduced independently using slit stare mode. This was performed manually by changing the localised slit position for the A and B frames appropriately. This allows for better time resolution for determining the radial velocity. The signal-to-noise of the NIR is not as high and therefore these spectra were reduced by combining each A-B-B-A set in slit nod mode.

4.5 Data Analysis

The data were analysed with molly as described in Chapter 3. The reduced science frames were heliocentric corrected, normalised to a flux of 1, and the radial velocity of the spectral lines were measured. The data from the two nights were analysed together and separately and no significant difference was found between the two. Therefore I analysed of both nights together.

The measured radial velocities for the $H\alpha$ absorption and emission lines are listed in Table 5.1. The best fitting widths and depths of the three Gaussians used to model $H\alpha$ absorption line were found to be 0.149, 2.360, 8.30 nm and -0.24, -0.13, -0.12 mJy, respectively.

To refine the ephemeris of this system I used the method described in Chapter 3 Section 3.2.4. When fitting the $H\alpha$ absorption line I allowed all four parameters (γ, K_y, T_0, P) to roam. Any points more than 3σ away from the model were excluded to improve the fit. 1 kms^{-1} was added in quadrature to the standard statistical errors listed in Tables 5.1 and 4.2 until a reduced χ^2 of 1 was achieved.

Once the ephemeris was determined P and T were held constant for fitting all other spectral lines. The other lines were passed through the IDL MPFIT code to improve upon the purely statistical errors from MOLLY and to phase fold the data onto the newly determined orbital period.

Finally the equivalent widths were calculated for each line using the method described in Chapter 3 Section 3.2.5 and are listed in Tables 4.3 – 4.5 below.

4.6 Results

Figure 4.1 shows the result of the radial velocity analysis and fitting, it has been phase folded onto the new ephemeris determined from the fit of the $H\alpha$ absorption line.

HJD	$V_r(\text{abs})$	$V_r(\text{em})$	HJD	$V_r(\text{abs})$	$V_r(\text{em})$
-2450000	[km s ⁻¹]	[km s ⁻¹]	-2450000	[km s ⁻¹]	[km s ⁻¹]
6898.7591	35.8 ± 1.0	-69.4 ± 1.6	6898.7197	16.5 ± 1.2	48.5 ± 1.6
6898.8402	33.6 ± 1.0	-99.2 ± 1.6	6898.8804	14.2 ± 1.0	51.8 ± 1.4
6898.7630	40.9 ± 1.0	-118.1 ± 1.6	6898.7236	2.4 ± 1.1	132.3 ± 1.6
6898.8440	37.4 ± 1.0	-144.0 ± 1.6	6898.8844	-5.3 ± 1.0	135.9 ± 1.5
6898.7668	46.0 ± 1.0	-159.7 ± 1.6	6898.7274	-3.7 ± 1.1	163.7 ± 1.6
6898.8480	45.7 ± 1.0	-175.5 ± 1.6	6898.8882	-11.2 ± 1.0	184.6 ± 1.6
6898.7706	49.8 ± 1.1	-179.7 ± 1.7	6898.7314	-5.6 ± 1.1	188.1 ± 1.7
6898.8518	43.8 ± 1.1	-190.1 ± 1.7	6898.8922	-12.4 ± 1.2	199.5 ± 1.8
6898.7745	47.8 ± 1.0	-195.3 ± 1.6	6898.8129	-10.3 ± 1.1	203.8 ± 1.7
6898.8557	48.6 ± 1.1	-192.9 ± 1.6	6898.7352	-8.1 ± 1.1	203.9 ± 1.7
6898.7783	47.2 ± 1.0	-178.3 ± 1.6	6898.8960	-9.3 ± 1.2	195.6 ± 1.8
6898.7823	43.9 ± 1.0	-147.7 ± 1.6	6898.8168	-10.6 ± 1.0	193.8 ± 1.7
6898.7042	40.8 ± 1.3	-127.0 ± 2.0	6898.7391	-6.2 ± 1.1	191.3 ± 1.7
6898.8650	36.7 ± 1.0	-124.2 ± 1.5	6898.8998	-9.8 ± 1.1	173.6 ± 1.7
6898.7861	38.8 ± 1.0	-136.6 ± 1.5	6898.8206	-6.5 ± 1.0	173.8 ± 1.6
6898.7082	34.0 ± 1.2	-128.5 ± 1.7	6898.7429	-3.4 ± 1.1	164.7 ± 1.7
6898.8688	25.5 ± 1.0	-83.5 ± 1.4	6898.9036	-6.1 ± 1.1	141.3 ± 1.7
6898.7900	30.4 ± 1.0	-74.3 ± 1.5	6898.8247	0.7 ± 1.0	136.0 ± 1.7
6898.7120	27.3 ± 1.1	-77.4 ± 1.6	6898.7468	3.5 ± 1.1	117.1 ± 1.7
6898.8726	5.8 ± 1.0	-21.4 ± 1.4	6898.9075	-3.1 ± 1.2	93.7 ± 1.8
6898.7938	10.0 ± 1.1	-17.2 ± 1.5	6898.8285	-3.6 ± 1.1	88.5 ± 1.6
6898.7159	2.7 ± 1.3	-20.4 ± 1.7	6898.8324	-28.5 ± 2.3	-29.4 ± 3.1
6898.8766	-3.9 ± 1.0	-31.3 ± 1.4	6898.7553	29.9 ± 1.1	-1.7 ± 1.5
6898.7978	22.4 ± 1.0	62.3 ± 1.4	6898.8362	35.6 ± 1.1	-35.4 ± 1.7

Table 4.1: XSHOOTER data from the first night of observations. There are three main columns date, radial velocity of the absorption feature, and radial velocity of the emission feature. This is then duplicated in the neighbouring three columns.

HJD	$V_r(\text{abs})$	$V_r(\text{em})$	HJD	$V_r(\text{abs})$	$V_r(\text{em})$
-2450000	[km s ⁻¹]	[km s ⁻¹]	-2450000	[km s ⁻¹]	[km s ⁻¹]
6899.7069	-19.9 ± 2.5	-20.2 ± 1.7	6899.7415	33.7 ± 1.0	-80.3 ± 7.2
6899.7874	-8.7 ± 2.1	-18.1 ± 1.0	6899.8221	31.4 ± 1.1	-61.5 ± 32.2
6899.7107	36.5 ± 1.1	-46.5 ± 1.2	6899.7454	24.4 ± 1.6	-9.6 ± 2.6
6899.7912	33.6 ± 1.0	-64.9 ± 1.1	6899.8259	15.8 ± 1.7	-11.4 ± 2.0
6899.7146	37.8 ± 1.0	-99.4 ± 1.1	6899.3532	16.9 ± 1.2	48.0 ± 1.5
6899.7951	36.7 ± 1.0	-107.3 ± 1.0	6899.7527	9.4' ± 1.6	46.5 ± 2.6
6899.7184	41.8 ± 1.0	-146.8 ± 1.0	6899.7566	-2.0 ± 1.0	138.7 ± 4.2
6899.7223	44.8 ± 1.0	-171.1 ± 1.2	6899.7604	-6.7 ± 1.0	164.8 ± 2.5
6899.7261	48.2 ± 1.0	-185.0 ± 1.4	6899.7643	-10.0 ± 1.0	192.5 ± 1.6
6899.7300	49.1 ± 1.0	-173.3 ± 1.6	6899.7681	-8.5 ± 1.0	199.6 ± 1.4
6899.8105	46.2 ± 1.0	-178.9 ± 2.1	6899.7720	-8.4 ± 1.0	187.2 ± 1.1
6899.7338	45.4 ± 1.0	-163.3 ± 2.5	6899.7758	-5.3 ± 1.0	156.2 ± 1.0
6899.8143	40.9 ± 1.0	-152.3 ± 3.2	6899.7797	2.3 ± 1.0	112.4 ± 1.0
6899.7377	38.6 ± 1.0	-115.5 ± 4.1	6899.7029	1.6 ± 1.3	73.6 ± 1.4
6899.8182	36.5 ± 1.0	-133.4 ± 5.6	6899.7835	18.3 ± 1.6	51.4 ± 0.8

Table 4.2: XSHOOTER data from the second night of observations. The columns are identical to Table 5.1

4.6.1 Spectral features

As well as the Balmer lines I identified several other spectral lines: He I, Na I, Mg I, Si I, K I, Ca I & II, Ti I, and Fe I & II. The results of the fitting and the equivalent width analysis are listed in Tables 4.3 – 4.5. The results for each emission line outside of the Balmer series are very similar so, for simplicity, I will use only Ca II (866.214 nm) for comparison to H α going forward.

Figure 4.2 shows the trailed spectra of H α demonstrating the binary nature of the system with emission coming from the brown dwarf and absorption coming from the white dwarf. Of course, emission will be occurring within the white dwarf atmosphere however due to the higher optical depth, and thus lower mean free path of emitted photons, within the white dwarf atmosphere,

	Wavelength λ (Å)	Semi-amplitude K (kms ⁻¹)	Systemic velocity γ (kms ⁻¹)	Day-side EW (Å)	Night-side EW (Å)
H α	6562.76 (ab)	28.3 ± 0.4	18.4 ± 0.3	-	-
	6562.76 (em)	-192.4 ± 1.2	4.5 ± 0.9	-0.79 ± 0.021	-0.03 ± 0.021
H β	4861.30 (ab)	28.9 ± 0.9	6.8 ± 0.3	-	-
	4861.30 (em)	-189.5 ± 5.2	2.1 ± 3.7	-0.29 ± 0.030	-0.09 ± 0.030
H I	10938.17	-184.8 ± 8.7	-14.8 ± 6.2	-	-
He I	21655.34	-119.3 ± 50.3	1.7 ± 24.2	-0.66 ± 0.1	0.24 ± 0.1
Na I	5889.95	-188.2 ± 2.4	2.9 ± 1.7	-0.20 ± 0.021	-0.02 ± 0.021
	5895.92	-185.7 ± 2.5	6.6 ± 1.8	-0.16 ± 0.021	0.04 ± 0.021
	8183.27	-191.2 ± 7.0	1.0 ± 4.8	-0.13 ± 0.021	0.03 ± 0.021
	8194.81	-184.8 ± 6.1	-4.4 ± 4.2	-0.19 ± 0.021	0.06 ± 0.021
Mg I	5167.32	-188.1 ± 2.4	-3.5 ± 1.7	-0.15 ± 0.030	-0.05 ± 0.030
	5172.68	-186.7 ± 2.3	-3.8 ± 1.6	-0.17 ± 0.030	-0.09 ± 0.030
	5183.60	-187.9 ± 1.7	-6.4 ± 1.2	-0.14 ± 0.030	-0.07 ± 0.030
	8806.76	-191.4 ± 5.0	-23.0 ± 3.5	-0.40 ± 0.021	-0.03 ± 0.021

Table 4.3: The best fit radial velocity parameters (cf. equation 5.1) to the emission lines. The period and zero ephemeris were determined by fitting the white dwarf radial velocity data and can be found in Table 4.6. P and T_0 and were then held constant for all subsequent emission lines. The equivalent widths of the emission lines were determined, where possible, from the line profiles.

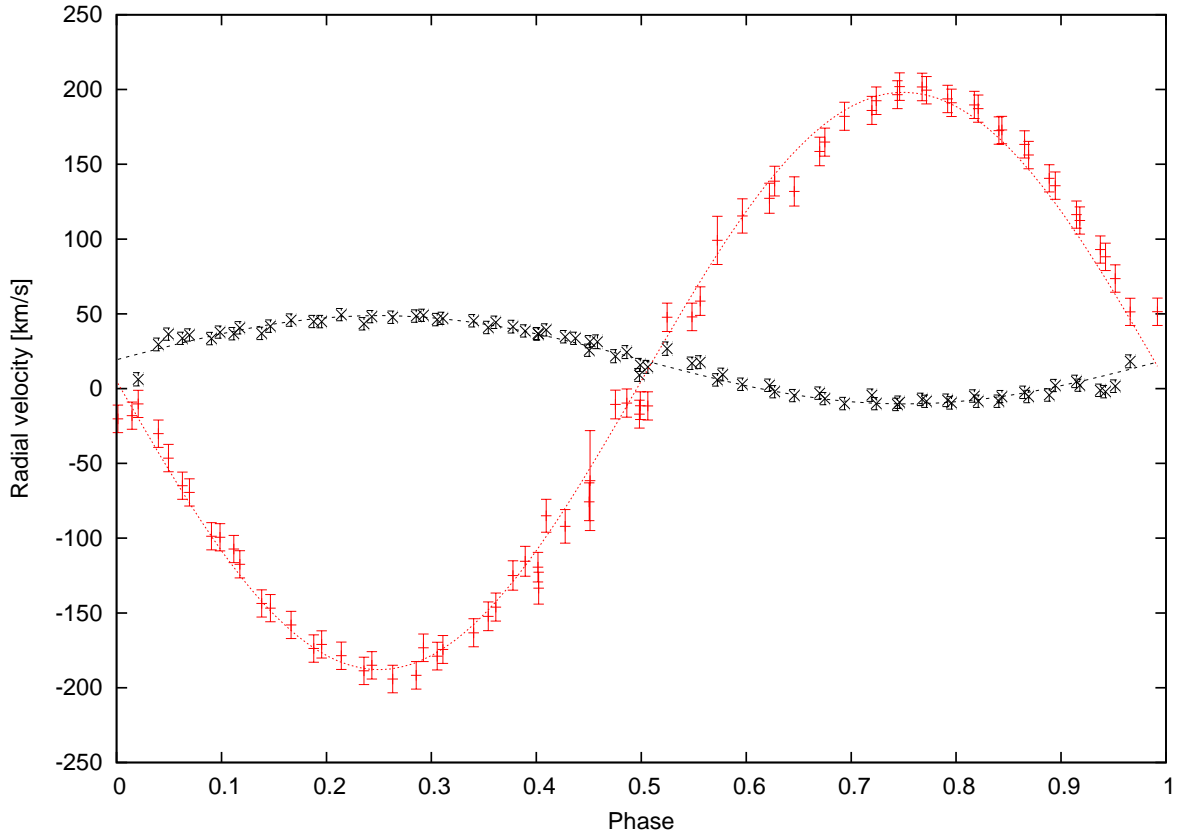


Figure 4.1: The measured radial velocity values of the $H\alpha$ emission (red '+') and absorption (black 'x'). These have been fit with equation (5.1) using the best fitting values for γ and K from tables 4.3 – 4.5.

observationally, we see the absorption. The brown dwarf atmosphere is not so dense and has a lower optical depth for the upper layers of its atmosphere thus we can detect the emission. The adjacent trailed spectra of the Ca II emission line highlights the similarity between the $H\alpha$ and Ca II emission features. These emission features disappear briefly when the "night"-side of the brown dwarf is facing the observer ($\phi = 0.5$). For consistency I follow previous studies of WD0137-349 in adopting the unconventional phasing of this system and define phase 0 as when the brown dwarf is furthest from the observer. Therefore it is likely the emission is only coming from the heated side of the brown dwarf. This is happening in both trails however it is slightly less obvious in the $H\alpha$ trail due to the absorption feature. This is further validated by the equivalent widths of all of the metal lines listed in Tables 4.3 – 4.5: the night-side equivalent widths are all ≈ 0 .

	Wavelength λ (Å)	Semi-amplitude K (kms ⁻¹)	Systemic velocity γ (kms ⁻¹)	Day-side EW (Å)	Night-side EW (Å)
	10585.14	-171.8 ± 12.7	10.9 ± 9.0	-0.32 ± 0.1	0.04 ± 0.1
Si I	10868.79	-182.5 ± 5.0	0.5 ± 3.7	-0.09 ± 0.1	0.23 ± 0.1
	12031.51	-187.1 ± 4.8	-13.2 ± 3.7	-0.29 ± 0.1	0.03 ± 0.1
K I	7698.96	-187.5 ± 2.0	7.1 ± 1.4	-0.14 ± 0.021	0.00 ± 0.021
Ca I	12816.04	-184.8 ± 6.3	19.8 ± 4.2	-	-
	3933.66	-185.0 ± 4.2	-1.2 ± 2.9	-0.08 ± 0.030	0.05 ± 0.030
Ca II	8498.02	-186.5 ± 0.8	6.3 ± 0.6	-0.46 ± 0.021	-0.01 ± 0.021
	8542.09	-185.6 ± 1.1	7.1 ± 0.8	-0.75 ± 0.021	0.00 ± 0.021
	8662.14	-186.9 ± 1.0	5.1 ± 0.7	-0.73 ± 0.021	-0.05 ± 0.021
	11752.31	-177.6 ± 4.4	13.1 ± 3.0	-0.05 ± 0.1	-0.06 ± 0.1
Ti I	11982.96	-191.0 ± 3.5	8.2 ± 2.7	-0.14 ± 0.1	-0.05 ± 0.1
	19860.98	-158.7 ± 8.5	-6.2 ± 4.6	-0.44 ± 0.1	0.05 ± 0.1

Table 4.4: A continuation of Table 4.3. The best fit radial velocity parameters to the K I, Ca I & II, and Ti I emission lines.

In addition to my search for emission features, I looked for other absorption lines which may be present in the system either from the brown dwarf – the likes of which have been seen in subdwarf (sdB) systems (Wood & Saffer, 1999) – or intrinsic to the white dwarf, indicating it may be a DAZ - a white dwarf with metal lines in its atmosphere. The white dwarf in this system is within the temperature range of 16 000 – 20 000 K which was suggested by Kilic et al. (2006) to be cool enough to potentially show metal absorption lines in its spectrum, however WD0137-349 does not. Only the Balmer lines are present coming from the white dwarf. There is also no emission in phase with the white dwarf therefore no mass transfer or gas circulation can be inferred.

	Wavelength	Semi-amplitude	Systemic velocity	Day-side EW	Night-side EW
	λ (Å)	K (kms ⁻¹)	γ (kms ⁻¹)	(Å)	(Å)
	8327.05	-186.3 ± 2.2	3.6 ± 1.6	-0.11 ± 0.021	0.003 ± 0.021
	8334.53	-185.7 ± 4.6	19.7 ± 3.2	-0.10 ± 0.021	0.04 ± 0.021
Fe I	8387.77	-185.2 ± 2.2	7.7 ± 1.6	-0.16 ± 0.021	-0.01 ± 0.021
	8688.62	-188.9 ± 1.4	7.2 ± 1.0	-0.15 ± 0.021	0.01 ± 0.021
	8824.22	-186.4 ± 2.5	6.6 ± 1.7	-0.05 ± 0.021	-0.01 ± 0.021
	10682.39	-193.9 ± 16.8	40.3 ± 12.1	-0.10 ± 0.1	-0.05 ± 0.1
	11970.50	-186.5 ± 11.6	2.1 ± 7.4	-0.04 ± 0.1	-0.10 ± 0.1
	13120.47	-160.6 ± 27.5	-31.3 ± 17.1	-0.07 ± 0.1	-0.18 ± 0.1
	13147.92	-210.1 ± 10.6	5.0 ± 6.5	-0.07 ± 0.1	0.07 ± 0.1
	14876.54	-219.6 ± 25.4	14.0 ± 15.5	-0.77 ± 0.1	-0.1 ± 0.1
	15022.67	-185.0 ± 5.3	6.7 ± 3.7	-0.13 ± 0.1	0.02 ± 0.1
	15036.47	-168.7 ± 18.0	3.9 ± 12.4	-0.14 ± 0.1	-0.24 ± 0.1
	19771.29	-180.5 ± 15.5	9.0 ± 7.9	-	-
Fe II	8434.49	-198.2 ± 3.9	17.8 ± 2.8	-0.15 ± 0.021	-0.07 ± 0.021
	10690.51	-180.8 ± 4.7	-0.8 ± 3.5	-0.15 ± 0.1	0.02 ± 0.1
	11825.65	-182.2 ± 10.8	18.0 ± 7.2	-0.03 ± 0.1	0.05 ± 0.1
	15885.67	-171.0 ± 15.4	2.1 ± 10.1	-	-
	17106.54	-175.0 ± 12.7	10.6 ± 7.8	-0.17 ± 0.1	-0.20 ± 0.1

Table 4.5: A continuation of Tables 4.3 and 4.4. The best fit radial velocity parameters to the Fe I & II emission lines.

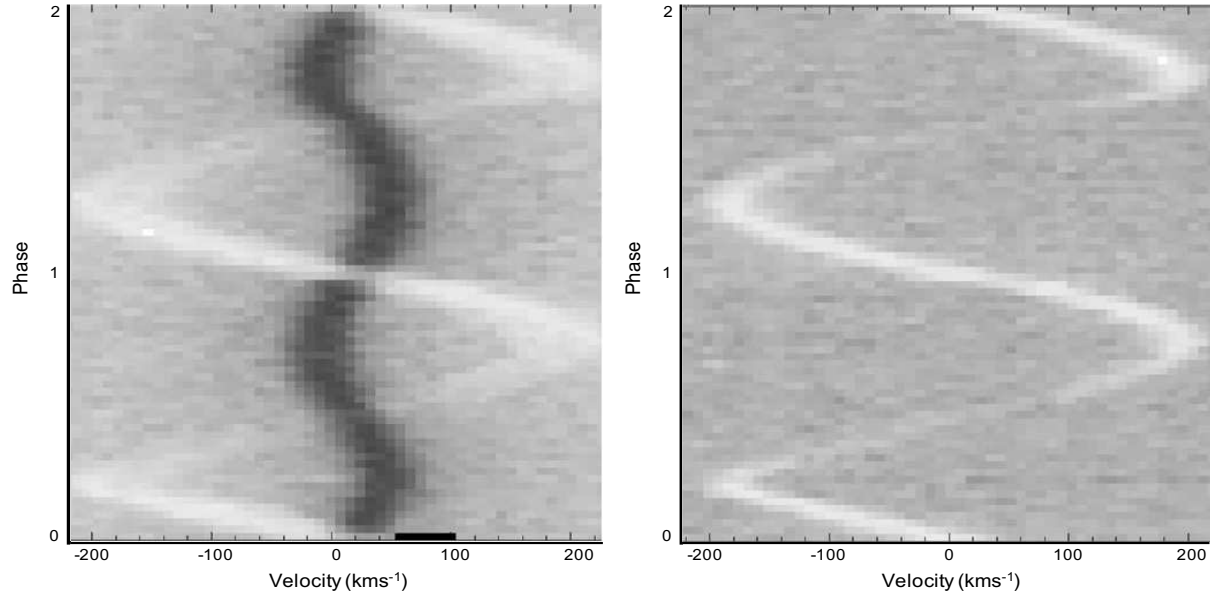


Figure 4.2: Trailed spectra demonstrating the binary nature of the system. **Left:** The $H\alpha$ emission (white) and absorption (black) line demonstrating the emission line is in anti-phase with the absorption feature. **Right:** The 8662.14 \AA Ca II emission line (white). The Ca II emission closely resembles the $H\alpha$ emission indicating they originate from the same place: the brown dwarf.

4.7 Comparison to similar systems

WD0137-349B is unique because it is the first irradiated brown dwarf to exhibit He, Na, Mg, Si, K, Ca, Ti, and Fe emission lines in its atmosphere. The radial velocities of these lines confirm that they originate from the brown dwarf and are most likely a direct result of irradiation from the 16 500 K white dwarf host causing a temperature inversion in the brown dwarf atmosphere. Below I contrast the observable properties of WD0137-349B to other, similarly irradiated brown dwarf and low-mass stellar companions to white dwarfs in short period binaries.

4.7.1 Low mass companions

A large number of Post Common Envelope Binaries (PCEBs) have low mass stellar companions and Balmer line emission has been detected in a number these. For example, LTT 560 displays

H α emission with dual components, one of which is due to stellar activity on the M dwarf (Tappert et al., 2007). Ca I & II, Na I, K I, Fe I and Ti were observed in the secondary’s atmosphere as absorption (Tappert et al., 2011). Irradiation induced emission lines outside of the Balmer series are less common but have been seen. For example Ca II and Na I emission in GD 448 (Maxted et al., 1998) and He I and Mg II emission in NN Serpentis (Parsons et al., 2010).

A handful of PCEBs have substellar companions but emission from these is seen less frequently. H α emission was detected in WD0137-349 by Maxted et al. (2006); it has also been seen in other systems such as SDSS J120515.80-024222.6 (71.2 mins; Parsons et al. 2017) SDSS J155720.77+091624.6 (2.27 hours; Farihi et al. 2017), and EPIC212235321 (68.2mins; Casewell et al. 2018).

Whilst WD0137-349B is the first brown dwarf companion discovered to exhibit irradiation induced metal emission lines, irradiation has been observed to induce temperature differences across the surfaces of brown dwarf companions. For example SDSS J141126.20 +200911.1 displays a flux excess in the K_s band indicative of a temperature increase on the irradiated side of the brown dwarf (Littlefair et al., 2014) and the cataclysmic variable SDSS J143317.78 +101123.3 shows a ~ 200 K temperature difference across the surface of the brown dwarf (Hernández Santisteban et al., 2016). WD0137-349 has a temperature difference of 500 K between the day– and night–side of the brown dwarf (Casewell et al., 2015).

These irradiated white dwarf – brown dwarf systems do not all manifest the same observable properties. In order to understand this we need to look at the atmospheres of isolated brown dwarfs to establish a base from which we can interpret irradiated brown dwarfs.

4.7.2 Emission from non-irradiated brown dwarfs

H α emission as been seen in the atmospheres of ”hyperactive” brown dwarfs. Pineda et al. (2016) characterised the H α emission in three such objects: 2MASS J00361617+1821104 (2MASS 0036), 2MASS J17502484-0016151 (2MASS 1750), and SDSS J042348.57-041403.5

(SDSS 0423). 2MASS 0036 is an L dwarf with variable $H\alpha$ which is thought to be linked to magnetic interaction with a companion. The $H\alpha$ emission isn't as strong in 2MASS 1750 which has been classified as a L5.5 brown dwarf and SDSS 0423 is an L6+T2 brown dwarf binary with the $H\alpha$ emission coming from the L dwarf. The detection of $H\alpha$ emission is linked to chromospheric activity in brown dwarf atmospheres. The M9.5 dwarf PC 0025+0447 ($M < 0.06M_{\odot}$) discovered by Schneider et al. (1991) displays consistent $H\alpha$ emission. This emission and the emission of He I and O I is thought to be due to coronal activity on the brown dwarf (Martín et al., 1999). 2MASS J04183483+2131275 a $L5 \pm 0.5$ brown dwarf is the first, in the Hyades open star cluster, to display chromospheric $H\alpha$ emission (Perez-garrido 2017). This activity is unusual and is not expected from a brown dwarf of this age. A double degenerate binary system, 2MASS J13153094-2649513 (L5 + T7; Burgasser et al. 2011), shows $H\alpha$, Na I, and K I emission coming from the L dwarf (Fuhrmeister et al., 2005). The lack of irradiation suggests the emission is non-thermal, the cause is thought to be the presence of a chromosphere driven by an unusually strong magnetic field Burgasser et al. (2011).

WD0137-349B displays metal emission lines akin to irradiated low-mass stellar companions but is the first sub-stellar companion to do so. So-called hyperactive brown dwarfs have shown similar emission which has been taken as evidence for the presence of a chromosphere. The difference being hyperactive brown dwarf chromospheres are thought to be generated by unusually strong magnetic fields; whereas WD0137-349B is due to the intense irradiation from the white dwarf. We will discuss the presence of brown dwarf chromospheres with respect to WD0137-349B in the next section.

4.8 Discussion

There are some distinct atmospheric differences between WD0137-349 and field brown dwarfs. For example, molecules such as CrH and FeH are expected to be present in a L type dwarf (see Kirkpatrick et al. 1999) but neither of these molecules are detectable in the data. Nor is there any sign of Cr, Rb, or Cs which are expected in a substellar atmosphere. These elements are thought

to be raised in the atmosphere through the process of convection (Oppenheimer et al., 1998), so their non-detection suggests that irradiation may be hindering the convective processes that would normally occur in a brown dwarf atmosphere.

The metal emission lines I have detected allow me to draw some parallels, for example, Na I and K I are expected to be in the atmosphere of a late L-type brown dwarf (Kirkpatrick et al. 1999; Helling & Casewell 2014). A brown dwarf of spectral type L7 or later would not be expected to display TiO in its spectrum due to its cooler atmosphere (<2700 K) leading to the formation of perovskites (CaTiO_3) that remove the TiO from the atmosphere (Kirkpatrick et al., 1999). Indeed, in these data, I do not detect any molecules at all; I have however detected Ti I suggesting that irradiation may have destroyed TiO and/or the dust grains thus leaving Ti in the upper-atmosphere.

Atmospheres of single or binary brown dwarfs are understood to have very low effective temperatures. The gas-phase is therefore dominated mostly by H_2 , as well as H_2O , CO or CH_4 , depending on the effective temperature. If the brown dwarf is irradiated by an external source, the atmospheric temperature will rise similar to the outer atmospheres of irradiated planets (see Fig 1 in Barman et al. (2004)). Schmidt et al. (2015) present observations from the BOSS survey that suggest that brown dwarfs have chromospheres and this is corroborated by Sorahana et al. (2014) who reach a similar conclusion. Schmidt et al. (2015) and Sorahana et al. (2014) both invoke a simplified representation of the chromosphere temperature structure.

Figure 4.3 is the output from a gas-phase equilibrium code (see Bilger et al. 2013) that was executed by Ch. Helling¹. For my work I have interpreted the plot produced from this code. This acts as a simple first test to model the expected chemical composition in a hot and diluted upper part of a brown dwarf atmosphere. The code uses a prescribed DRIFT-PHOENIX model ($T_{\text{gas, gas}}$)-structure for $T_{\text{eff}}=2000$ K, $\log(g)=5.0$, $[\text{M}/\text{H}]=\text{solar}$ as input for the inner atmospheric part. The temperature in the upper atmosphere was manipulated to be indicative of a temperature increase caused by a chromosphere or external energy input (black line, top panel, Fig. 4.3). Which allowed the gas phase temperature to be high enough to increase the local degree of thermal ionisation (blue line, top panel) substantially as is suggested by my XSHOOTER observations. Panels

¹School of Physics and Astronomy, University of St Andrews, St Andrews KY16 9SS, UK. ch80@st-and.ac.uk

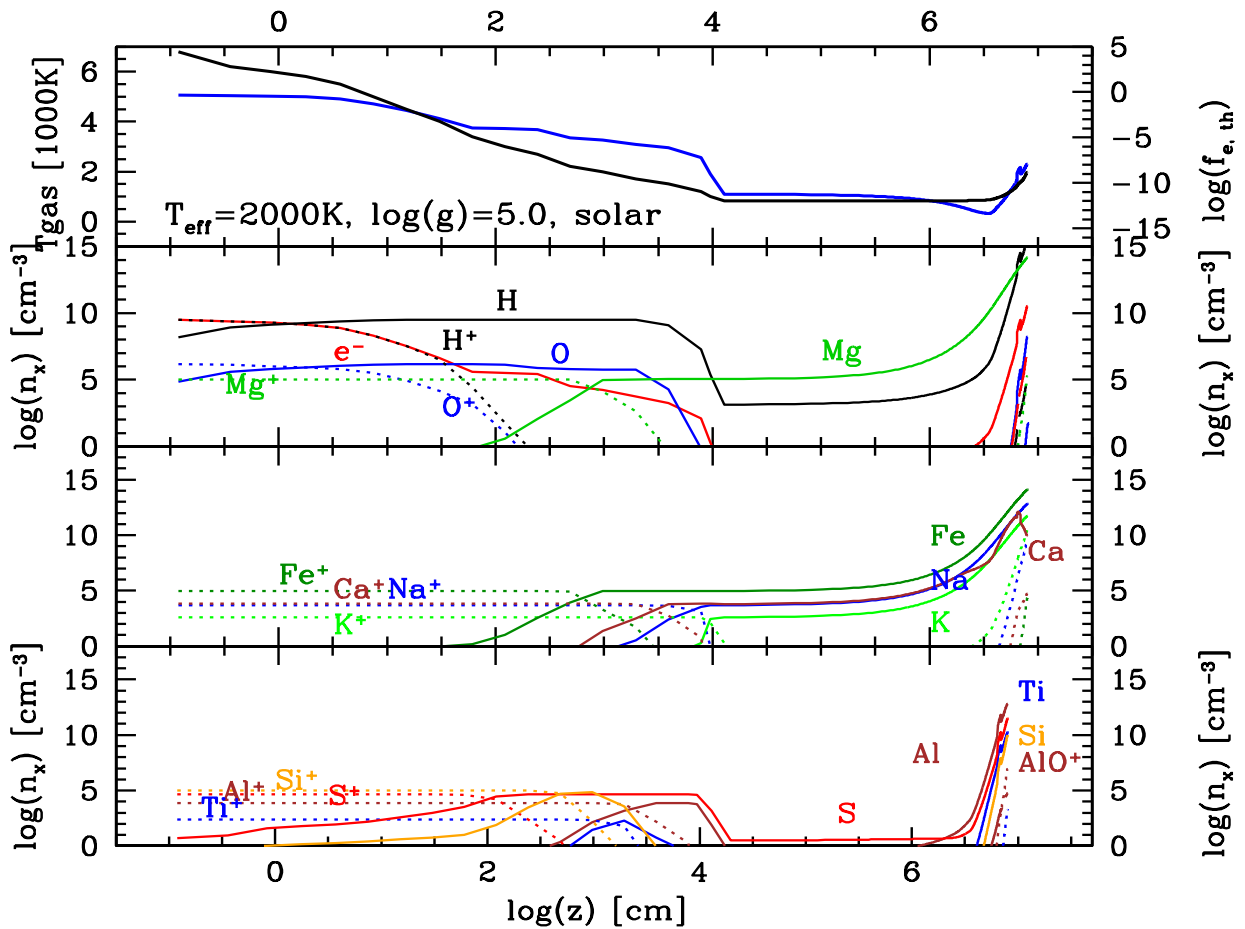


Figure 4.3: Chemical equilibrium results for a Drift-Phoenix model atmosphere ($T_{\text{eff}} = 2000 \text{ K}$, $\log(g) = 5.0$, solar metallicity) with an artificially added chromosphere-like temperature increase for atmospheric heights $z < 10^4 \text{ cm}$ (z decreases outwards). The top panel shows the temperature of the brown dwarf (black, steeper line) due to a chromosphere or external energy input and the degree of thermal ionisation (blue, flatter line) that these higher temperatures induce. The second, third, and fourth panels show the chemical equilibrium results plotted for a selected number of atoms (solid lines) and ions (dashed lines) each with a corresponding label. As expected, the inner part of the atmosphere is dominated by the atomic form of an element but an outward increasing temperature (e.g. resulting from a chromosphere or corona) will cause different ions to appear height-dependently.

2 – 4 in Figure 4.3 demonstrate which ions would emerge if WD0137-349B exhibited such a rise in local temperature in the upper atmosphere. Various ions dominate over their atomic counterpart at different gas temperatures i.e. at different atmospheric heights. For example, H^+ (H II) is the dominating H-binding species rather high in our example atmosphere where $T_{\text{gas}} \approx 6000 \text{ K}$ while Fe II (Fe^+) dominates over Fe I (Fe) at $T_{\text{gas}} \approx 2100 \text{ K}$ for the given density structure; the uppermost atmospheric layer is now fully ionised with $n(\text{H}^+) = n(\text{e}^-)$. While the calculation presented in Fig. 4.3 does only consider collisional ionisation in LTE, it gives an indication of how the upper atmosphere of a brown dwarf would change if irradiation, or another mechanism for forming a chromosphere, caused an outward temperature increase which is necessary to explain the emission features observed for WD0137-349B.

This simple approach suggests that atomic emission lines are expected to occur in brown dwarf atmospheres. Irradiated brown dwarfs will, however, have strong temperature gradients in the observable atmosphere similar to irradiated giant gas planets e.g. HD 189733b (Lee et al., 2016). Such 'surface' temperature gradients are caused by hydrodynamic transport of atmospheric gas and will cause the local chemistry to change substantially (Helling et al., 2016). Therefore, a far hotter day-side of an irradiated brown dwarf would show higher ionised elements in emission than the terminator regions, for example. The data supports this as the strength of the emission lines significantly weaken when the night-side of the brown dwarf is in view. This will be discussed further in the next section.

4.8.1 Characterising the line profiles

The equivalent widths listed in Tables 4.3 – 4.5 demonstrate that there is a clear and dramatic difference between the day- and night-side of the brown dwarf which fits with the 500 K temperature difference found by Casewell et al. (2015). Figure 4.4 shows the variability in equivalent width of the $\text{H}\alpha$ emission line with respect to the phase of the system. Equivalent width is effectively a measure of line strength and there is a clear weakening of the line at $\phi = 0.5$: where the dark side of the brown dwarf is facing the observer. The same has been performed for the 8662 \AA Ca II line and is also plotted in Figure 4.4; the shape of this variation for these two lines matches closely

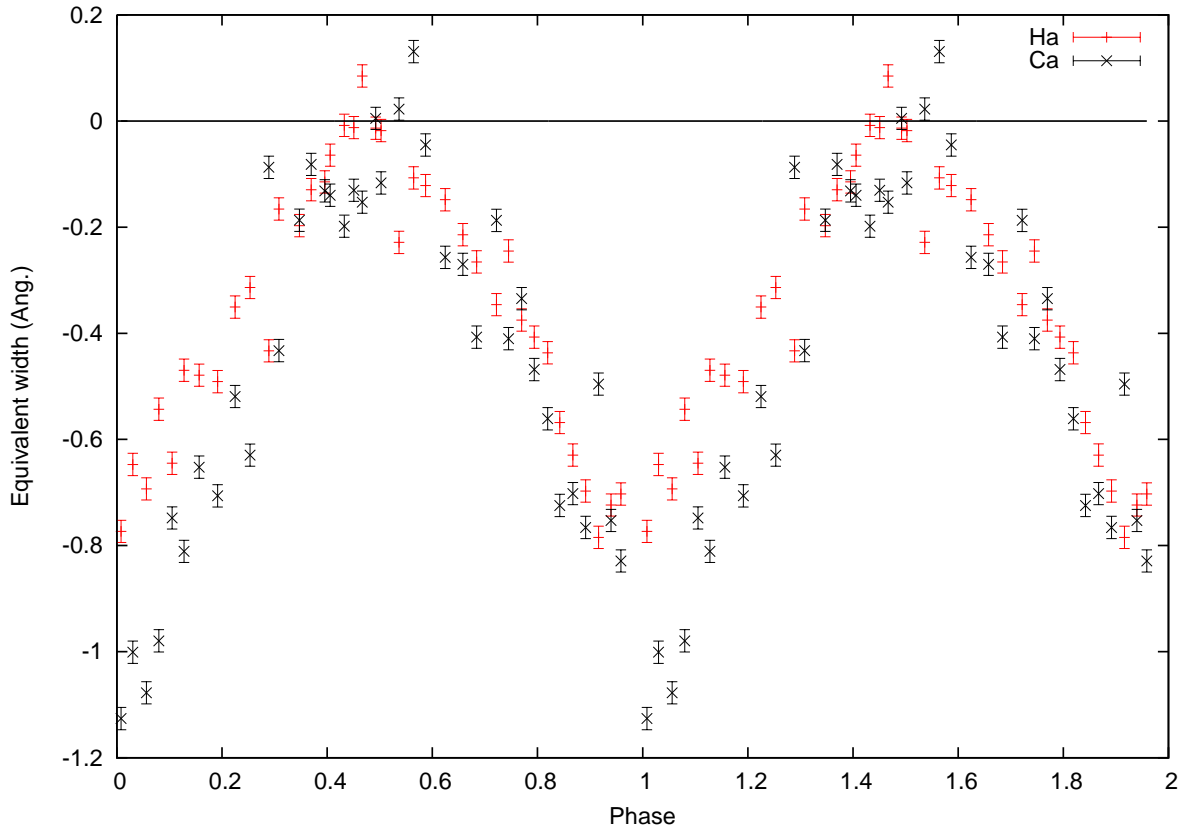


Figure 4.4: Equivalent width of the $H\alpha$ emission (red '+') and the Ca II 8662 Å line (black 'x') as a function of phase. The horizontal black line at an equivalent width of 0 Å marks the point where a spectral feature is no longer present. The strength of the emission lines varies with orbital phase, going to zero at $\phi=0.5$ i.e. when the dark-side of the brown dwarf is in view. The data has been duplicated over two phases.

and the Ca II line appears only marginally weaker. It is likely that the phase dependent variability of the brown dwarf indicates significantly different atmospheric properties between the day- and night-side. This may give rise to extreme variations in weather (Lee et al., 2015). From Burleigh et al. (2006) we see that the brown dwarf dominates the continuum at wavelengths longwards of $1.95 \mu\text{m}$ therefore lines detected in the NIR are more largely affected and caution should be exercised when interpreting these equivalent widths.

I have compared the measured equivalent widths to published equivalent widths of two "hyper-active" brown dwarf systems (2MASS J0418 and SDSS J0423) that display $H\alpha$ emission. There are other brown dwarfs with published equivalent widths for this line however they are most of-

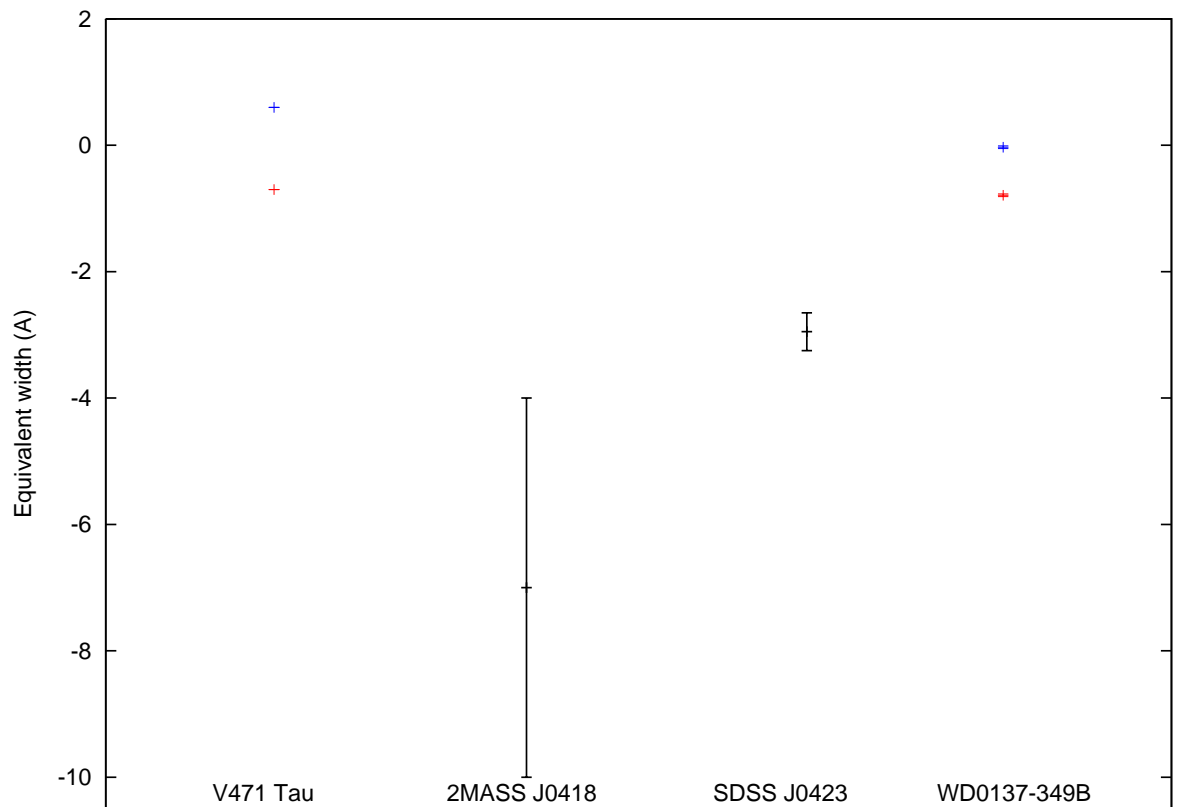


Figure 4.5: A comparison of our measured equivalent widths to three other brown dwarfs that display this type of emission and whose equivalent width had been measured. V471 Tau has also been included as it has day (red, lower) and night (blue, higher) side equivalent widths with a clear phase dependency similar to WD0137-349B.

ten early L dwarfs on or around the hydrogen burning mass limit or the $H\alpha$ emission is sporadic and probably due to flaring. The two included in Figure 4.5 have sustained $H\alpha$ emission. I also compare to V471 Tau as it is an example of an irradiated sub-stellar companion. Comparisons to the hyperactive brown dwarfs is valid as the underlying continuum is unaffected by non – brown dwarf components such as reflection from a companion. Setting the continuum level in V471 Tau was more complex due to line blending and rotational broadening but Bois et al. (1991) accounted for this. Thus I can compare the $H\alpha$ values to these literature values. Clearly, data is sparse thus any conclusions drawn are preliminary and more observations are required to build a better picture of irradiated atmospheres. That said, Figure 4.5 suggests that the emission from WD0137-349B is more akin to irradiation induced emission like that seen on V471 Tau than emission seen in

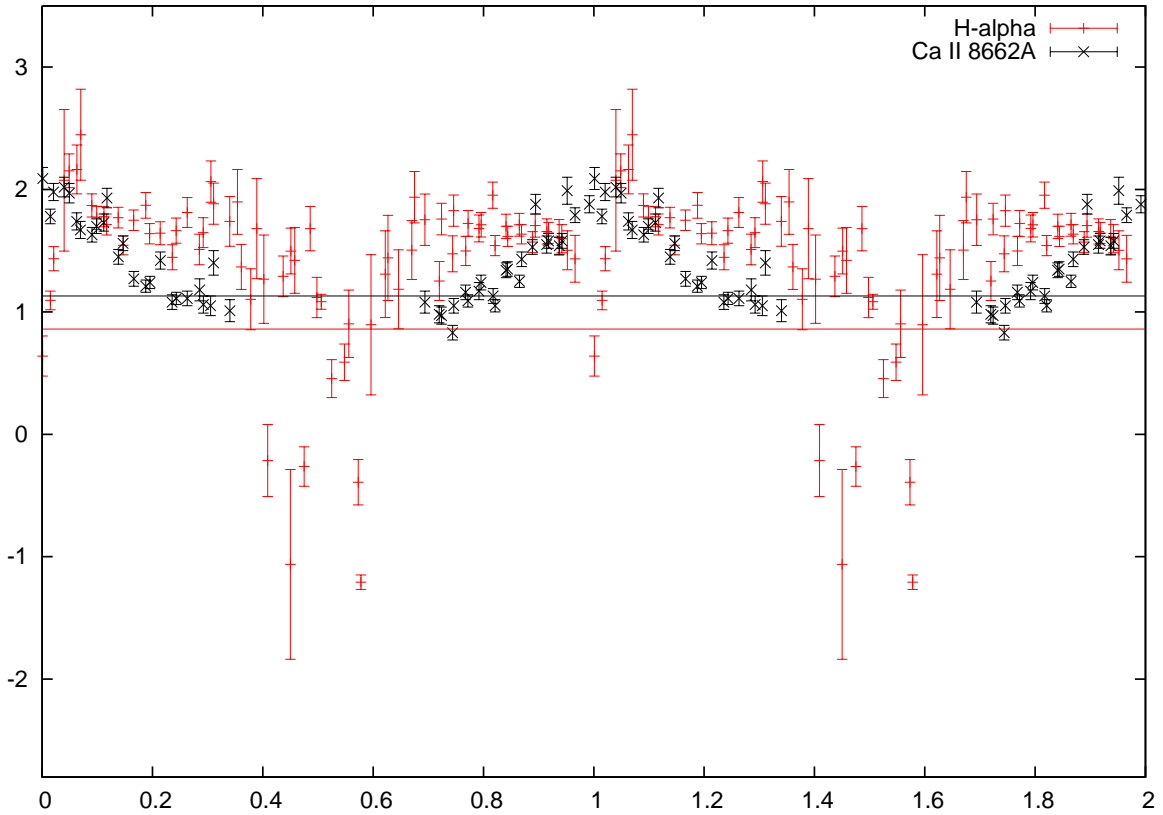


Figure 4.6: The FWHM of the $H\alpha$ line (red '+') and the Ca II line (black 'x') with respect to phase. The horizontal lines indicate the FWHM calculated from the $v\sin(i)$ for each line in the corresponding colour. The strength of the Ca II line between $\phi = 0.35 - 0.7$ was too weak to get a reliable FWHM measurement. This has been duplicated over two orbits for clarity.

”hyper-active” brown dwarfs which is driven by unusually strong magnetic fields.

I also observe a phase dependent change in the width of the emission lines as is demonstrated in Figure 4.6. From this I can see that the Ca II emission line is narrower at nearly every point in phase this is likely due to the region of Ca II emission being more concentrated on the brown dwarf surface i.e. towards the front of the white dwarf-facing hemisphere. The signal-to-noise ratio of the Ca II line between $\phi = 0.35 - 0.7$ was too low to fit.

The emission region of the brown dwarf is situated on its upper atmosphere so so a measurement of the radial velocity of the emission line is not the true representation of the radial velocity of the brown dwarf as a whole. The semi-amplitude component, K_{em} , of the emission radial velocity

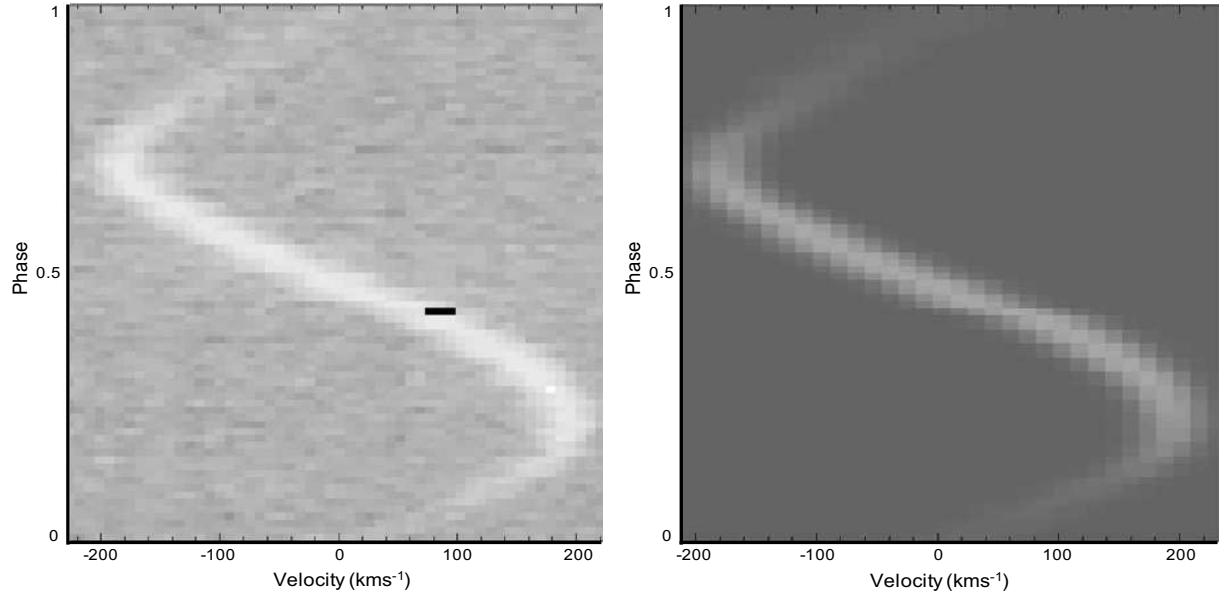


Figure 4.7: **Left:** A trail plot observed spectra centred on the Ca II 8662 Å emission line with orbital phase going from 0 to 1 vertically and radial velocity on the x-axis. **Right:** Simulated data trail plots of the Ca II 8662 Å emission line. The black bar on the left plot is due to bad pixels that were masked out of that spectrum, they do not affect the data in any way.

needs to be offset to reflect the centre of mass of the brown dwarf. To investigate this I simulated the Ca II emission lines using code written by Pierre Maxted². His code creates a model that takes into account the Roche geometry of the brown dwarf and limb darkening / brightening. I simulated an intrinsic spectrum at each point on the brown dwarf that is equal to Gaussians with the same FWHM as the resolution of the spectra. The emission flux is proportional to the incident flux from the white dwarf and no intrinsic emission or absorption from the brown dwarf is assumed i.e. pure emission due to irradiation. The exposure time of 5 mins is an appreciable fraction of the orbital period, to account for this I have included phase smearing by numerical integration over three phase points.

I set up a grid of semi-amplitude, K , filling factor, f , and linear limb darkening, X , as defined in Maxted et al. (1998), where the filling factor is the ratio of the star radius to the size of the Roche lobe measured from the centre of the star towards the L1 point. The code uses Levenburg-Marquadt minimisation to optimise γ and the ratio of the Ca II intrinsic line strengths plus an

²Keele University, Keele, Staffordshire, ST5 5BG, United Kingdom.

Properties of the system	
P (days)	0.079429939(1)
T_0	2454178.6761 ± 0.0003
K_c (km s ⁻¹)	210 ± 5
Mass ratio	0.135 ± 0.004

Table 4.6: The values obtained from fitting Equation (5.1) to the measured radial velocities of the H α absorption and emission lines. The error on the final digit of the period is shown in parentheses. We list the corrected semi-amplitude for the brown dwarf used to correct for the light from the emission being offset from the centre of mass of the brown dwarf; we used this value to calculate the masses of the white dwarf and brown dwarf.

overall scaling factor to match the line strengths of the observations. I provided all the spectra so that the code knows at which orbital phases to calculate the output spectra and the wavelength scale and range, i.e., so that it is easy to do a direct pixel-by-pixel comparison. From Figure 4.7 shows these simulations provide a good fit to the data, the best fitting values are listed in Table 4.6 along with the calculated mass ratio. I also estimate the $v \sin(i)$ of this system to be 39.3 km s^{-1} which can be translated to FWHM using, $\text{FWHM} = \frac{v \sin(i)}{c} \lambda$ where λ is the wavelength of the line. This has been indicated with horizontal lines on Figure 4.6 for H α and Ca II.

Ability to reproduce this line strength variation that is seen in WD0137-349 will be important in any future models of irradiated atmospheres.

4.8.2 Heat redistribution of irradiated sub-stellar objects

In an attempt to explore the role irradiation and opacity plays on heat redistribution Perna et al. (2012) model the atmosphere of hot Jupiters using 3D atmospheric circulation models. The models are cloud-free and this results in an atmosphere opacity that is too low. They do find however, that heat redistribution breaks down at irradiation temperatures greater than 2200 - 2400 K and attribute this to the advective timescale becoming much longer than the radiative timescale.

Showman et al. (2013) use a circulation model to compare the atmospheres of hot Jupiters with and without intense irradiation. They found that strong insolation (stellar radiation that reaches the planets surface) produces circulation dominated by high-altitude air flow from the day-side to the night-side and suggest a return flow at deeper levels. It is clear irradiation of gas giant planets introduces additional dynamical effects within their atmospheres. Younger, lower gravity ($\log g \approx 5$) brown dwarfs share many properties with these gas giant exoplanets (Faherty et al., 2013).

No 3D simulations have been created for higher gravity irradiated brown dwarfs like WD0137-349B but comparable atmospheric effects could be expected. A recent study by Hernández Santisteban et al. (2016) looks at the interacting binary system of a brown dwarf being irradiated by a 13 200 K white dwarf. They model the atmosphere using a simple geometric reprocessing model and find poor heat redistribution from the day- to the night-side. With a slightly hotter white dwarf such as WD0137-349 ($T_{\text{eff}} = 16\,500$ K) one would expect this effect to be similar and the strength variation over the orbit of all our observed emission lines does support this. Although the longer period of WD0137-349B is likely to make heat redistribution more effective. Full analysis of phase curves would need to be done to be sure of this effect.

4.9 Conclusion

The work presented in this chapter demonstrates the first brown dwarf atmosphere to exhibit a range of emission lines as a direct result of intense UV irradiation from the 16 500 K white dwarf primary.

I have used 78 XSHOOTER observations of WD0137-349AB to refine the ephemeris of the system using the emission and absorption lines of $H\alpha$. I show that this system is detached as there is no indication of mass transfer in the trailed spectra and no lines other than balmer lines coming from the white dwarf. I have detected new emission lines of He I, Na I, Mg I, Si I, K I, Ca I & II, Ti I, and Fe I & II originating from the brown dwarf atmosphere as a direct result of irradiation-induced temperature inversion of the brown dwarf atmosphere. Observations of such metal lines

is what makes WD0137-349 unique.

One would expect that shorter orbits with hotter white dwarfs, thus more intense irradiation, would lead to stronger Balmer line emission and metal emission like we see in the atmosphere of WD0137-349B. From the discussed comparable systems I find that despite their similarities irradiated substellar objects do not all manifest the same observable properties however the sample size is very small. Ideally one would have many white dwarf - brown dwarf binary systems across a range of brown dwarf spectral types, orbital separations, and white dwarf temperatures; this way we could better quantify the relationship between irradiation and metal emission in substellar atmospheres.

I analysed the result of a simple preliminary test from Ch. Helling's DRIFT-PHOENIX model that manipulated the temperature of the upper atmosphere to give an outward temperature increase. This allowed me to establish what to expect from an irradiated brown dwarf atmosphere specifically the expected chemical composition at different gas temperatures and atmospheric heights. The elements detected and their ionisation states broadly match the predictions of this model which supports the possibility of a brown dwarf chromosphere being present.

I measured the equivalent widths of all emission lines in WD0137-349B and found the line strengths to weaken from the day to the night-side of the brown dwarf. This indicates that the irradiation is likely driving dramatic temperature and weather variations between the two sides of this tidally locked brown dwarf. By comparing the $H\alpha$ day- and night-side equivalent width to that of similar systems I found that WD0137-349B appears more akin to the irradiation induced $H\alpha$ emission of low mass stellar companion atmospheres than isolated brown dwarfs.

Any future models of irradiated atmospheres will need to reproduce the line strength variation that is seen here.

5

Possible accretion in NLTT5306

NLTT5306 is much cooler than the previous system and therefore the influence of irradiation (if there is any at all) will be reduced. I will investigate the possibility of using NLTT5306 in a similar way to WD0137-349 as well explore other ways in which this system may be informative.

5.1 Introduction

The contents of this chapter are published in Longstaff et al. (2018; submitted) on NLTT5306 a $0.4 M_{\odot}$ DA white dwarf with a $0.053 M_{\odot}$ brown dwarf companion. I present new XSHOOTER spectra of NLTT5306. This system is extremely likely to have undergone common envelope

evolution, resulting in a short period (101 min) binary. I have confirmed the presence of $H\alpha$ emission and discovered a Na I absorption feature associated with the white dwarf. The sinking timescale of a DA white dwarf atmosphere is very short, therefore if metal spectral lines are detected matter must be accreting continuously onto the surface of the white dwarf. I followed this up with *Swift* observations which reveal an UV excess but no orbital period modulation. I compare NLTT5306 to similar systems including WD0137-349 (see Chapter 4), a system with component masses and orbital period almost identical to NLTT5306, but exhibiting no evidence of accretion. The only major differences between NLTT5306 and WD0137-349 are the cooling age and temperature of the white dwarfs. Given these similarities it may be expected that mass transfer would be more likely to occur in the system with the hottest white dwarf, where irradiation of the secondary is strongest, but here the opposite situation is observed. Finally I discuss some potential mechanisms for accretion in NLTT5306 and outline the questions that still need to be answered about this unusual system.

5.2 Data from XSHOOTER

5.2.1 Observations

20 spectra of NLTT5306 were obtained using the XSHOOTER (Vernet et al., 2011) instrument mounted at the ESO VLT-UT3 ('Melipal') telescope in Paranal, Chile. (See Chapter 2 for full description of XSHOOTER specifications). The observations took place on the night of 2014-August-29 between 04:35 – 07:12 universal time as part of programme 093.C-0211(A). The observations were in the wavelength range $0.3 - 2.48 \mu$ using the three independent arms: VIS, UVB, NIR. The 20 exposures, each 300 s long, were taken covering 1.3 orbits giving 15 spectra per full orbit. The airmass ranged between 1.02 – 1.58 and the seeing between 0.63 – 1.3 arcsec. The data and standards were taken in nodding mode. There was a high wind of 13 ms^{-1} at the start of the night which slowed to 8 ms^{-1} which negatively affected the seeing during the night.

5.2.2 Data reduction and analysis

The XSHOOTER data used in this chapter were reduced using GASGANO (v2.4.3) (Izzo et al., 2004) following ESO’s XSHOOTER pipeline (v2.5.2) using the methods described in Chapter 3. The data and standards were taken in nod mode in an A-B-B-A pattern. Nodding during an observation meant that the telescope is shifted up and down - keeping the object still within the slit. The AB pairs are combined for better sky subtraction. Despite the high wind, the UVB and VIS data had high enough signal-to-noise that each frame could be reduced individually in stare mode in exactly the same way as the XSHOOTER data in Chapter 4. Again, the signal-to-noise of the NIR is not as high and therefore these spectra were reduced by combining each A-B-B-A set in slit nod mode.

The data were then analysed in MOLLY using the data analysis methods described in Chapters 3. To summarise, the radial velocity of the $H\alpha$ absorption line was measured using a combination of three Gaussians: two for the wings and one for the core. The best fitting widths found were 30.0, 10.0, and 4.6 nm with depths of -0.12, -0.15, and -0.24 mJy, respectively.

To model the $H\alpha$ emission feature a fourth Gaussian was added to the three used in the absorption model. Its width was fixed to 0.1 nm and its height and position were free to roam. I searched the 0.3 – 2.4 μm wavelength range for features similar to those seen in Longstaff et al. (2017) and identified Na I absorption doublet (5889 Å and 5895 Å). Only one Gaussian was necessary per line as there are no other spectral features at this wavelength.

5.2.3 Refinement of the ephemeris

I used the radial velocities in Table 5.1 of the $H\alpha$ absorption line to refine the ephemeris of NLTT 5306. I fit the equation,

$$V_r = \gamma + K \sin\left(2\pi \frac{t - T_0}{P}\right), \quad (5.1)$$

HJD	$V_r(\text{abs})$	HJD	$V_r(\text{abs})$
-2450000	[km s ⁻¹]	-2450000	[km s ⁻¹]
6899.8384	-31.7 ± 3.8	6899.8770	54.2 ± 4.1
6899.8423	-17.2 ± 3.5	6899.8809	20.0 ± 4.0
6899.8461	-0.1 ± 3.8	6899.8882	-1.1 ± 4.5
6899.8501	23.2 ± 3.8	6899.8921	-17.4 ± 4.0
6899.8539	37.4 ± 3.9	6899.8959	-16.9 ± 4.0
6899.8578	57.5 ± 3.9	6899.8998	-27.3 ± 4.0
6899.8616	67.3 ± 4.5	6899.9036	-30.3 ± 4.4
6899.8655	45.0 ± 4.3	6899.9075	-19.2 ± 4.1
6899.8693	54.1 ± 4.0	6899.9113	-13.5 ± 4.6
6899.8732	62.2 ± 4.1	6899.9152	-7.5 ± 6.7

Table 5.1: The measured XSHOOTER radial velocity data for all 20 frames taken on 2014-Aug-29.

to the measured radial velocities using a least-squares method allowing the systemic velocity, γ , the semi-amplitude, K , the zero point of the ephemeris, T_0 , and the period, P , to roam. Any points more than 3σ away from the model were excluded to improve the fit. 1km s^{-1} was repeatedly added in quadrature to the standard statistical errors until a reduced χ^2 of 1 was achieved resulting in $\sim 6\text{km s}^{-1}$ added in quadrature to the radial velocity of the $\text{H}\alpha$ absorption.

When fitting the $\text{H}\alpha$ emission and Na I absorption T_0 and P were held constant. This resulted in 2 and 0.6km s^{-1} being added to the $\text{H}\alpha$ and Na I radial velocities, respectively. The error bars in Figure 5.1 reflect this increase in the error values. The best fitting orbital parameters can be found in Table 5.2. Figure 5.2 shows the trailed spectra of the $\text{H}\alpha$ line and the Na I doublet; this demonstrates that all of the lines are moving in phase with one another and likely originate from the same place.

It should be noted that I have redefined the zero point of the ephemeris from the one quoted in Steele et al. (2013) to be when the unseen brown dwarf is closest to the observer in order to match with convention.

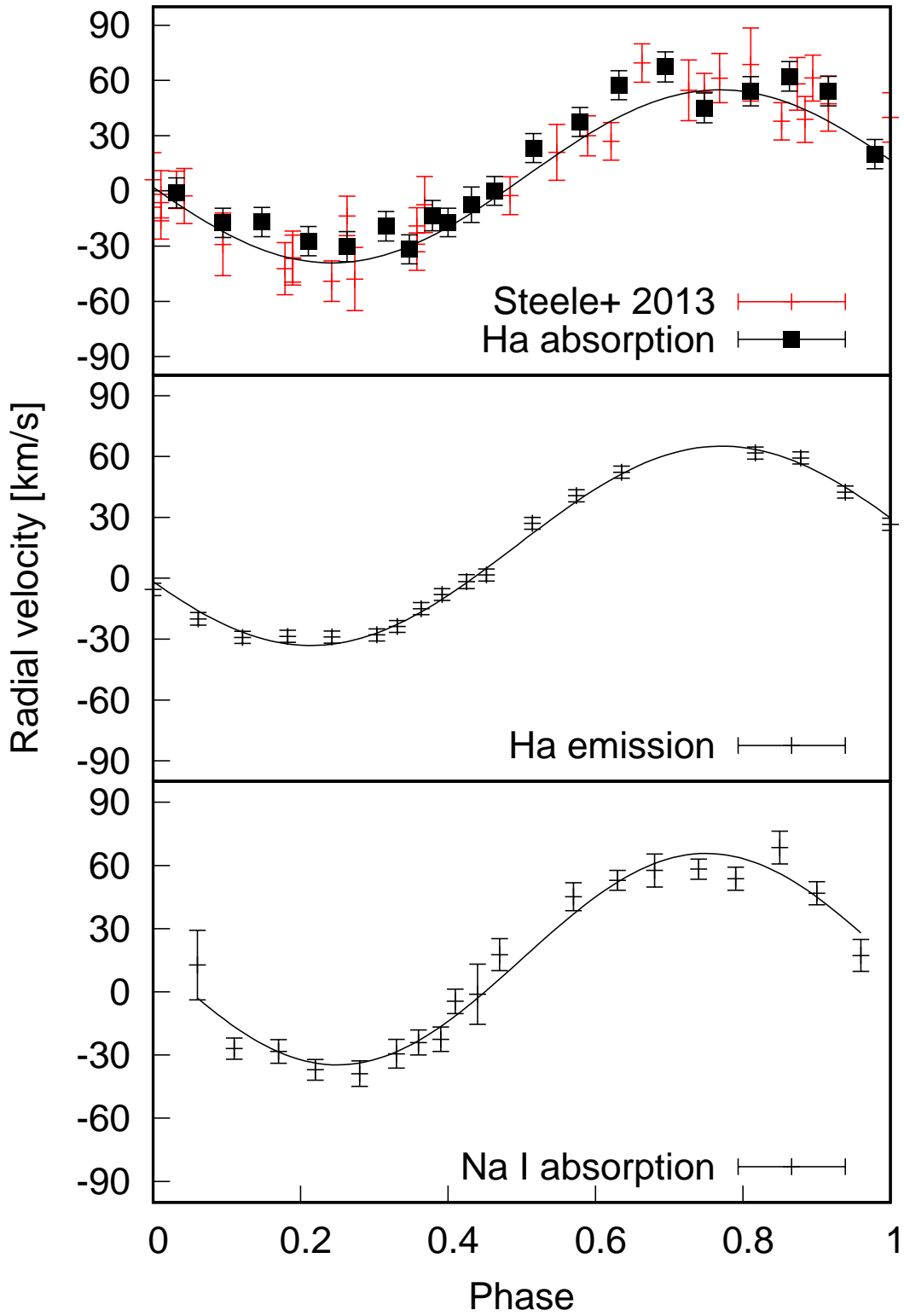


Figure 5.1: Radial velocity measurements made using *MOLLY mgfit* routine have been fit using Equation 5.1 with best fitting values listed in Table 5.2. The $H\alpha$ absorption (top) with Steele et al. (2013) data folded onto the new ephemeris (red '+'), $H\alpha$ emission (middle), and Na I absorption (bottom) lines are all present in the NLTT5306 atmosphere.

System parameters		
P	0.07075025(2)	Days
T ₀	3740.1778(8)	HJD-2450000
K _{H abs}	-46.8 ± 2.5	km s ⁻¹
K _{H em}	-49.1 ± 1.1	km s ⁻¹
K _{Na}	-50.2 ± 6.7	km s ⁻¹
γ _{H abs}	15.6 ± 1.8	km s ⁻¹
γ _{H em}	16.0 ± 1.0	km s ⁻¹
γ _{Na}	15.5 ± 3.5	km s ⁻¹
M _{WD}	0.44 ± 0.04	M _☉
M _{BD}	56 ± 3	M _{Jup}
R _{WD}	0.0156 ± 0.0016	R _☉
Distance	71 ± 4	pc
Separation, a	0.566 ± 0.005	R _☉
Mass ratio, q	0.12 ± 0.01	-

Table 5.2: The parameters of the orbit of NLTT5306 found by fitting Equation 5.1 to a combined data set of our measured radial velocities and the radial velocities published in Steele et al. (2013). Zero phase is defined as when the white dwarf is furthest from the observer. The values below the centre line are taken from Steele et al. (2013) and listed here for convenience due to their use in this work.

5.2.4 Measuring H α emission line strength

To determine if the strength of the hydrogen emission line was varying I calculated the equivalent width of the line for each of the 20 spectra. The equivalent width was determined using,

$$W = \int_{\lambda_1}^{\lambda_2} \frac{F_c - F_\lambda}{F_c} d\lambda, \quad (5.2)$$

where F_c is the continuum intensity and F_λ is the intensity over the wavelength range of interest,

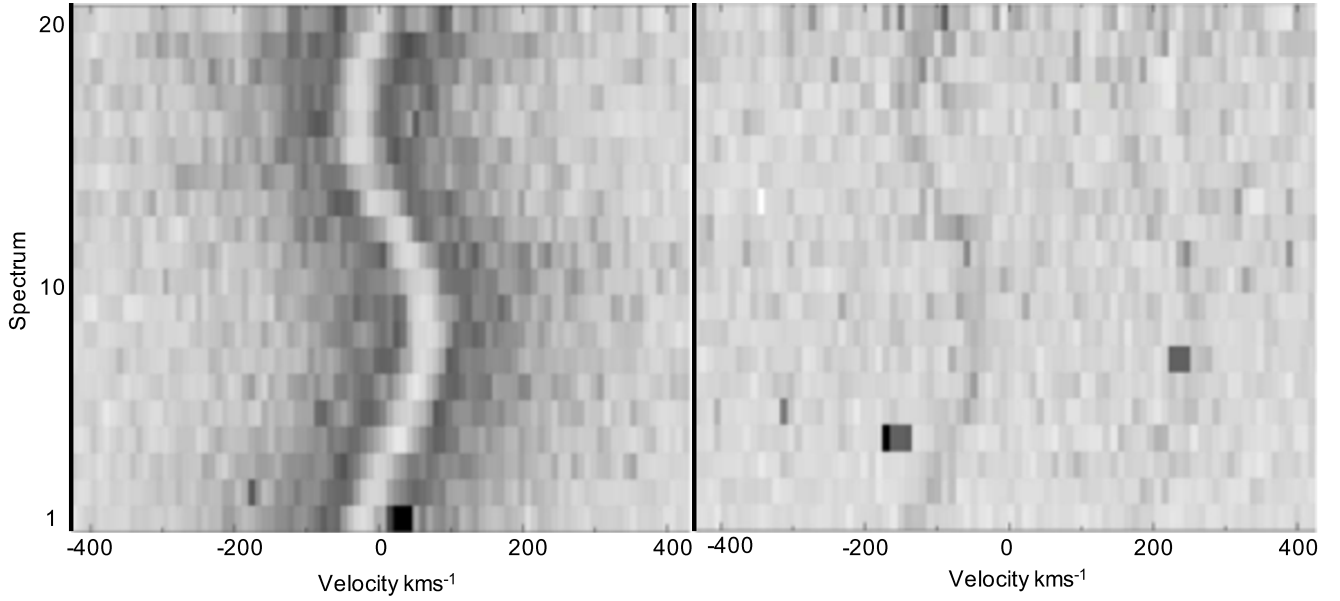


Figure 5.2: **Left:** The trailed spectrum of the $H\alpha$ line. The emission (white) traces the path of the absorption (dark grey). **Right:** The trailed spectrum of the 5889.95 Å and 5895.92 Å Na I lines.

$d\lambda$. The $H\alpha$ line is strong enough for this to be done over a full phase, however the emission feature is in the core of the the $H\alpha$ absorption feature. Figure 5.3 demonstrates how I modelled the absorption feature and subtracted this from our data leaving only the emission, with which I calculated equivalent width. The measured equivalent widths can be seen on the right of Figure 5.3. The line is weakest between $\phi = 0.25 - 0.45$ and strongest between $\phi \sim 0.60 - 0.85$. The equivalent width never reaches a width of 0 Å meaning that the $H\alpha$ emission region on the white dwarf is never out of the line of sight of the observer. A $\phi \sim 0.25$ offset can clearly be seen in the right hand panel of Figure 5.3 which suggests that the orbital period of the emission region is not in phase with the orbital period of the system.

I measured the equivalent width of the Na I $\lambda 5889$ line to be 0.12 ± 0.02 Å and the weaker Na I $\lambda 5895$ line was measured to be 0.02 ± 0.02 Å, however, the signal to noise of the latter line is far lower than the former.

$H\alpha$ emission coming from the white dwarf whose strength varies with orbital phase, coupled with the unusual presence of a lone Na I detection is indicative of accretion. For this reason further observations were acquired using the UVOT camera on board the *Swift* Telescope.

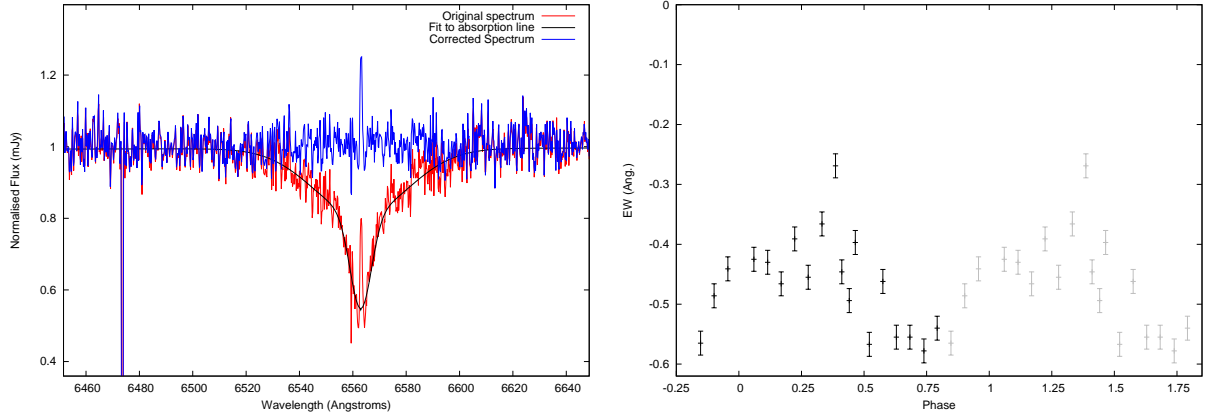


Figure 5.3: **Left** shows the original spectrum (red) with the fit to the absorption feature (black) that was subtracted to leave only the emission feature (blue). **Right** shows how the $H\alpha$ measured equivalent widths vary with phase a phase shift of ~ 0.25 can clearly be seen. This has been duplicated over two phases with the duplicate data plotted in grey.

5.3 Data from *Swift*

In order to determine if there were any high energy emissions from NLTT5306, observations were taken using *Swift* as it allows for simultaneous observation in UV and X-ray wavebands.

5.3.1 ToO observations and analysis

Swift was able to detect NLTT5306 in an initial Target Of Opportunity (ToO) observation. Prior to this I calculated predicted magnitudes for comparison. I convolved a pure Hydrogen, homogeneous, plane-parallel, LTE white dwarf model ($T_{\text{eff}} = 7750 \text{ K}$; $\log g = 7.75$, Koester 2010) with three *Swift* filter profiles: uvw1, uvm2, and uvw2. These filter profiles have been plotted alongside the white dwarf model spectrum in Figure 5.4 and their central wavelengths can be found in Table 5.3.

The ToO observation (target ID: 34661) took place on 2016-August-09. A 400 s snapshot per filter was taken in Image mode. Image mode produces a 2D sky map which is aspect corrected before being made available for further processing.

Filter	Effective wavelength (Å)	Predicted magnitude
W1	2589.1	18.45 ± 0.2
M2	2228.1	18.94 ± 0.2
W2	2030.5	19.58 ± 0.2

Table 5.3: The predicted magnitudes for observations using UVOT in three wavebands. The effective wavelengths have been taken from Rodrigo et al. (2012).

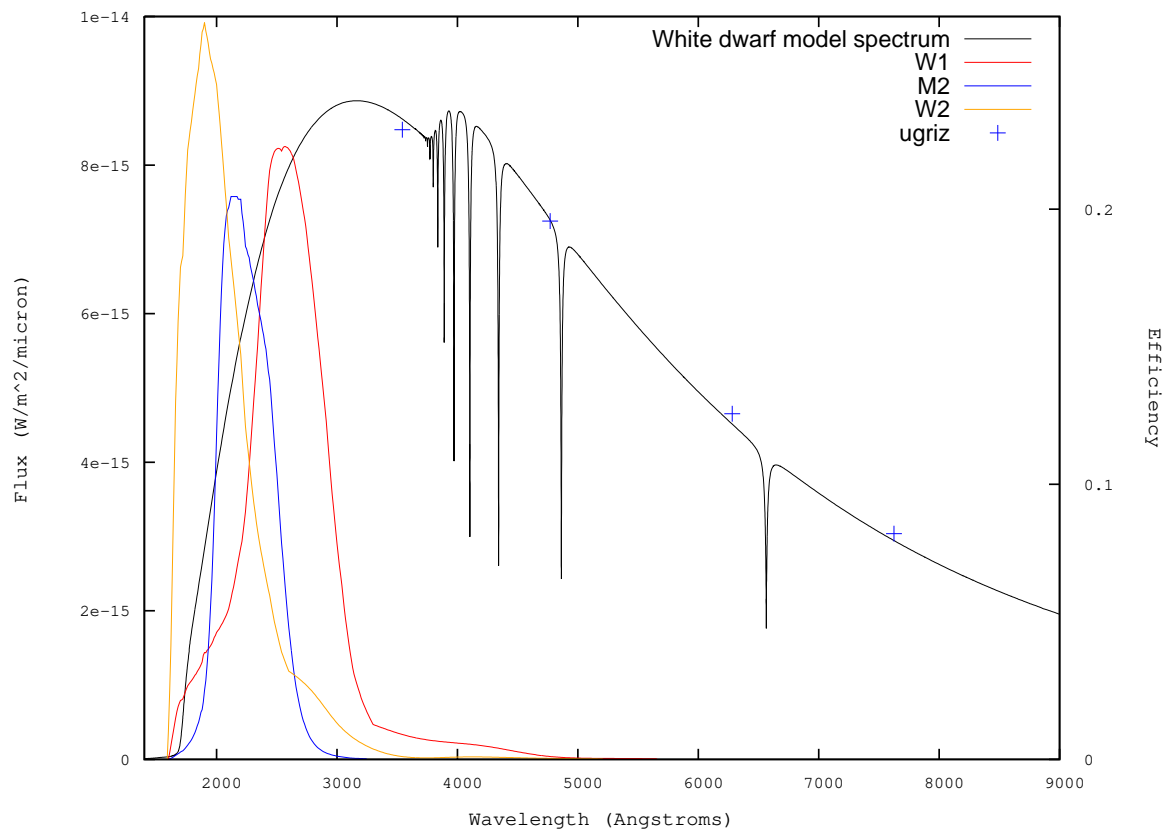


Figure 5.4: The white dwarf model and the three filter profiles uvw1 (red), uvm2 (blue), and uvw2 (yellow). SDSS photometry has been plotted in blue (+) in the five filter bands, u , g , r , i , and z .

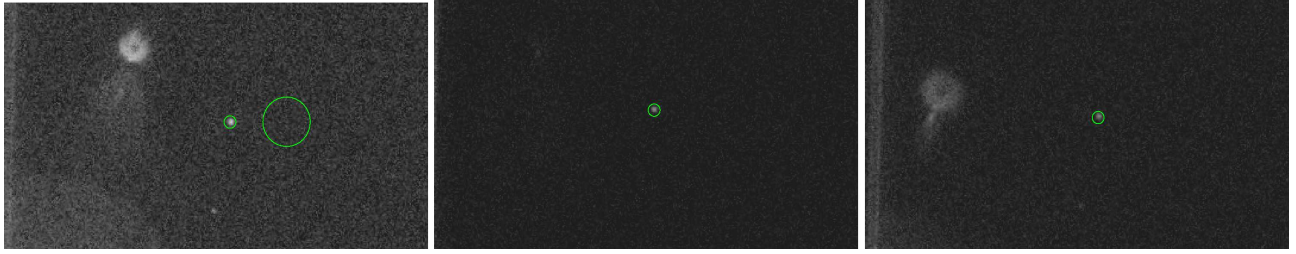


Figure 5.5: Example image of the ToO reduction showing the selection of the target and a background region.

In each waveband and a signal-to-noise ratio of >15 was achieved. I used the standard UVOT analysis pipeline¹¹ to derive magnitudes. For each image a source region of $5''$ was selected around NLTT5306 and a $20''$ background region was selected from a nearby blank region (see Figure 5.5). I set the background threshold to 3σ . Aperture photometry was performed on each image by taking the source and background regions and running, UVOTSOURCE (Evans et al. (2007), Evans et al. (2009)).

From Figure 5.5 it is clear that *Swift* did detect NLTT5306 in all three wavebands. These observations were performed at $\phi = 0.6 - 0.7$ when the brown dwarf is furthest from to the observer.

5.3.2 GI observations and analysis

I followed up the initial ToO with further observations in the same filters as part of the GI program (target ID: 93147) to get full orbital coverage. Ideally continuous observations would have been performed however *Swift* has a maximum snapshot length of ~ 1.8 ks. Consequently the observations consisted of nine ~ 1.5 ks snapshots (three per filter) culminating in a total observation time of 13.1 ks (Target ID: 00093147001 - 9). Two of the nine observations were repeated; one due to an interruption (00093147005), and one due to the observation being split into smaller snapshots significantly lowering the signal-to-noise (00093147008). A summary of observations are listed in Table 5.4. All all GI program observations were taken in Event mode.

¹¹<http://www.swift.ac.uk/analysis/uvot/index.php>

Filter	Target ID	Start time	Stop time	Obs ID	UVOT exposure
All	34661	2016-08-09T16:06:58	2016-08-09T17:13:52	34661001	1051.42
	93147	2017-06-07T00:52:57	2017-06-07T01:46:57	93147001	1618.32
W1	93147	2017-06-07T08:50:57	2017-06-07T09:44:01	93147002	1674.38
	93147	2017-06-07T16:52:57	2017-06-07T17:46:07	93147003	1667.89
	93147	2017-06-14T00:17:57	2017-06-14T01:11:40	93147004	1635.64
M2	93147	2017-06-14T08:15:57	2017-06-14T09:09:53	93147005	242.206
	93147	2017-06-14T16:15:57	2017-06-14T17:09:41	93147006	1634.65
	34661	2017-07-24T16:07:57	2017-07-24T17:01:41	34661002	1634.45
	93147	2017-06-17T00:02:57	2017-06-17T00:57:52	93147007	1562.78
W2	93147	2017-06-17T08:30:57	2017-06-17T12:06:43	93147008	1501.51 ¹
	93147	2017-06-17T17:36:57	2017-06-17T18:30:30	93147009	1645.68
	93147	2017-06-29T18:12:57	2017-06-29T19:48:20	93147010	1634.27

Table 5.4: Details of all *swift* observations of NLTT5306. ¹This observation was split into 4 smaller snapshots therefore a fourth observation was done to compensate for this.

Event mode provides a 2D sky map similar to Image Mode however each individual photon or ‘event’ is tagged with an associated start and stop time. The reduction process is as follows. First the raw coordinate positions are converted into detector and sky coordinates using the generic FTOOL command, COORDINATOR. The events are then screened using time tagged quality information to remove hot pixels using UVOTSCREEN. Source and background regions are selected – in an identical way to the Image Mode reduction – and the background subtracted. At this point the magnitude of NLTT5306 was determined for comparison to the predicted magnitudes listed in Table 5.5.

From the reduced images I created a lightcurve using UVOTEVTLC to select the time bin sizes. I divided each ~ 1.5 ks snapshot into 400 s bins to reduce the error on each point to < 0.5 per cent. I have plotted phase folded lightcurves for each filter in Figure 5.6

Filter	Effective wavelength (Å)	Predicted magnitude	Measured magnitude
uvw1	2589.1	18.45 ± 0.2	18.15 ± 0.1
uvm2	2228.1	18.94 ± 0.2	18.68 ± 0.1
uvw2	2030.5	19.58 ± 0.2	19.04 ± 0.1

Table 5.5: The predicted magnitudes compared to the measured magnitudes from observations using UVOT in three wavebands. The effective wavelengths have been taken from Rodrigo et al. (2012).

From Figure 5.6 no significant periodic variability on the period of the system appears to be present. Plotting a straight line at the average magnitude for each waveband shows how little variability there is. I calculated the median average deviation as a percentage to be 1 per cent. To investigate the small scatter I compared the lightcurves of NLTT5306 to those of three other sources in the same field. These reference sources showed very similar percentage deviations thus I conclude there is no detectable variability in the data. The scatter is likely due to systematics, potentially related to the background subtraction or the movement of the spacecraft.

5.3.3 Modelling the spectra and photometry

I combined the white dwarf model described in Section 5.3.1 with L3 – L7 brown dwarf spectra (Cushing et al., 2005) taken from SpeX on the IRTF. I normalised the XSHOOTER UVB, VIS, and NIR spectra to the g , z and J bands, respectively, ensuring they form a smooth continuum. From Figure 5.7 it can be seen that the model is consistent with the Sloan Digital Sky Survey (SDSS) $ugriz$, UKIRT Infrared Deep Sky Survey (UKIDSS) $YJHK$, and Wise (W1, W2) photometry. From Table 5.5 the W2 band is marginally brighter than predicted; and when viewed closely the *Swift* photometry does sit slightly above the model in Figure 5.7. This is likely due to an underestimate of the errors on the predicted magnitudes when convolving the white dwarf model with the *Swift* filter profile. The error in the predicted magnitudes was estimated based upon the

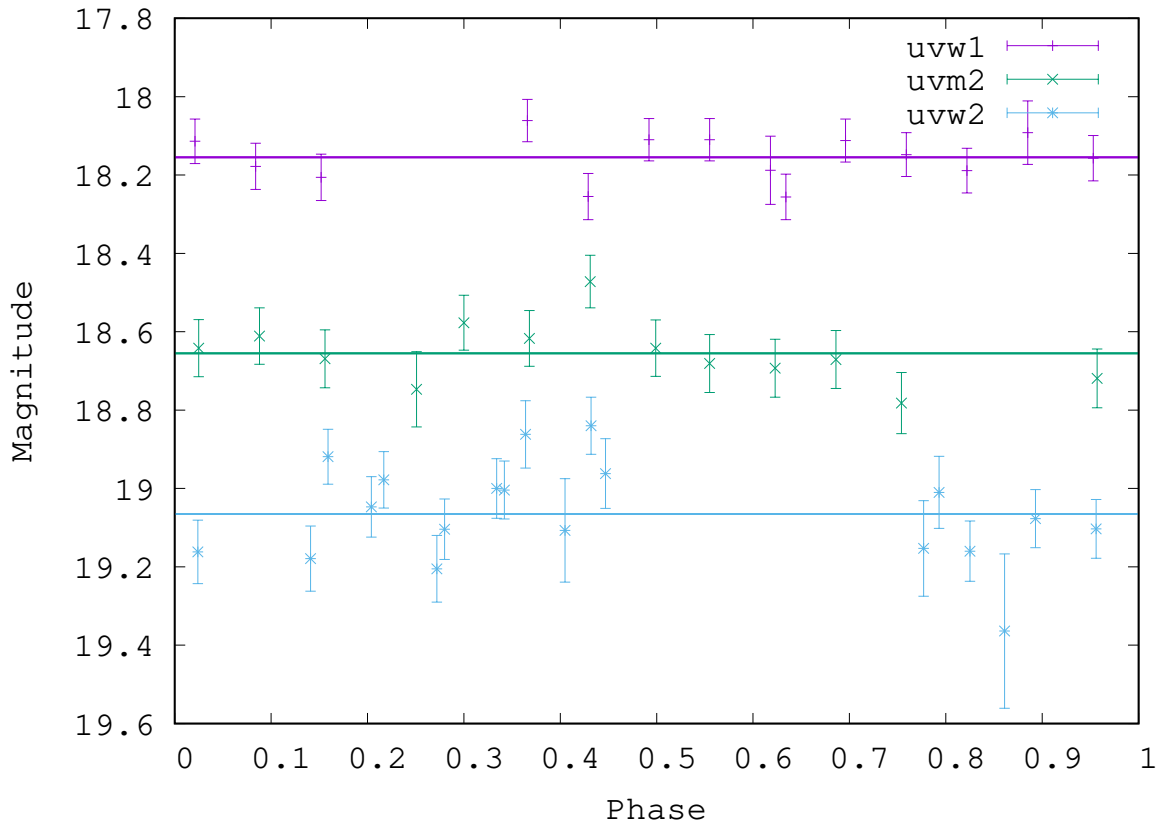


Figure 5.6: Measured magnitudes in three filters: uvw1, uvm2, and uvw2. Observations were taken covering as much of an orbit as possible. The horizontal lines are the average of the data points in each filter.

$\sim 1\%$ error of the white dwarf model used.

5.3.4 Placing an upper limit on the accretion rate

There were no X-ray detections from any of my *Swift* X-Ray Telescope (XRT) observations. This allowed me to determine an upper limit set by the cosmic background constantly detected by XRT. This gives an X-ray upper limit of $6.4 \times 10^{-4} \text{ counts s}^{-1}$ using the online Build XRT products page². From this I calculated a flux limit of $1.68 \times 10^{-14} \text{ ergs cm}^{-2} \text{ s}^{-1}$ using the *Swift* online data analysis tools (Evans et al. 2007, 2009) and *WebPIMMS*³. The *Swift* analysis software is part of the High Energy Astrophysics Software (HEASoft). The standard pipeline processing of

²[http://www.swift.ac.uk/user objects/](http://www.swift.ac.uk/user%20objects/)

³<https://heasarc.gsfc.nasa.gov/cgi-bin/Tools/w3pimms/w3pimms.pl>

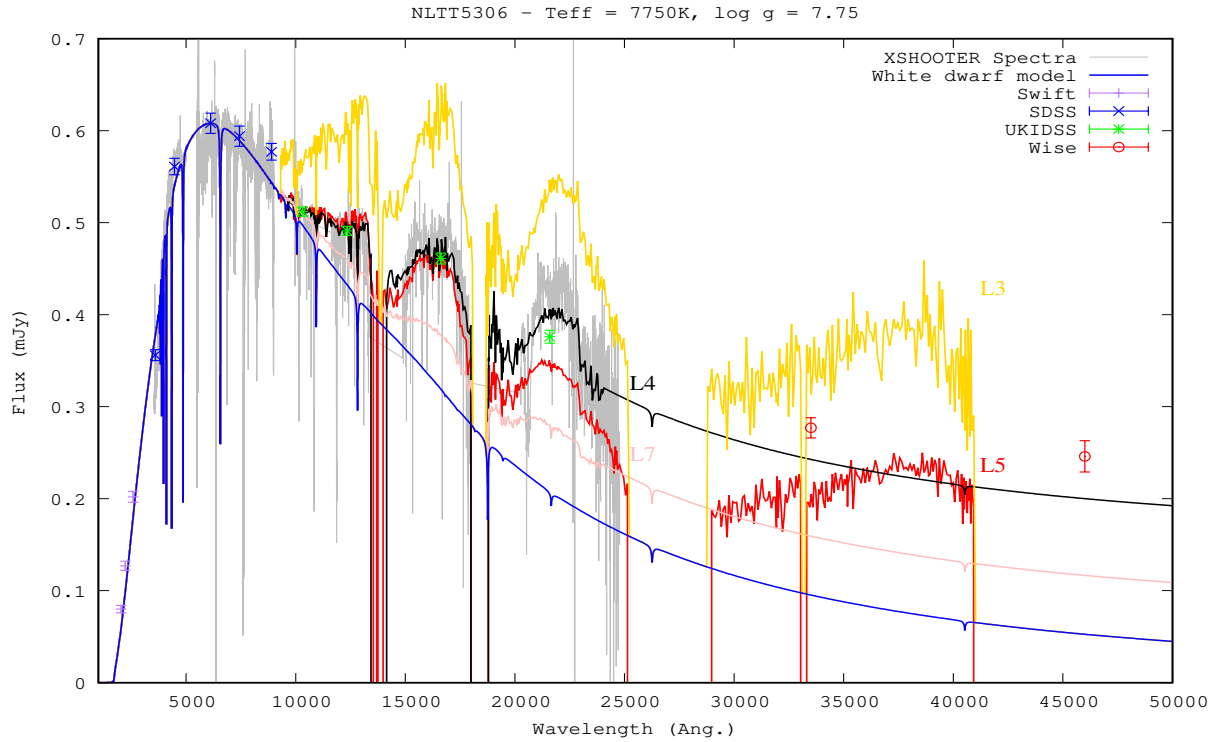


Figure 5.7: A composite of the white dwarf model spectrum (blue line) and a sequence of brown dwarf template spectra from L3 – L7 (labelled). Swift photometry is plotted in purple (+), SDSS *ugriz* in blue (x), UKIDSS *Y*, *J*, *H* and *K* in green (*) and Wise W1 and W2 in red (o).

Swift data ensures that the sky coordinates are correctly attained for each event. The stages of the pipeline include standard calibration, screening and filtering. The raw data are calibrated, a list of screened events are extracted, and the events filtered (spatially, temporally or spectrally) and the data are binned appropriately for extraction. These data products can then be accessed online.

Using the Gaia DR2 distance to NLTT5306 of 77pc and the white dwarf mass and radius listed in Table 5.2, I found an upper limit X-ray luminosity, $L_x = 4\pi D^2 F$, of $1 \times 10^{28} \text{ erg s}^{-1}$. From this I calculated an upper limit on the mass accretion rate to be $2 \times 10^{-15} M_{\odot} \text{ yr}^{-1}$.

Inclination	Roche Lobe radius	Filling factor
deg	R_{\odot}	%
25	0.1553	61
35	0.1428	67
50	0.1316	72
90	0.1219	78

Table 5.6: The results of Roche Lobe radius calculations for four different inclinations

5.3.5 Accretion mechanisms

The main possible mechanisms for mass transfer are Roche lobe overflow or via a wind from the donor. In each case, the mass flow may form a disc or, if the white dwarf is sufficiently magnetic, may be channelled along field lines down to the magnetic poles of the white dwarf.

Roche lobe overflow

The Roche lobe is the region surrounding each object in a binary system, indicating the area of its gravitational dominance. When a star exceeds its Roche lobe, mass can be lost to the Roche lobe of its companion. This is referred to as mass transfer via Roche-lobe overflow (Eggleton, 1983)

Using the mass ratio of the system, $q = \frac{M_T \sin(i)}{M_1}$, and the orbital separation, a , listed in Table 5.2 I calculated an estimate of the Roche lobe radius R_L of the brown dwarf for four different inclinations. Using the Breedts et al. (2012) improvements on the Eggleton (1983) calculation for the Roche lobe radius of a cataclysmic variable below the period gap in Equation 1,

$$\frac{R_L}{a} = \frac{0.5126q^{0.7388}}{0.6710q^{0.7349} + \ln(1 + q^{0.3983})} \quad (5.3)$$

and the Steele et al. (2013) value for the brown dwarf radius of $0.095 \pm 0.004 R_{\odot}$, I estimate that NLTT5306B is filling between 60 – 80% of its Roche Lobe.

It is possible for a companion with a predicted radius smaller than the radius of its Roche lobe

to still be Roche lobe filling, if the primary star in the system is very hot, causing inflation of the radius of the brown dwarf. For example, the millisecond pulsar SAX J1808.4–3658 has a companion brown dwarf of mass $0.05 M_{\odot}$, which is not large enough to fill its Roche lobe. Despite this, Bildsten & Chakrabarty (2001) detect a time averaged mass transfer rate of $\dot{M} \approx 10^{-11} M_{\odot} \text{ yr}^{-1}$. This is attributed to continuous heating from the neutron star, inflating the brown dwarf to a radius of $\approx 0.13 R_{\odot}$. They estimate the day-side of their brown dwarf to be between 3800–4800 K, much hotter than the 1700 K Steele et al. (2013) predict for NLTT5306B. Similarly Kelt-1b – a $27 M_{\text{Jup}}$ brown dwarf orbiting a ≈ 6500 K mid-F star in a 29 hour orbit – receives a large amount of stellar insolation which suggests the radius is likely to be significantly inflated (Siverd et al., 2012).

Contrastingly when examining eclipsing white dwarf – brown dwarf binary systems hotter than NLTT5306 I found the brown dwarf companions are not inflated. For example, SDSS J141126.20+200911.1 contains a 13000 K white dwarf with a $\approx 50 M_{\text{Jup}}$ brown dwarf with a relatively small radius of $0.072 R_{\odot}$ (Littlefair et al., 2014). Similarly SDSS J1205-0242 has a ~ 23600 K white dwarf that irradiates a $\approx 50 M_{\text{Jup}}$ brown dwarf with a radius of $0.081 R_{\odot}$ (Parsons et al., 2017). Additionally, the non-eclipsing system, WD0137-349AB, contains a 16 500 K white dwarf and a brown dwarf with a similar mass, yet accretion signatures are not seen. Therefore it is unlikely that NLTT5306A, at $T_{\text{eff}} = 7700$ K, is hot enough to significantly inflate the brown dwarf.

Interestingly, NLTT5306B displays a distinct triangular shape in the H -band (see Fig. 3 in Steele et al. (2013)), suggestive of low surface gravity (Kirkpatrick et al., 2006) which could mean the brown dwarf atmosphere is extended. This feature is usually only seen in young (e.g. 10s of Myr) sub-stellar objects (Allers & Liu, 2013). NLTT5306B is estimated to be ~ 0.5 Gyr, and the cooling age of the white dwarf is 710 Myr (Steele et al., 2013) and so we would not expect to see evidence of low gravity at this age.

Magnetic interaction

The companions in Low Accretion Rate Polars (LARPs) and, possibly, some polars are thought to slightly underfill their Roche Lobes, with accretion taking place through magnetic funnelling of

a wind from (or material close to the surface of) the secondary onto the poles of the white dwarf (King, 1985). These systems are characterised by containing white dwarfs with strong magnetic fields of >10 MG (Schwope et al., 2002). The strength of the magnetic field and what precisely makes some white dwarfs magnetic, and others not, is still very much an open topic in this field. A magnetic field is typically detected through Zeeman splitting of spectral lines and/or cyclotron humps. I do not see any cyclotron humps in the spectral data; nor do I detect any Zeeman splitting of the H lines.

The upper limit on the accretion rate implies a critical magnetic field strength required to prevent the formation of an accretion disk thus leading to magnetic channelling of mass. To disrupt disk formation, the magnetic radius, r_m , which de-marks the region in which the magnetic field of the white dwarf is expected to dominate the accretion dynamics, would have to be at least equal to the circularisation radius, R_{circ} , given by Frank et al. 2002,

$$\frac{R_{\text{circ}}}{a} = (1 + q)(0.5 - 0.227 \log_{10}(q))^4, \quad (5.4)$$

where q is the mass ratio and a is the orbital separation. For NLTT5306 we find this value to be 1.1×10^{10} cm ($\approx 10 R_{\text{WD}}$) using the component masses and separation (Table 5.2). By equating the ram pressure, ρv^2 , to the magnetic pressure, $B^2/8\pi$, the magnetic radius can be written as,

$$r_m = 5.1 \times 10^8 \dot{M}_{16}^{-\frac{2}{7}} m_1^{-\frac{1}{7}} \mu_{30}^{\frac{4}{7}}, \quad (5.5)$$

where \dot{M}_{16} is the mass accretion rate in units of 10^{16} gs^{-1} , m_1 is the mass of the white dwarf in solar masses and μ_{30} is the white dwarf magnetic moment in units of 10^{30} Gcm³ (see e.g. Frank et al. 2002). Setting Equation 5.5 equal to the circularisation radius and adopting the white dwarf radius from Table 5.2, I found a critical magnetic field of 0.45 ± 0.02 kG is all that is needed to prevent the formation of an accretion disc. I would expect any white dwarf to be at least this magnetic (Scaringi et al., 2017), which makes this result consistent with the lack of any observational evidence for a substantial accretion disk. The accretion flow in NLTT5306 is therefore highly likely to be magnetically controlled.

Wind from a companion

In some cases the compact primary is able to capture a fraction of material from a companion via a wind. This is known as wind accretion and, typically, the wind originates from stellar companions. For example, V471 Tau captures the coronal mass ejections from the K-dwarf (Bois et al., 1991; Sion et al., 2012). Similarly, LTT 560 displays $H\alpha$ emission on the white dwarf caused by stellar activity from the secondary late-type main-sequence star (Tappert et al., 2011). Unlike stellar objects, brown dwarfs are degenerate and much cooler than stars which is likely the reason why a brown dwarf wind has never been detected. It is unlikely that a wind from NLTT5306B is being generated through irradiation alone since we do not see anything of the sort in similar more highly irradiated systems, including those with very short periods (e.g. Casewell et al. 2018). A low rate of mass loss via a wind is possible if the low gravity implied by the H -band is confirmed (Allers & Liu, 2013).

5.4 Discussion

The presence of $H\alpha$ emission and Na I absorption in the atmosphere of NLTT5396A suggests accretion due to the short (days to weeks) sinking time-scale in DA white dwarfs (Wyatt et al., 2014). However, the lack of high energy emission places strong constraints on the possible rate of accretion. Modulation of the $H\alpha$ emission line strength suggests that the accretion region or ‘hot-spot’ is moving with respect to the observer which could give an insight into the geometry of this non-eclipsing system. To adequately assess how NLTT5306 fits into the context of other interacting systems I compare the accretion rate upper limit to that of similar binaries.

5.4.1 Accretion rate

The systems in Tables 1.1 and 1.2 in Chapter 1 have accretion rates orders of magnitude higher than NLTT5306. The CV WZ Sagittae has a rate of $7.5 \times 10^{-13} M_{\odot} \text{ yr}^{-1}$, and the polars SDSS

J121209+013627 and EF Eri: $\sim 10^{-13} M_{\odot} \text{ yr}^{-1}$ (Burleigh et al., 2006; Koen & Maxted, 2006) and $3.2 \times 10^{-11} M_{\odot} \text{ yr}^{-1}$ (Schwope et al., 2007), respectively. Pre-polars have slightly lower rates at $10^{-14} - 10^{-13} M_{\odot} \text{ yr}^{-1}$ (Schmidt et al., 2007). White dwarfs with stellar companions that accrete via a wind have accretion rates from 10^{-19} to $10^{-16} M_{\odot} \text{ yr}^{-1}$ (Debes, 2006; Kawka et al., 2008) and the rate largely depends on the spectral type of the companion.

There are a handful of polluted white dwarfs (white dwarfs with consistently observed metal lines in their spectra) accreting from gas disks, such as SDSS J122859+104032, which has an upper limit accretion rate of $5 \times 10^{-17} M_{\odot} \text{ yr}^{-1}$ (Gänsicke et al. 2006; Brinkworth et al. 2009). The white dwarfs with dust disks have similar accretion rates, for example, $\dot{M} \sim 7 \times 10^{-17} M_{\odot} \text{ yr}^{-1}$ (von Hippel et al., 2007); 10^{-19} to $10^{-16} M_{\odot} \text{ yr}^{-1}$ (Farihi et al., 2018).

SDSS J155720.77+091624.6, a unique system consisting of a white dwarf - brown dwarf binary with a circumbinary debris disk, has a steady state of accretion at an inferred rate of $\dot{M} \simeq 9.5 \times 10^{-18} M_{\odot} \text{ yr}^{-1}$ (Farihi et al., 2017), while WD1145+017, a system with multiple transiting objects thought to be disintegrating planetesimals (Vanderburg et al., 2015), has a steady state mass accretion rate of $6.7 \times 10^{-16} M_{\odot} \text{ yr}^{-1}$ (Xu et al., 2016).

One system that does have a similar accretion rate is LTT 560 (Tappert et al., 2007). LTT 560 is a white dwarf + M-dwarf PCEB that displays $H\alpha$ emission associated with the white dwarf. The mass accretion rate was estimated to be $\sim 5 \times 10^{-15} M_{\odot} \text{ yr}^{-1}$ by Tappert et al. (2011) and the accretion mechanism is thought to be a stellar wind from the M dwarf companion.

The above comparisons put the upper limit well below that of CVs and polars, by at least two orders of magnitude, and an order of magnitude above rates due to wind and gas/dust disk accretion. From Figure 5.7 we can see the Wise photometry is consistent with a white dwarf + L3 – L5 dwarf model with no sign of an infrared excess indicative of a disk. Nor have I detected any $H\alpha$ emission from anywhere other than the white dwarf surface. This evidence implies that no disk has formed therefore the mechanism for accretion is more likely to be magnetic funnelling of a light brown dwarf wind.

5.5 Conclusions

$H\alpha$ emission and Na I absorption associated with the white dwarf lead me to believe accretion is happening in NLTT5306. The lower limit on the accretion rate and the lack of any observational evidence for an accretion disk, suggests accretion may be occurring via magnetic channelling of a wind from the donor. The phase-offset orbital variation of the $H\alpha$ emission line strength indicates a potential hot-spot on the white dwarf surface, further supporting the magnetically channelled wind interpretation. Yet, the lack of any detectable high energy emissions, Zeeman splitting, or cyclotron humps conflicts with this.

The possibility that the triangular shape of the H-band does indeed indicate low surface gravity, then it may be possible for a wind to escape from NLTT5306B. The low critical magnetic field (0.45 kG) required to prevent a disk forming from matter accreting at a rate of $2 \times 10^{-15} M_{\odot} \text{ yr}^{-1}$ indicates there is scope for such a wind to be magnetically channelled through the bulk of the system. At the same time, the field and mass transfer rate are too low to produce detectable Zeeman or cyclotron features. Furthermore, it may be possible the magnetic field of the white dwarf plays a role in the stripping of any loosely bound material close to the surface of NLTT5306B.

This work demonstrates that NLTT5306 is a useful target for mapping the transition from post-common envelope binary to pre-cataclysmic variable. The broad spectrum observations clearly indicate that a higher signal-to-noise is required. For example, systems with lower accretion rates than NLTT5306 have X-ray detections (e.g. Farihi et al. 2018), requiring observations using more sensitive observatories such as XMM-Newton. Furthermore, magnetic fields weaker than 2 MG are only detectable for the highest S/N spectra (e.g. Tout et al. 2008) therefore thorough circular spectro-polarimetry observations are required to verify a magnetic field.

6

Spectroscopically classifying white dwarf + brown dwarf candidate systems using the Gemini near-infrared spectrograph

In this Chapter I will address the final aim of this thesis: to discover more white dwarf - brown dwarf systems. If successful, this will provide a good starting point for further research into determining if these systems are close binaries.

6.1 Introduction

In this chapter I investigate eight white dwarfs with photometrically confirmed infrared excesses. The photometric infrared excess can be caused by a red companion such as a brown dwarf in orbit about the white dwarf. To categorically determine the nature of the cause of the red excess spectroscopic analysis must be done. I use new low resolution spectroscopy from Gemini near infrared spectrograph (GNIRS) to spectroscopically examine these potential white dwarf - brown dwarf systems. Table 6.1 is a summary of the properties of each white dwarf from the literature. I have included the most recent distances derived from the *Gaia* DR2 parallaxes (Gaia Collaboration et al. 2016, 2018; Luri et al. 2018).

6.1.1 Discovering white dwarfs with infrared excesses

Over the last 20 years many surveys have been performed that have observed white dwarf stars. The Sloan Digital Sky Survey (SDSS) (York et al., 2000) has discovered tens of thousands of DA white dwarfs in its data releases 1 - 14 (DR1 - DR14). A prominent catalogue that has been the foundation for much further work discussed in this Chapter, was created by Eisenstein et al. (2006) based on SDSS DR4. They produced a catalogue of 9316 spectroscopically identified SDSS white dwarfs, 6000 of which were new discoveries. This was followed by Kleinman et al. (2007) which looked at DR7 and Kepler et al. (2015) that looked at DR10.

The UKIRT Infrared Deep Sky Survey (UKIDSS) (Lawrence et al., 2007) is the NIR counterpart to the SDSS. The Large Area Survey (LAS) makes observations in the YJHK filters. Therefore, through cross-correlation of SDSS and UKIDSS LAS catalogues of white dwarfs, infrared excesses can be identified. An infrared excess is where observations in the infrared bands ($\sim 1 - 2.5\mu\text{m}$) is higher than what a model would predict.

Steele et al. (2011) performed a near-infrared photometric search for unresolved sub-stellar companions around white dwarfs in the UKIDSS LAS and identified 9–11 candidate white dwarf + brown dwarf systems. From this they estimated a brown dwarf companion fraction of $\leq 0.5 \pm 0.3\%$.

SDSS J	Short name	T _{eff} K	log g	Spectral Type	WD mass M _☉	Distance pc	References
075132.52 +200216.94	0751+2004	16749±62	8.046±0.044	DBA	0.54	223 ⁺⁸ ₋₈	3, 4
090759.59 +053638.13	0907+0536	19474±293	7.82±0.05	DA	0.54±0.02	323 ⁺²⁶ ₋₂₂	1, 2,3
095042.31 +011506.56	0950+0115	21785±365	7.89±0.06	DA	0.49±0.02	321 ⁺⁶⁶ ₋₄₇	1, 3
100300.08 +093940.16	1003+0939	22331±435	7.87±0.06	DA	0.57±0.03	413 ⁺⁹⁷ ₋₆₆	1, 2
101049.48 +040722.50	1010+0407	13588±668	7.76±0.11	DA	0.48±0.05	275 ⁺²⁴ ₋₂₁	1, 3
101532.30 +042447.66	1015+0425	34526±86	7.38±0.07	DA	0.41±0.02	792 ⁺¹⁷³ ₋₁₂₁	1, 3
101607.45 +002027.04	1016+0020	21045±703	8.48±0.12	DA	0.92±0.07	359 ⁺⁸⁷ ₋₅₉	1, 3
103736.57 +013905.11	1037+0139	16300±221	7.73±0.05	DA	0.49±0.02	358 ⁺³⁰ ₋₂₆	1, 2, 3

Table 6.1: This table summarises key properties of the eight white dwarf - brown dwarf candidate systems investigated. This distances have been updated according to Gaia DR2. References: Eisenstein et al. (2006) (1), Steele et al. (2011) (2), Girven et al. (2011) (3), Kepler et al. (2015) (4), Kepler et al. (2016) (5)

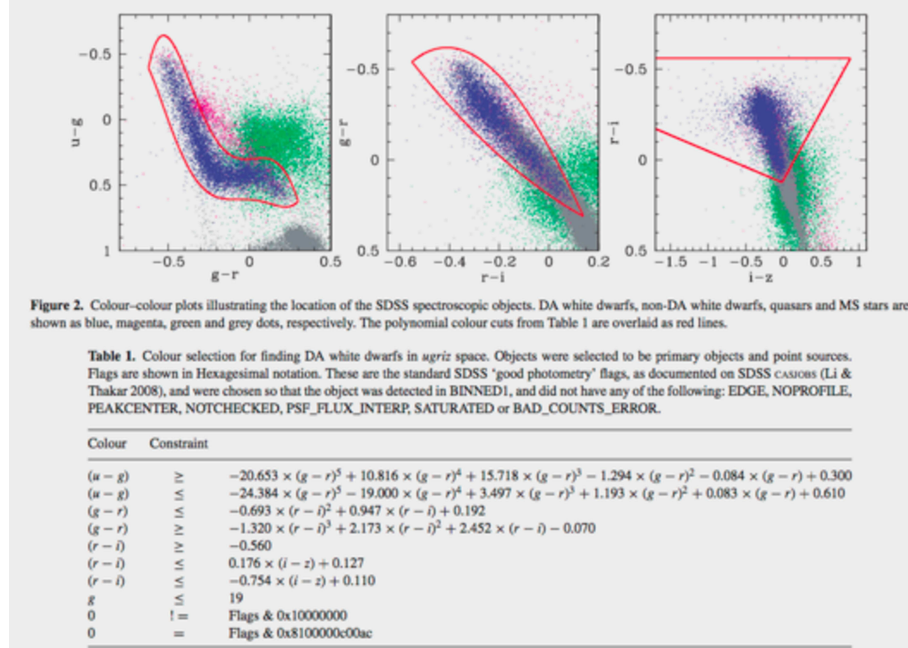


Figure 6.1: This shows the colour-colour plots illustrating the location of the SDSS spectroscopic objects; DA white dwarfs are shown in blue. The table beneath the plot lists the polynomials used to perform the colour cuts to select white dwarfs; these are overlaid as red lines. Credit: DA white dwarfs in Sloan Digital Sky Survey Data Release 7 and a search for infrared excess emission. *Mon Not R Astron Soc.* 2011;417(2):1210-1235. doi:10.1111/j.1365-2966.2011.19337.x

Girven et al. (2011) used photometrically and spectroscopically identified white dwarfs to perform a similar analysis and found 8-10 systems with predicted companion massed in the range associated with brown dwarfs. They estimate the unresolved ($<2''$) brown dwarf companion fraction to DA white dwarfs to be between 0.3 – 1.3%.

At a similar time Debes et al. (2011) performed a cross-correlation of the preliminary SDSS DR7 white dwarf catalogue between the WISE, Two-Micron All Sky Survey (2MASS), UKIDSS, and SDSS DR7 photometric catalogues. They identified 42 candidate white dwarf - brown dwarf systems and suggested all need to be confirmed with infrared spectroscopy. They calculated their observed brown dwarf companion frequency to be $1.3\% \pm 0.6\%$.

Girven et al. (2011) performed colour-colour cuts on the SDSS photometry to select white dwarfs with hydrogen-rich (DA) atmospheres without the recourse to spectroscopy. The cuts they made

and the polynomials that defined them are in Figure 6.1. Using this method they were about to identify 5819 DA white dwarfs. Their approach was also applied to SDSS DR7 for objects with and without SDSS spectroscopy. From the spectroscopic sample they found that 0.8 - 2% of white dwarfs have an excess consistent with a brown dwarf type companion. From the white dwarfs with photometry only, they found 1.8% of white dwarf are candidates for having brown dwarf companions. Gentile Fusillo et al. (2013) build on the method of Girven et al. (2011) by cross-correlating SDSS DR7 with DR8 of UKIDSS LAS. Candidates were examined for an excess by comparing the white dwarf model flux with the observed near-infrared magnitudes and found 2.0% of the spectroscopic DA white dwarfs may have a companion of type L0 or later.

Each study suggests a slightly different estimate of the brown dwarf companion fraction to white dwarf stars. This stems from the different sample sizes and selection techniques when cross-correlating. From these studies the companion fraction is likely to be of the order 1 – 2%. This is to be expected from the brown dwarf desert and therefore is not surprising that the known number of white dwarf - brown dwarf binaries is still only 10 (See Chapter 1).

6.2 Data reduction

Gemini/GNIRS cross-dispersed near-infrared spectra over 18 nights between 2017-01-10 to 2017-04-13 using the Gemini Near-Infrared Spectrograph (GNIRS) on the Gemini North 8 m telescope in Hawaii. They were taken in Service mode through observing program GN-2017A-Q-52. GNIRS cross-dispersed (SXD) spectroscopy mode was utilised, providing complete spectra from 0.8-2.5 μm across five orders (3 - 7). Use of the short (0.15"/pixel) blue camera with its 32 l/mm grating, and a slit of width 0.3" gives an instrumental resolution of $R \sim 1700$.

Each observation was split into 1 hour blocks as is a requirement of the science queue and the exposure time of each science frame was 300 s. Each science target had three observation blocks (OBs) with the exception of 1003+0939 which has four. The data were taken in AB pairs and the targets were not extended objects therefore in each frame a blank region of sky was observed. This

was to facilitate the removal of night sky emission lines and dark current. Before each sequence of exposures, a set of calibration images was taken consisting of continuum and emission-line lamps for flat fielding and wavelength calibration purposes, respectively.

I reduced and telluric corrected the data using Spextool v4.1 (Cushing et al. (2004), Vacca et al. (2003b)) as outlined in Section 3.1.2. This pipeline was not initially designed for the reduction of GNIRS data however only minor changes are required to allow Spextool to run effectively on GNIRS data (e.g. directories renamed). This pipeline makes use of the IDL package, MPFIT and performs the standard spectral reduction techniques (except flexure correction as this is not necessary for GNIRS) as outlined in Chapter 3. To summarise, I used SPEXTOOL to create a master flat and a wavelength calibration files. I used the XSPEXTOOL routine to flat field and wavelength calibrate the science and telluric standard data. Next I defined and traced the extraction aperture positions before applying a background subtraction. This extraction was done using the optimal extraction methods. I combined the separate spectra into one (multi-order) spectrum, using the XCOMBSPEC routine, to increase the signal-to-noise. Finally, I applied the telluric correction and flux calibration to the combined spectrum using the XTELLCOR-GENERAL routine. The result of this process was a single calibrated spectrum for each OB. I combined the final spectra from each OB to create a single spectrum, per system, for analysis. A table of the observation dates, the average airmass on each night and the final signal-to-noise ratio achieved for each object is listed in Table 6.2.

6.3 Data Analysis

All of the systems discussed in this Chapter contain a white dwarf primary and a low mass companion. White dwarfs have high surface gravities, due to their small radii, and have either H (DA) or He (DB) dominated spectra. While some white dwarfs, show metal absorption lines due to accretion, or the remnants of their stellar atmospheres, none of these systems do, and hence the models discussed are pure H. There is one exception: SDSS J0751+2004 which is a DB white dwarf and therefore has a He atmosphere. I used an T_{eff} and $\log g$ appropriate model whose object

System SDSS J	Date	Air mass	$N_{\text{exp}} \times T_{\text{exp}}$	Combined signal-to-noise
0751+2004	2017-01-10	1.12	8 x 300	
0751+2004	2017-01-11	1.63	10 x 300	13
0751+2004	2017-01-12	1.01	8 x 300	
0907+0536	2017-01-12	1.04	16 x 300	
0907+0536	2017-01-13	1.41	8 x 300	9
0950+0115	2017-01-14	1.07	8 x 300	
0950+0115	2017-01-15	1.36	8 x 300	10
0950+0115	2017-02-24	1.10	10 x 300	
1003+0939	2017-01-16	1.11	20 x 300	
1003+0939	2017-02-20	1.20	8 x 300	5
1010+0407	2017-02-22	1.04	8 x 300	
1010+0407	2017-02-24	1.04	8 x 300	10
1010+0407	2017-03-06	1.07	16 x 300	
1015+0425	2017-02-16	1.20	8 x 300	
1015+0425	2017-03-19	1.05	8 x 300	11
1015+0425	2017-03-23	1.38	8 x 300	
1016+0020	2017-01-15	1.12	24 x 300	5
1037+0139	2017-04-05	1.11	10 x 300	
1037+0139	2017-04-13	1.25	18 x 300	23

Table 6.2: The observing schedule for each target and the average air mass for each night. The final column lists the signal-to-noise achieved from combining all OBs into one final spectrum.

parameters come from Koester (2010) and Kepler et al. (2015) for this system.

For DA systems with temperatures greater than 20 000 K I used TLUSTY201. For systems with lower temperatures I used the more recent version, TLUSTY205 (Lanz & Hubeny, 2003) as this incorporates the Rybicki Method (Hubeny & Lanz, 2017). At lower temperatures the radiation pressure is small and LTE effects are stronger. The Rybicki Method is a numerical scheme that provides an intermediate model from which the full non-LTE model can be converged more easily. A detailed description of TLUSTY can be found in Hubeny & Lanz (2017).

To determine if the photometric excess for each object was real, I took T_{eff} , $\log g$ for each object from the literature (Table 6.1) as well as the magnitudes from SDSS and UKIDSS. I provided the DA white dwarf models created using TLUSTY to SYNSPEC. I selected a wavelength range of 900 - 50000 Å to coincide with my observational data, with a step size of 0.1 Å. For each object in Table 6.1, I generated a non-LTE model with TLUSTY (Lanz & Hubeny, 2003) and synthesised a spectrum with SYNSPEC using the method described in Chapter 3. I combined these models with brown dwarf template spectra from the NASA Infrared Telescope Facility (IRTF) spectral library¹. These are substellar spectra observed at a resolving power of $R = \frac{\lambda}{\delta\lambda} \sim 2000$ with the medium-resolution spectrograph, SpeX, at the NASA IRTF on Mauna Kea. All of the spectra have been absolutely flux calibrated using Two Micron All Sky Survey (2MASS) photometry. Table 6.3 lists all standards used in this work for each spectral type.

Making combined models

To combine a white dwarf model with a brown dwarf model I set them both to 10 pc. To do this I normalised both sets of models to their absolute H-band magnitudes. For the white dwarf models I obtained the expected H magnitudes from synthetic magnitudes² (Holberg & Bergeron 2006; Kowalski & Saumon 2006; Tremblay et al. 2011; Bergeron et al. 2011) and I have listed these in Table 6.4. For the brown dwarf standards, I used Table 16 from Dupuy & Liu (2012); I have listed

¹[http://irtfweb.ifa.hawaii.edu/spex/IRTF Spectral Library](http://irtfweb.ifa.hawaii.edu/spex/IRTF_Spectral_Library)

²<http://www.astro.umontreal.ca/bergeron/CoolingModels>

Spectral Type	Brown dwarf Standard	Absolute H magnitude	H band flux $\times 10^{-15}$ ($\text{ergs}^{-1}\text{cm}^{-2}\text{\AA}^{-1}$)	References
M6	2MASS J1354+2150	9.73	14.3	4
M7	2MASS J0917-1650	9.79	13.5	4
M8	2MASS J1045+1254	10.24	8.91	4
M9	LHS 2924	11.10	4.38	1
L0	2MASS J022+2537	10.99	4.47	3
L1	2MASS J2130-0845	11.22	3.75	4
L2	Kelu-1	11.40	3.18	2
L3	DENIS-P J1058-1548	11.92	1.97	5
L4	DENIS-P J1705-0516	12.11	1.59	5
L5	2MASS J0155+0950	12.59	1.06	5
L6	2MASS J2212+3430	12.98	0.741	5
L7	SDSS J1044+0429	13.64	0.389	5

Table 6.3: All brown dwarf standard spectra, of spectral types pertinent to this work, from the IRTF Spectral Library. The associated references are Burgasser & McElwain (2006)(1), (Burgasser et al., 2007)(2), Burgasser et al. (2008) (3), Kirkpatrick et al. (2010) (4), and Burgasser et al. (2010) (5). For each spectral type the H band flux was calculated from the mean 2MASS absolute magnitudes (Dupuy & Liu, 2012).

the calculated fluxes in Table 6.3. I normalised each combined model to the i band photometry of the respective system listed in Table 6.5.

6.4 Results & Discussion

When the excess is only photometric there is little other information with which to classify a potential companion. Unlike photometry, a spectrum provides more than just the magnitude within that wavelength band. By comparing these spectra to spectra of known brown dwarfs one can better classify the nature of the infrared excess. For each candidate system I have modelled the

Target SDSS J	H band Magnitude	H band Flux $\times 10^{-15}$ ($\text{ergs}^{-1}\text{cm}^{-2}\text{\AA}^{-1}$)
0751+2004	11.56	2.87
0907+0536	11.34	3.24
0950+0115	11.34	3.24
1003+0939	11.34	3.24
1010+0407	11.77	2.18
1015+0424	9.648	15.4
1016+0020	12.14	1.55
1037+0139	10.84	5.11

Table 6.4: The H band absolute magnitudes estimated from the T_{eff} and $\log g$ of each system and compared to Pierre Bergeron’s cooling models. I have also calculated the corresponding flux values in each case.

white dwarf and combined this with brown dwarf spectral templates; these were selected based on the previous photometric spectral type estimates. Through the combination of composite models, SDSS and UKIDSS photometry, and SDSS and GNIRS spectra I have classified the low mass companions to all eight white dwarf primaries. I have plotted the models and all the available data for each system in Figures 6.2 to 6.9. They each have a minimum of two composite models for comparison. I will discuss each system in turn.

SDSS J075132.52 +200216.94

Figure 6.2 shows the white dwarf model combined with three separate brown dwarf template spectra of type L2, 3, and 4. These models pass through all of the available photometry except for the J band which sits very slightly below all the composite models. this may be due to all models and spectra having been normalised to the i band for improved comparison. The SDSS and GNIRS spectra have been plotted in grey with the region $1.8 - 1.95\mu\text{m}$ removed due to low

	u	g	r	i	z	Y	J	H	K
Effective λ (\AA):	3595	4470	6122	7440	8897	10310	12350	16620	21590
0751+2004	17.7 \pm 0.01	17.7 \pm 0.01	18.1 \pm 0.01	18.3 \pm 0.01	18.5 \pm 0.04	18.2 \pm 0.03	18.2 \pm 0.04	17.8 \pm 0.07	17.6 \pm 0.10
0907+0536	18.3 \pm 0.01	18.2 \pm 0.01	18.5 \pm 0.01	18.8 \pm 0.01	19.1 \pm 0.04	18.8 \pm 0.05	18.7 \pm 0.08	18.6 \pm 0.20	18.4 \pm 0.20
0950+0115	17.9 \pm 0.01	17.8 \pm 0.01	18.2 \pm 0.01	18.5 \pm 0.01	18.8 \pm 0.04	18.5 \pm 0.04	18.5 \pm 0.06	18.2 \pm 0.10	-
1003+0939	18.9 \pm 0.02	18.9 \pm 0.01	19.3 \pm 0.02	19.6 \pm 0.03	20.0 \pm 0.10	19.3 \pm 0.08	19.2 \pm 0.10	18.5 \pm 0.20	18.5 \pm 0.20
1010+0407	18.6 \pm 0.02	18.3 \pm 0.01	18.5 \pm 0.01	18.8 \pm 0.01	19.1 \pm 0.04	18.7 \pm 0.04	-	18.2 \pm 0.20	-
1015+0425	17.4 \pm 0.01	17.6 \pm 0.01	18.1 \pm 0.01	18.5 \pm 0.01	18.8 \pm 0.04	18.5 \pm 0.04	18.6 \pm 0.05	18.4 \pm 0.20	18.2 \pm 0.20
1016+0020	18.7 \pm 0.02	18.7 \pm 0.01	18.9 \pm 0.01	19.3 \pm 0.02	19.4 \pm 0.07	19.4 \pm 0.13	-	18.7 \pm 0.20	-
1037+0139	18.5 \pm 0.02	18.3 \pm 0.01	18.6 \pm 0.01	18.8 \pm 0.01	18.7 \pm 0.04	18.3 \pm 0.04	17.8 \pm 0.03	17.3 \pm 0.06	17.1 \pm 0.07

Table 6.5: The SDSS ugriz and UKIDSS YJHK magnitudes, where available, for all eight candidate white dwarf - brown dwarf systems in this Chapter.

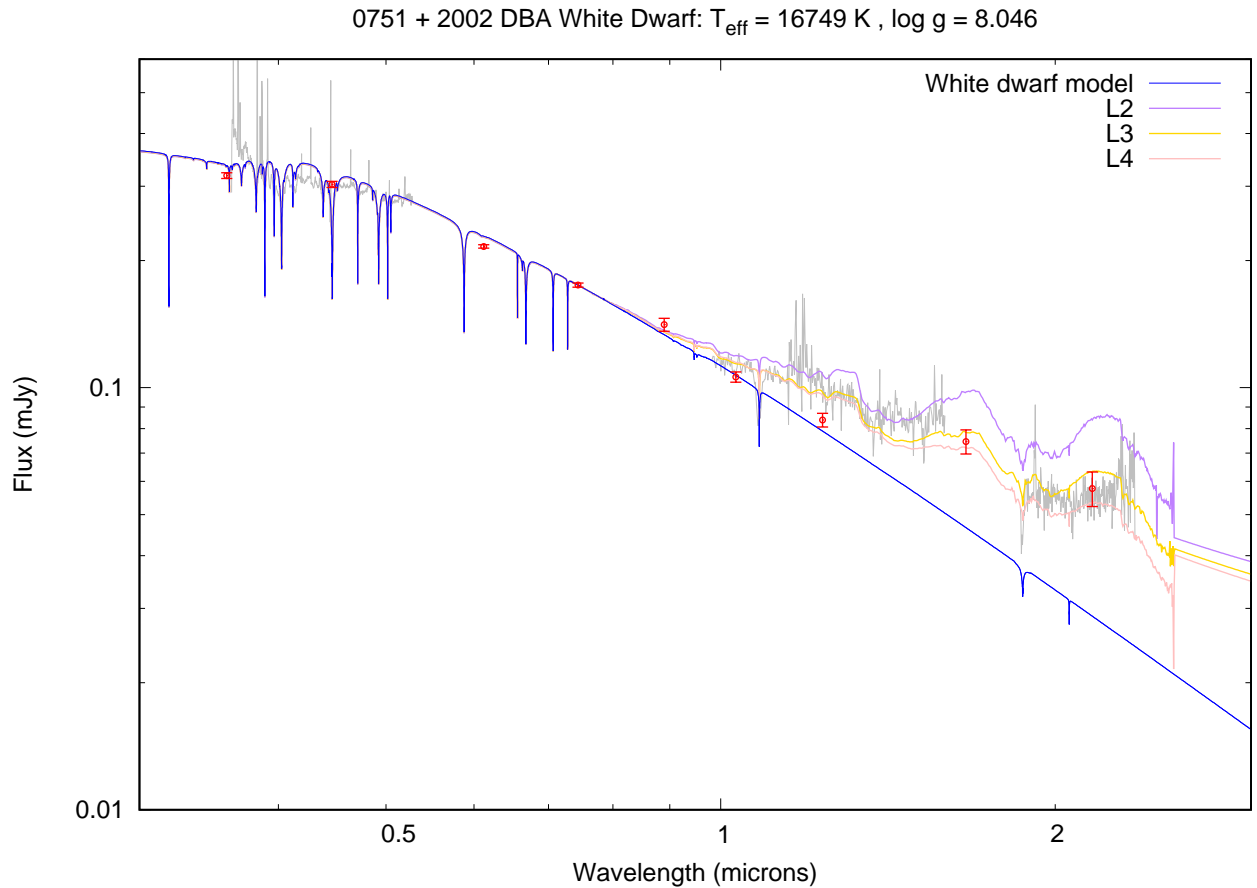


Figure 6.2: A DBA white dwarf model (blue) and composite white dwarf - brown dwarf models for three spectral types, L3 (purple), L4 (yellow), and L5 (pink). The observed photometry from SDSS and UKIDSS are plotted in red and the SDSS visible and GNIRS near-infrared spectra are plotted in grey.

signal-to-noise ratio even after optimised telluric correction. The spectra from $1.2 - 1.8 \mu\text{m}$ follows the shape and sits between the L2 and L3 models whereas the spectra longwards of $1.9 \mu\text{m}$ more sits between L3 and L4. Overall the spectrum broadly mirrors the shape of a early-mid L dwarf.

Kepler et al. (2015) classified the white in this system as a DAB meaning it has both H and He in its atmosphere. However, they do note that this classification is uncertain. It is possible that the H detected in this white dwarf is from accreted material from the brown dwarf companion in a similar fashion to NLTT5306 (Chapter 5). If this were to be the case then a much stronger limit could be placed on the accretion rate and therefore an empirical limit on wind substellar

0907 + 0536 DA White Dwarf: $T_{\text{eff}} = 19474 \text{ K}$, $\log g = 7.82$

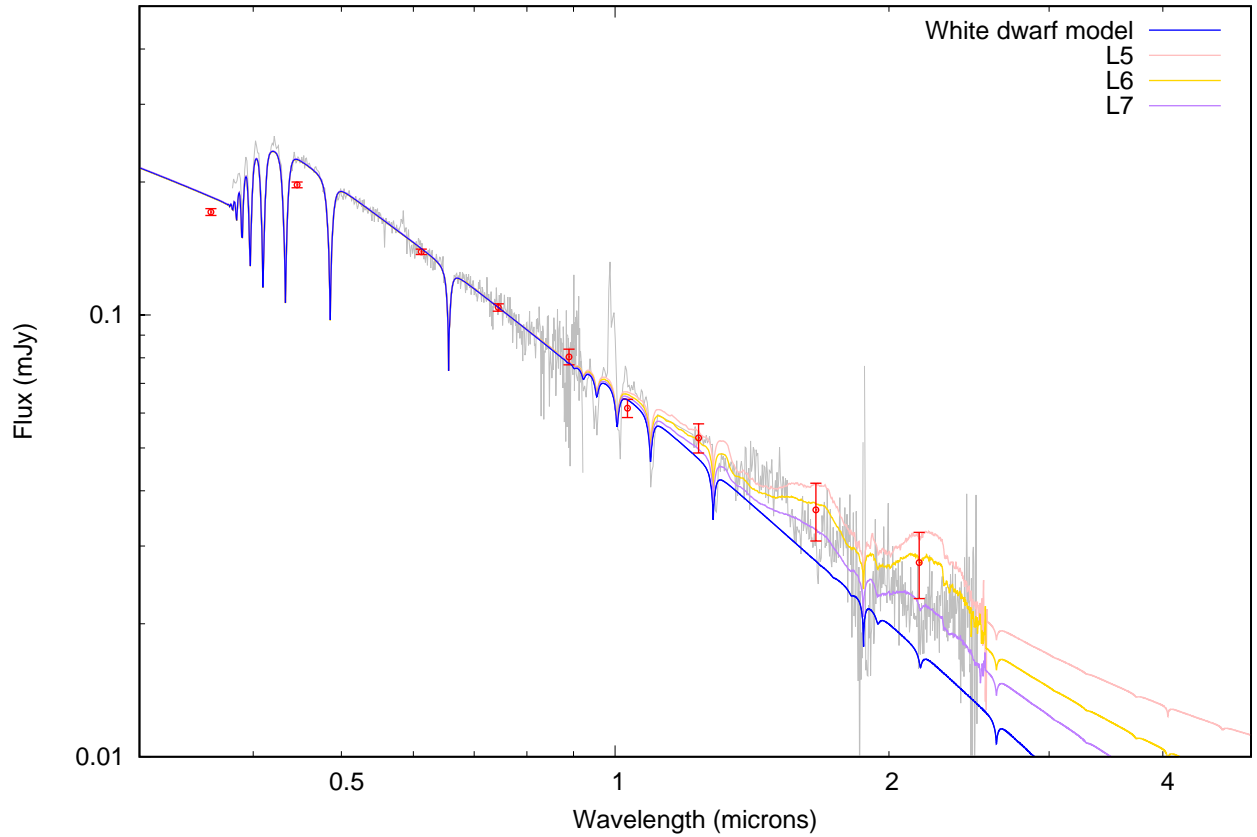


Figure 6.3: A DA white dwarf model (blue) and composite white dwarf - brown dwarf models for three spectral types, L5 (pink), L6 (yellow), and L7 (purple). The observed photometry from SDSS and UKIDSS are plotted in red and the SDSS visible and GNIRS near-infrared spectra are plotted in grey.

companions. Without knowledge of the separation of the two bodies and the orbital period of the system this cannot be tested.

SDSS J090759.59 +053638.13

Comparing the composite models of a white dwarf combined with L5, 6 and 7 brown dwarf templates to the spectra of SDSS J0907 +0536 indicates that the source of the infrared excess may not be from a low mass companion. This is particularly evident when looking at the K band

where the spectrum does not have the characteristic bump that is clear in the template spectra. This may be due to the low signal-to-noise ratio of the data. It is also difficult to interpret the near-infrared photometry due to the large error bars that span all three spectral templates. The combination of these traits means this object can not be confidently classified as a brown dwarf; the infrared excess may be due to a disk or cyclotron emission but without spectra longwards of $2.5\mu\text{m}$ this is hard to say for certain. A big factor in play here could be that the data only achieve a signal-to-noise ratio of 9 and one of the observing nights had poor seeing.

SDSS J095042.31 +011506.56

SDSS J0950+0115 has much less near-infrared photometry than other objects in this study which made gathering spectral data even more important in this case. The photometry in the Y and J bands sit considerably lower than the spectra this could be due to an error in the temperature estimate of the white dwarf, as the u and g band photometry are also lower, which could cause an under-estimate of the near-infrared excess. Alternatively, if the brown dwarf companion is close to the white dwarf the H band excess may be due to a reflection effect from intense irradiation. The three templates used in analysing this system were L3, 4, and 6 and are plotted in Figure 6.4 where it can be seen that that the spectrum broadly follows the shape of a mid-to-late L dwarf.

SDSS J100300.08 +093940.16

Figure 6.5 shows a white dwarf model combined with a M8 and an L0 brown dwarf template spectrum. The near-infrared photometry for this system tracks shape of the GNIRS spectrum and the Y, J, and K photometry align with the L0 template; the H band, however, is higher with only its lower uncertainty limit approaching the L0 template. The signal-to-noise of the GNIRS spectrum in the Y band was too low and has been removed. From the spectrometry in the H and K bands it is clear that SDSS J1003+0939 resembles an early L dwarf or a late M dwarf and the spectrum sits right in the middle of the two templates.

0950 + 0115 DA White Dwarf: $T_{\text{eff}} = 21785 \text{ K}$, $\log g = 7.89$

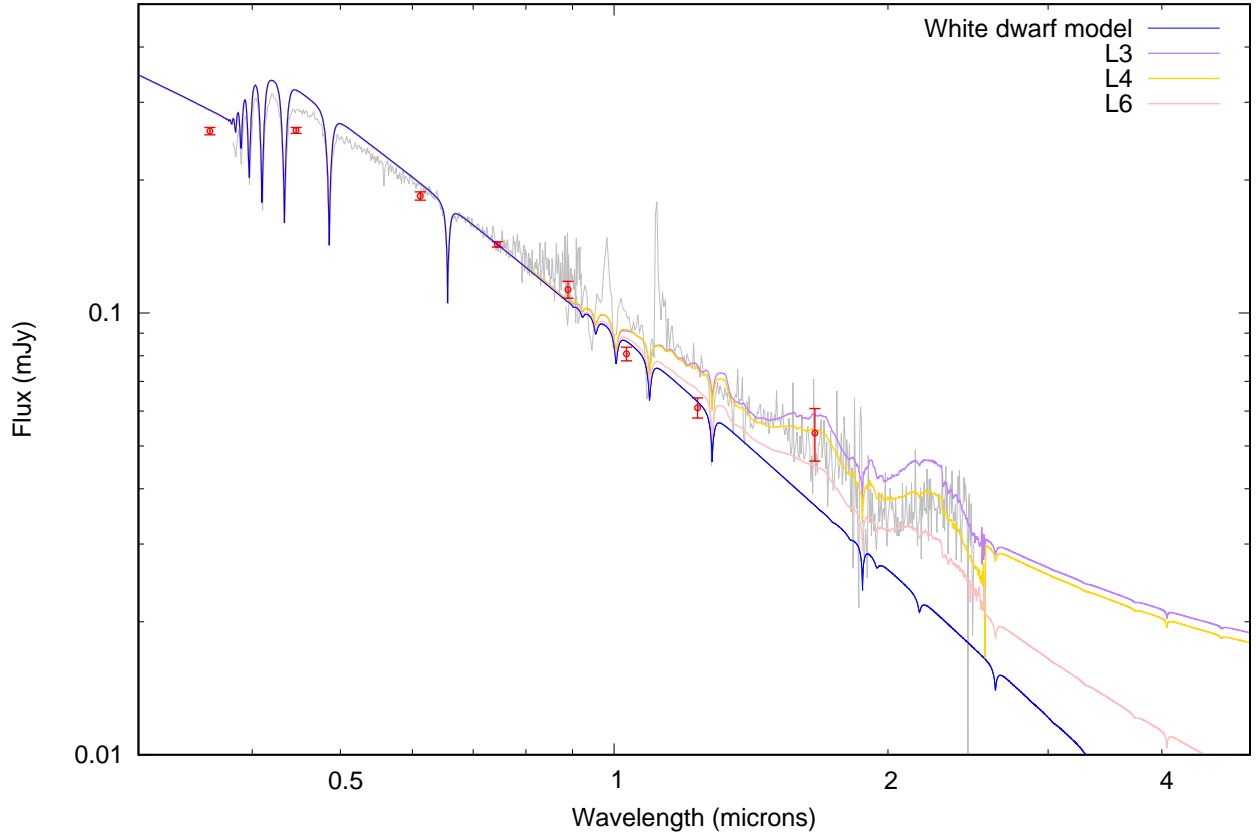


Figure 6.4: A DA white dwarf model (blue) and composite white dwarf - brown dwarf models for three spectral types, L3 (purple), L4 (yellow), and L6 (pink). The observed photometry from SDSS and UKIDSS are plotted in red and the SDSS visible and GNIRS near-infrared spectra are plotted in grey.

SDSS J101049.48 +040722.50

The model of the coolest white dwarf in this sample is plotted in Figure 6.6 combined with template spectra of L5, 6, and 7 brown dwarfs and all available optical and near-infrared photometry. Both the Y and J band photometry sit below the models and the spectra. The Y band is only slightly below and likely due to normalising the models and GNIRS spectra to the *i* band. The near-infrared spectra appear a lot flatter than the templates and whilst there is a slight hump in the H band there does not appear to be one in the K band. The shape of the near-infrared spectra does not look like the templates plotted in Figure 6.6 which suggests that this system may not

1003 + 0939 DA White Dwarf: $T_{\text{eff}} = 22331 \text{ K}$, $\log g = 7.87$

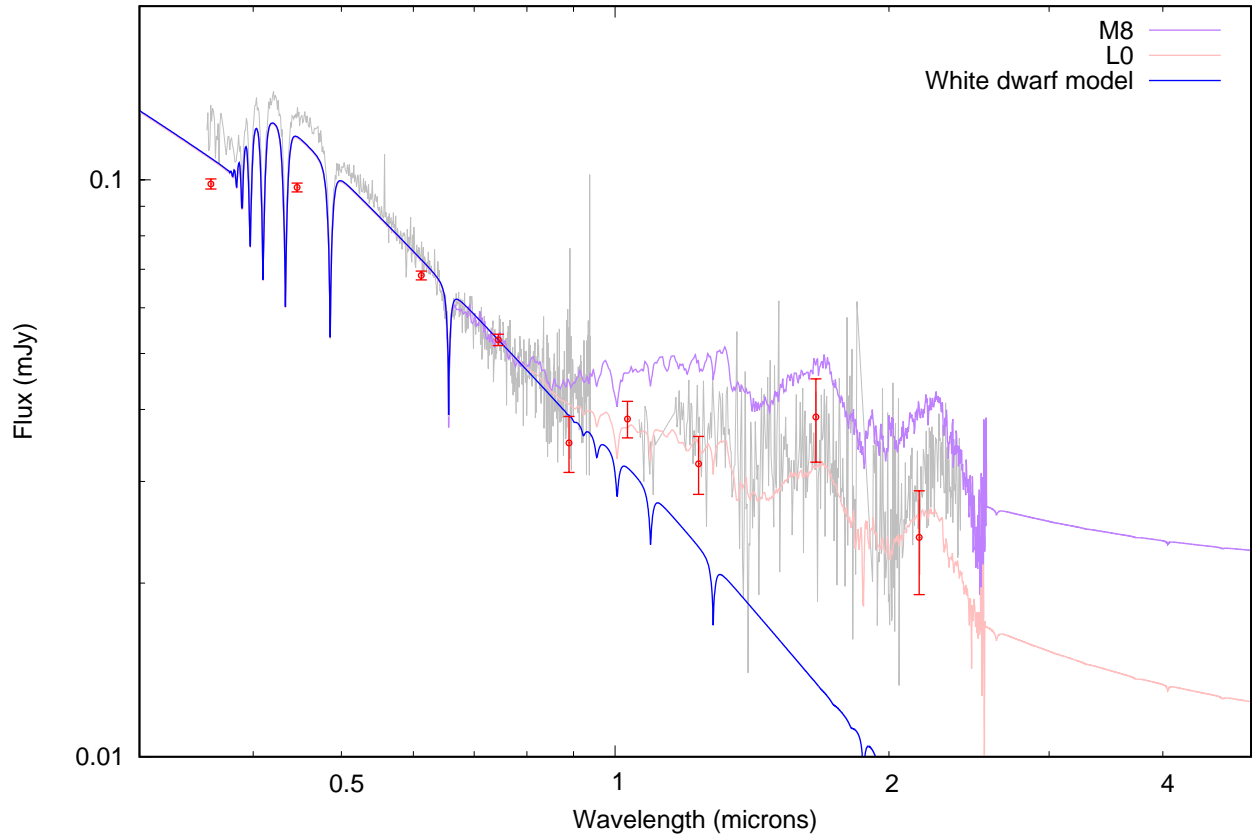


Figure 6.5: A DA white dwarf model (blue) and composite white dwarf - brown dwarf models for two spectral types, M8 (purple), and L0 (pink). The observed photometry from SDSS and UKIDSS are plotted in red and the SDSS visible and GNIRS near-infrared spectra are plotted in grey.

contain a low mass companion and the excess could be due to a disc. Having said that, the low mass of the white dwarf ($0.48 M_{\odot}$) suggests the white dwarf progenitor's evolution was truncated, which is indicative of a brown dwarf companion within \sim few AU from the white dwarf. SDSS J1010+0407 could be a close binary system similar to WD0137-349 and NLTT 5306 and could be verified with radial velocity measurements.

1010 + 0407 DA White Dwarf: $T_{\text{eff}} = 13588 \text{ K}$, $\log g = 7.76$

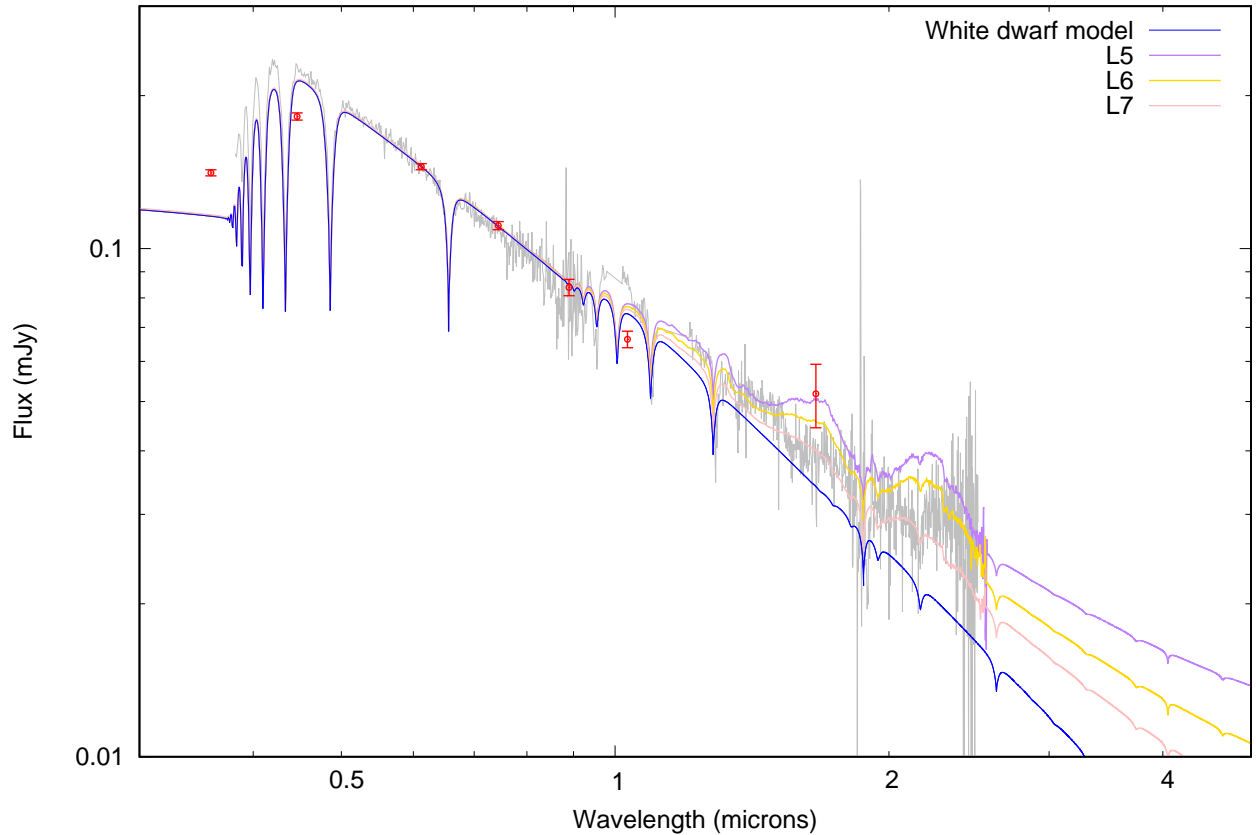


Figure 6.6: A DA white dwarf model (blue) and composite white dwarf - brown dwarf models for three spectral types, L5 (purple), L6 (yellow), and L7 (pink). The observed photometry from SDSS and UKIDSS are plotted in red and the SDSS visible and GNIRS near-infrared spectra are plotted in grey.

SDSS J101532.30 +042447.66

SDSS J1015+0424 is the hottest white dwarf in this sample it can be seen from Figure 6.7 that this produces a very steep white dwarf model. The optical photometry sits below the model suggesting a slight over estimate of the white dwarf temperature however the photometry aligns very well with the optical spectra. In the near-infrared the Y and J photometry do not appear to be above the white dwarf model however the H and K photometry sit significantly above and overlap with the measured spectra. The shape of the near-infrared spectra suggest it could be anything from a late M to mid L dwarf companion however the excess is so slight that it is impossible to

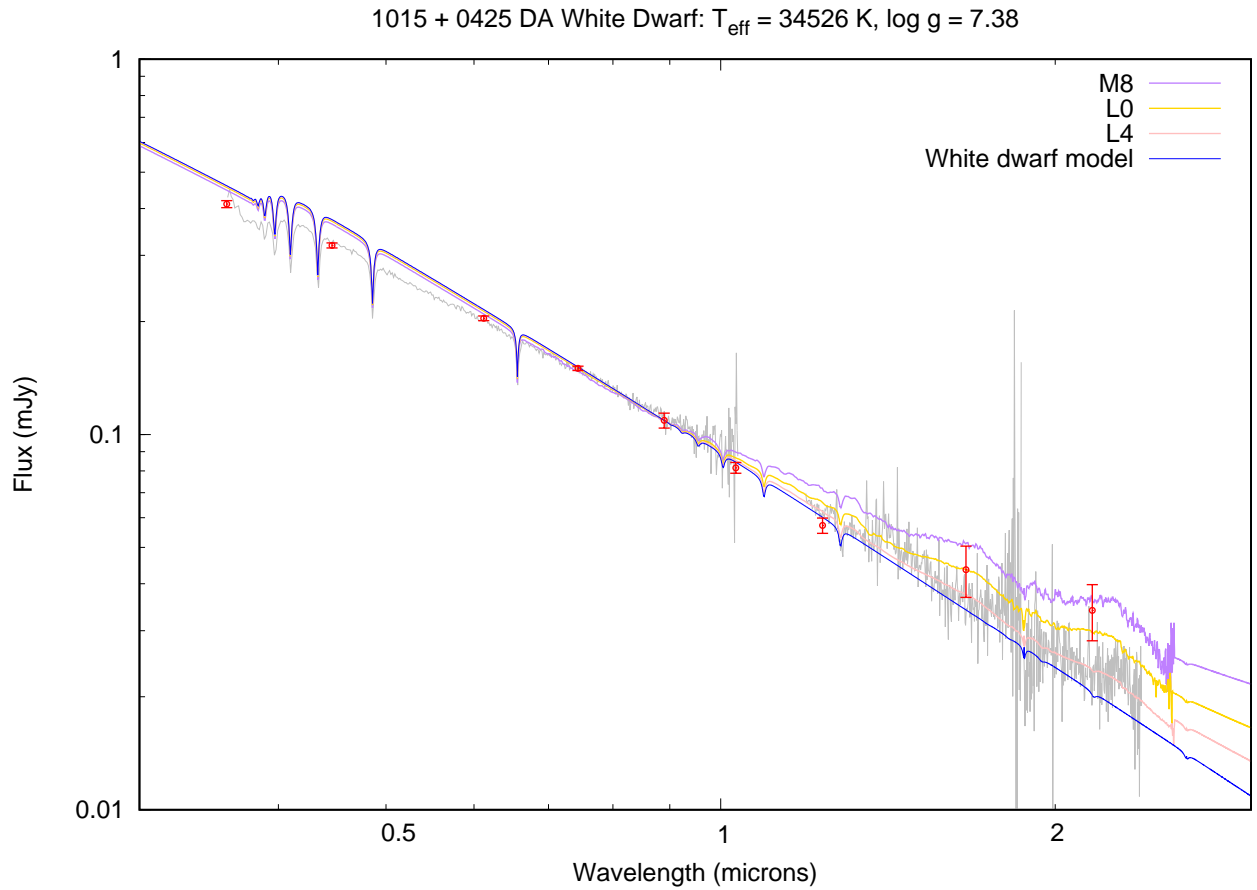


Figure 6.7: A DA white dwarf model (blue) and composite white dwarf - brown dwarf models for three spectral types, L5 (purple), L6 (yellow), and L7 (pink). The observed photometry from SDSS and UKIDSS are plotted in red and the SDSS visible and GNIRS near-infrared spectra are plotted in grey.

determine the nature of a potential companion purely from these data alone.

SDSS J101607.45 +002027.04

SDSS J1016+0020 GNIRS spectroscopy shows a clear infrared excess that lines up very well with the photometry. However the spectra appear to be quite shapeless especially in comparison to the L2, 3, and 4 brown dwarf templates. there is a hint of a bump in the K band but it is not strong enough for a robust conclusion to be dwarf on the spectral type of the potential companion in this

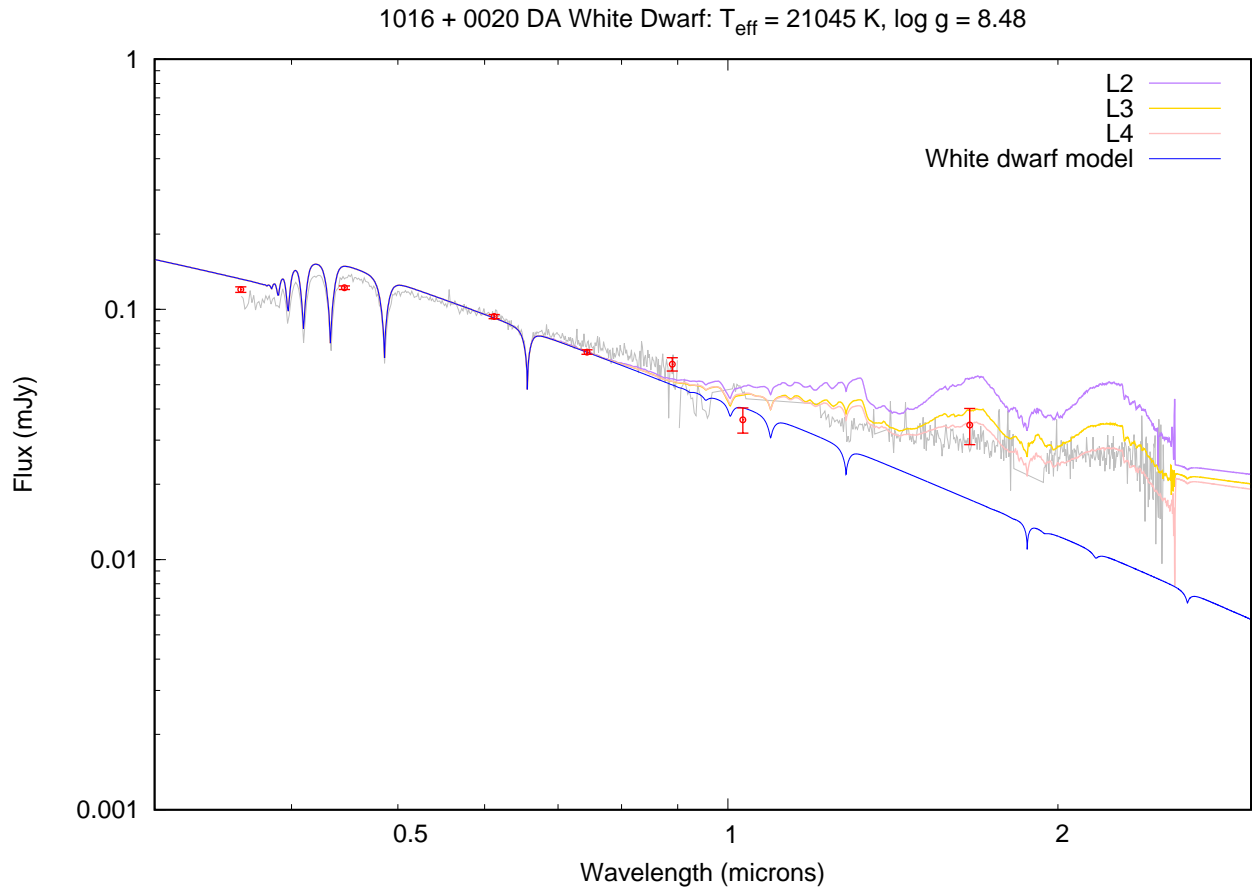


Figure 6.8: A DA white dwarf model (blue) and composite white dwarf - brown dwarf models for three spectral types, L2 (purple), L3 (yellow), and L4 (pink). The observed photometry from SDSS and UKIDSS are plotted in red and the SDSS visible and GNIRS near-infrared spectra are plotted in grey.

system. The Y band photometry sits below where one would expect it to be when looking at the z and H band photometry. However due to very poor signal-to-noise in the Y band it can't be seen whether the photometry would overlap with the spectroscopy.

SDSS J103736.57 +013905.11

SDSS J1037+0139 is the most clearly defined low mass companion. From Figure 6.9 it can be seen that the spectra and photometry align very well and the shape of the near-infrared spectrum

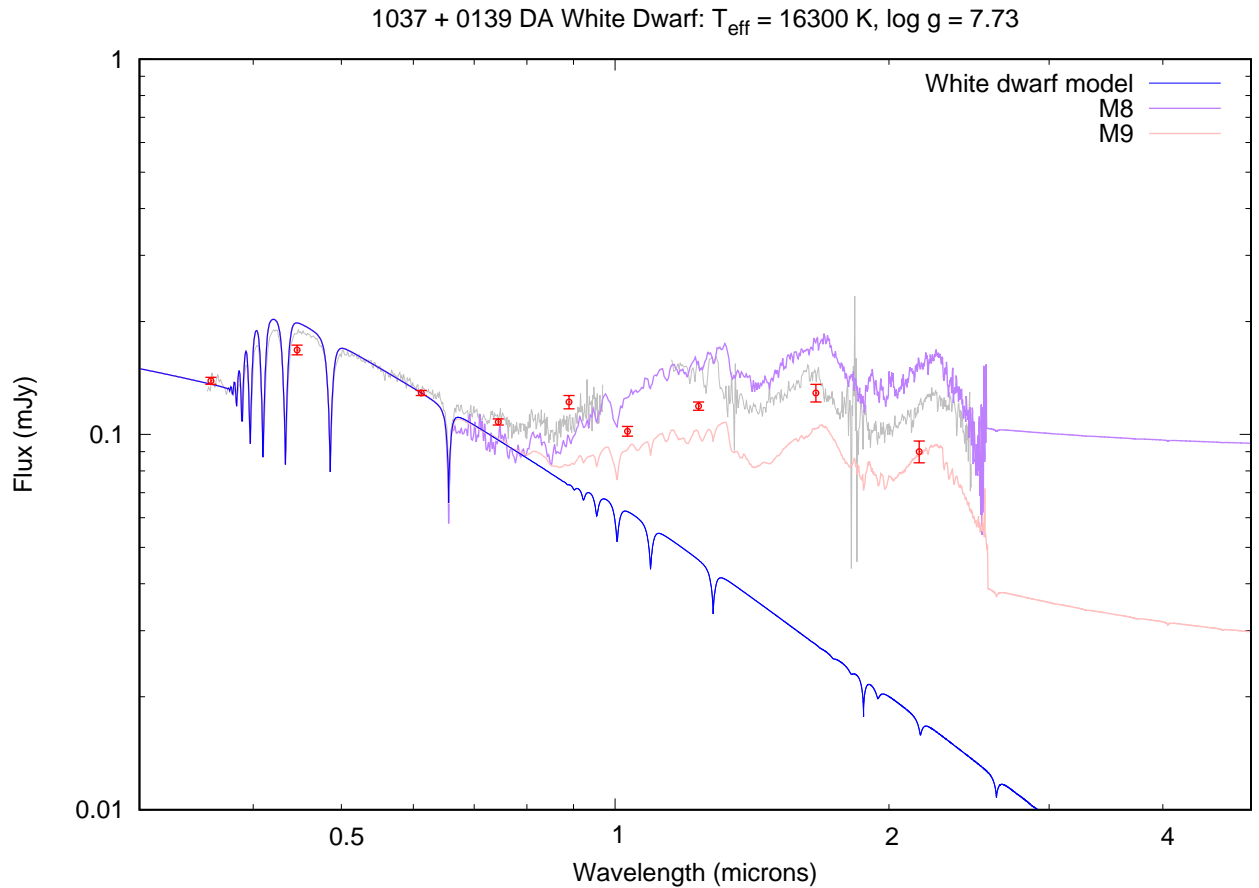


Figure 6.9: A DA white dwarf model (blue) and composite white dwarf - brown dwarf models for three spectral types, M8 (purple), and M9 (pink). The observed photometry from SDSS and UKIDSS are plotted in red and the SDSS visible and GNIRS near-infrared spectra are plotted in grey.

looks almost identical to that of a late type M dwarf. From inspection of the spectroscopy alone it would appear that an M8 spectral type would be most fitting however there is a drop in the K band photometry that sits almost exactly on the M9 spectral template. It is clear that this system contains a late type M dwarf.

This system has recently been found to have a short orbital period of ~ 6 hours making it an excellent candidate for empirically measuring the mass and radius of a fully convective late type M-dwarf. Constraining the radius will allow for better determination of the radii of exoplanets transiting other late type M-dwarfs, such as, Trappist-1 (Gillon et al., 2017).

6.5 Conclusion

The aim of this chapter was to discover and classify new white dwarf - brown dwarf binary systems. As has been discussed, many of the systems cannot be definitively classified with this work alone. Most of the spectra have signal-to-noise ratios of 10 or lower, two of which only achieved a signal-to-noise ratio of 5, thus making any classification uncertain. Unsurprisingly the better quality data provided the better classification estimates i.e. SDSS J1037 +0139 with a signal-to-noise ratio of 23.

In many cases the near-infrared spectra appear flat and featureless which could be a result of the large temperature difference between the white dwarf and the cool companion. The white dwarf, despite peaking in the blue, still contributes to the infrared and so discerning subtle brown dwarf-like spectral features becomes more difficult with hotter white dwarfs; this is particularly clear in SDSS J1015+0424. A better approach would have been to model and subtract the white dwarf from the near-infrared spectra and then compare the result to spectral templates.

Of the eight systems analysed in this work only three can be classified as definitely white dwarfs with low mass companions: SDSS J0950+0115, SDSS J1003+0939, and SDSS J1037+0139. The other five systems require further spectroscopic follow up to ensure that the observed infrared excess is due to a low mass companion. GNIRS spectra is capable of delivering this, however, a signal-to-noise ratio of at least 15 is necessary for robust future classification.

7

Conclusions

This chapter will review the work presented in this thesis. Chapter 1 individually describes white dwarf and brown dwarf formation and goes on to explain how white dwarf - brown dwarf binaries form through common envelope evolution. I have described all known close white dwarf - brown dwarf binaries both interacting and non-interacting. Chapter 2 introduced the instrumentation used to acquire spectroscopic and photometric data. Chapter 3 described the analysis techniques used in this work to reduce, analyse and model infrared, visible and ultraviolet spectroscopic data.

In the introduction I set out three main goals,

- To spectroscopically investigate the close white dwarf - brown dwarf binaries WD0137-349 and NLTT5306.

- To determine if these systems can be used as exoplanet analogues to inform future exoplanet atmospheric models.
- To spectroscopically confirm new white dwarf - brown dwarf binary systems.

I will discuss how well these aims have been achieved in the sections below.

7.1 Chapter 4: Emission lines in WD0137-349B

Investigation of WD0137-349 has shown that irradiated brown dwarfs can be used to inform future irradiated planet models. However, the differences between a brown dwarf and a gas giant exoplanet must always be kept in mind i.e. mass, density.

This chapter described the results of new XSHOOTER optical and near-infrared spectra of the 16 500 K white dwarf with a tidally locked brown dwarf companion. This system is a close, non-eclipsing, non-interacting binary with a period of ≈ 114 minutes. The substellar companion has a spectral type of L6 – L8, a temperature of $1300 < T_{\text{eff}} < 1400$ K, and a mass of $\sim 0.053 M_{\odot}$ and is therefore definitely in the brown dwarf regime.

7.1.1 Conclusions

I confirmed the presence of $H\alpha$ emission that was previously observed by Maxted et al. (2006) through radial velocity analysis. A key result of this work was my discovery of He, Na, Mg, Si, K, Ca, Ti, and Fe emission lines originating from the brown dwarf atmosphere.

Ch. Helling performed a preliminary test using a DRIFT-PHOENIX model. This model manipulated the temperature of the upper atmosphere to give an outward temperature increase; the result of which I analysed. This first test was to estimate what chemical one would expect at different gas temperatures. The elements I detected from my observational data and their ionisation states

broadly match the predictions of this model; which supports the possibility of a brown dwarf chromosphere being present.

I examined the equivalent widths of all emission lines and found a strong correlation between line strength and orbital phase suggesting that emission is not occurring on the non-irradiated side of the brown dwarf. This implies that heat redistribution around the brown dwarf is inefficient and emission is therefore a direct result of the intense irradiation from the white dwarf. The implications of this are that any future models of irradiated atmospheres - including hot Jupiters - will need to reproduce this line strength variation.

7.1.2 Future Work

The results from this Chapter will become important as the field of exo-atmospheres grows to a point where comparable observations can be made. This is not possible with the currently available observatories. Part of my investigation into WD0137-349 involved comparing the spectroscopic emission lines to that of a DRIFT-PHOENIX model of a brown dwarf upper atmosphere with an artificial temperature inversion. This comparison could be better performed with higher resolution spectra focused on the regions with known emission lines. From this abundances could be compared and potentially stratification of the upper brown dwarf atmosphere could be discerned.

7.2 Chapter 5: Possible accretion in NLTT5306

This system was less useful as an irradiated exoplanet analogue due to never directly detecting the brown dwarf. Despite this, NLTT 5306 is an interestingly unique system due to the evidence of accretion that contradicts the current understanding of when a system of this separation should begin interaction. Therefore NLTT 5306 would be a good candidate for mapping the transition from post common envelope binary to pre-CV.

This chapter looked at another close white dwarf - brown dwarf binary system. The white dwarf

is significantly cooler than WD0137-349 at 7756 K but the orbital separation and brown dwarf mass are very similar, 101 mins and $56 M_{\text{Jup}}$, respectively. Previous work by citetsteele13 found $H\alpha$ emission consistent with the white dwarf radial velocity solution suggesting it originates from the white dwarf surface. This lead Steele et al. (2013) to suggest accretion is occurring via Roche Lobe overflow. The spectra presented in Steele et al. (2013) also displays a triangular H-band which has been linked to low surface gravity of brown dwarfs.

I used XSHOOTER spectroscopy and *Swift* photometry to investigate this system further and determine the mechanism for accretion. The XSHOOTER spectra confirmed the $H\alpha$ emission to be in phase with the absorption and therefore originating from the white dwarf. I also detected Na I absorption lines coming from the white dwarf as well. My *Swift* observations covered the wavelength range 2030 - 2590 Å in three wavebands: uvw1, uvm2, uvw2; observations covered a full orbital period. XRT data were also taken simultaneously. If accretion were to be occurring one would expect high energy emission to be present.

7.2.1 Conclusions

$H\alpha$ emission and Na I absorption associated with the white dwarf indicate accretion is happening in NLTT5306. The X-ray non-detection allows for a lower limit to be placed on the accretion rate of $2 \times 10^{-15} M_{\odot} \text{yr}^{-1}$. Furthermore there is no observational evidence for an accretion disk which suggests accretion may be occurring magnetically, like a polar. This is supported by the phase-offset orbital variation of the $H\alpha$ emission line strength as this indicates a potential hot-spot on the white dwarf surface. However, the lack of any detectable typical evidence of accretion i.e. high energy emissions, Zeeman splitting, or cyclotron humps conflicts with this hypothesis.

The critical magnetic field required to prevent a disk forming from matter accreting at a rate of $2 \times 10^{-15} M_{\odot} \text{yr}^{-1}$ is very low at only, 0.45 kG. Coupling the low field required with the possibility that the triangular shape of the H–band does indeed indicate low surface gravity, then it may be possible for a wind to escape from NLTT5306B and there is scope for such a wind to be magnetically channelled through the bulk of the system. At the same time, the field and mass

transfer rate are too low to produce detectable Zeeman or cyclotron features.

7.2.2 Future Work

This system provides a lot of questions that need to be answered, most importantly: what is the mechanism of this accretion? The broad spectrum observations clearly indicate that a higher signal-to-noise is required. Systems with lower accretion rates than NLTT5306 do have X-ray detections (e.g. Farihi et al. 2018), thus observations using more sensitive observatories such as XMM-Newton are needed. Furthermore, magnetic fields weaker than 2 MG are only detectable for the highest S/N spectra therefore thorough circular spectro-polarimetry observations are required to verify a magnetic field.

7.3 Chapter 6: New white dwarf - brown dwarf systems

This chapter fulfils the third, and final, aim of this work: to spectroscopically identify and classify new white dwarf - brown dwarf systems.

This chapter investigates eight candidate white dwarf - brown dwarf systems. They were identified in previous surveys of white dwarfs with spectroscopic and/or photometric infrared excesses. To characterise these systems and determine their spectral type I reduced and analysed GNIRS spectra. In each case I used TLUSTY and SYNSPEC to model and synthesise white dwarf spectra based upon previous estimations of the white dwarfs effective temperature and surface gravity. I then created composite white dwarf + brown dwarf models of varying brown dwarf spectral type. I collected, SDSS optical spectra and photometry, and UKIDSS photometry to complement the new GNIRS spectra.

7.3.1 Conclusions

Of the 8 systems investigated only 3 could be definitively classified as having a brown dwarf companion: SDSS J0950+0115, SDSS J1003+0939, and SDSS J1037+0139. In many of the unclassified systems the near-infrared spectroscopy appeared flat and featureless making determining the cause of the infrared excess very difficult. It is possible that the infrared excess may be due to a disk or cyclotron emission however it is very hard to say anything with great certainty as most of the spectra have a signal-to-noise ratio less than 10 and two systems had less than 5.

SDSS J1037+0139 has been found to have an orbital period of ~ 6 hours. Currently models are relied upon to provide mass radius relations for late type M-dwarfs, however, these have been regularly found to underestimate the M dwarf radius by as much as 10 per cent for late spectral type. Further investigation into this system could yield an empirical measurement of the mass and radius of a late type M dwarf. This would directly benefit the characterisation of exoplanets around M-dwarfs due to transit surveys relying on precise knowledge of stellar host radii to determine the exoplanets radius and density.

7.3.2 Future Work

To categorically determine the nature of the other five systems higher quality spectral data is required. It is possible that the other five unclassified systems are indeed low mass companions and with better data their spectral type can be determined. GNIRS is capable of providing this but a signal-to-noise ratio of greater than 15 is necessary for robust classification.

For the three classified systems, the next step is to measure the white dwarf - brown dwarf separations. If any of them are close companions they would add to the currently very small list of such systems and thus populate the brown dwarf desert. To do this one would need to gain more, higher resolution, spectra (e.g. Xshooter spectra) and see if radial velocity can be measured; as was done for WD0137-349. If they are wider binaries then it may be possible to directly detect the brown dwarf in the near-to-mid infrared with, for example, James Webb Space Telescope. These

systems would be useful as benchmark brown dwarfs as their age could be well constrained via the white dwarf.

7.4 Summary

This thesis presents work on white dwarfs and brown dwarfs that exist in binary systems. White dwarfs are degenerate objects that are the final stage of stellar evolution and brown dwarfs are degenerate substellar objects whose atmospheres more closely resemble planets.

I have investigated two close white dwarf - brown dwarf binaries that, whilst very similar in orbital separation and component masses, display very different observational characteristics. The first of the two systems allowed me to thoroughly investigate how irradiation affects a planet-like atmosphere and the results will influence future models of irradiated, tidally locked companions. The latter system allowed me to probe the potential for a wind from a substellar companion onto its white dwarf primary. If further observations categorically prove that this system is accreting via magnetic funnelling of a brown dwarf wind it will be the first substellar wind to be detected and characterised. These close non-interacting white dwarf - brown dwarf binaries are very rare, only 10 have been confirmed so far. My final work has been to confirm 3 more white dwarf - brown dwarf systems whose orbital separations need to be determined to see if they exist in the brown dwarf desert. Given that WD0137-349 and NLTT 5306 have extremely similar physical parameters, i.e. component masses, radii, orbital separations, but they display very different observable characteristics; I would not want to say that one could predict the behaviour of a close white dwarf - brown dwarf system based purely on physical parameters. It would appear that, if all things are equal, temperature plays a very big part in determining the observable behaviour of irradiated brown dwarf companions. It would be interesting to compare physically similar systems across a range of temperatures.

Finally, the main conclusion of this work is that brown dwarf companions to white dwarf stars can be exceptionally useful tools for understanding exoplanet atmospheres. They provide insight into

binary evolution and understanding the many ways a post-common envelope binary can transition into a cataclysmic variable (i.e. Roche lobe over flow, magnetic field interaction). The main difficulty with this work is the small number of such systems currently detected. Increasing this number and understanding why it is so small in the first place is vital for the future of brown dwarf research.

Bibliography

- Abt H. A., Levy S. G., 1976, *ApJS*, 30, 273
- Ackerman A. S., Marley M. S., 2001, *ApJ*, 556, 872
- Allard F., Hauschildt P. H., Alexander D. R., Tamanai A., Schweitzer A., 2001, *ApJ*, 556, 357
- Allers K. N., Liu M. C., 2013, *ApJ*, 772, 79
- Apai D., Radigan J., Buenzli E., Burrows A., Reid I. N., Jayawardhana R., 2013, *ApJ*, 768, 121
- Bailey J., Ferrario L., Wickramasinghe D., 1991, *Monthly Notices of the Royal Astronomical Society*, 251, 37P
- Baraffe I., Chabrier G., Allard F., Hauschildt P. H., 2002, *A&A*, 382, 563
- Barman T. S., Hauschildt P. H., Allard F., 2004, *ApJ*, 614, 338
- Barthelmy S. D., Swift/BAT Instrument Team 2004, in *American Astronomical Society Meeting Abstracts Vol. 36 of Bulletin of the American Astronomical Society, The Swift-BAT Instrument – Initial On-Orbit Performance*. p. 1611
- Basri G., 1998, in *Rebolo R., Martin E. L., Zapatero Osorio M. R., eds, Brown Dwarfs and Extrasolar Planets Vol. 134 of Astronomical Society of the Pacific Conference Series, The Lithium Test for Young Brown Dwarfs (invited review)*. p. 394
- Beatty T. G., et al., 2014, *ApJ*, 783, 112

Beccari G., Carraro G., 2015, *Introduction to the Theory of Stellar Evolution*. p. 1

Beers T. C., et al., 1992, *AJ*, 103, 267

Bergeron P., Wesemael F., Dufour P., Beauchamp A., Hunter C., Saffer R. A., Gianninas A., Ruiz M. T., Limoges M.-M., Dufour P., Fontaine G., Liebert J., 2011, *ApJ*, 737, 28

Bergeron P., Wesemael F., Fontaine G., 1992, *ApJ*, 387, 288

Beuermann K., et al., 2013, *A&A*, 558, A96

Beuermann K., Wheatley P., Ramsay G., Euchner F., Gänsicke B. T., 2000, *A&A*, 354, L49

Bildsten L., Chakrabarty D., 2001, *ApJ*, 557, 292

Bilger C., Rimmer P., Helling C., 2013, *MNRAS*, 435, 1888

Bois B., Mochnacki S. W., Lanning H. H., 1991, *AJ*, 102, 2079

Breedt E., Gänsicke B. T., Girven J., Drake A. J., Copperwheat C. M., Parsons S. G., Marsh T. R., 2012, *MNRAS*, 423, 1437

Brinkworth C. S., Gänsicke B. T., Marsh T. R., Hoard D. W., Tappert C., 2009, *ApJ*, 696, 1402

Burgasser A. J., Cruz K. L., Cushing M., Gelino C. R., Looper D. L., Faherty J. K., Kirkpatrick J. D., Reid I. N., 2010, *ApJ*, 710, 1142

Burgasser A. J., Liu M. C., Ireland M. J., Cruz K. L., Dupuy T. J., 2008, *ApJ*, 681, 579

Burgasser A. J., McElwain M. W., 2006, *AJ*, 131, 1007

Burgasser A. J., Reid I. N., Siegler N., Close L., Allen P., Lowrance P., Gizis J., 2007, *Protostars and Planets V*, pp 427–441

Burgasser A. J., Sitarski B. N., Gelino C. R., Logsdon S. E., Perrin M. D., 2011, *ApJ*, 739, 49

Burleigh M. R., et al., 2006, *MNRAS*, 373, L55

- Burleigh M. R., et al., 2011, in Schuh S., Drechsel H., Heber U., eds, American Institute of Physics Conference Series Vol. 1331 of American Institute of Physics Conference Series, Brown Dwarf Companions to White Dwarfs. pp 262–270
- Burrows A., Hubbard W. B., Lunine J. I., Liebert J., 2001, *Reviews of Modern Physics*, 73, 719
- Burrows A., Marley M., et al., 1997, *ApJ*, 491, 856
- Burrows A., Sudarsky D., Lunine J. I., 2003, *ApJ*, 596, 587
- Burrows D. N., Hill J. E., Nousek J. A., Kennea J. A., Wells A., Osborne J. P., Abbey A. F., Beardmore A., Mukerjee K., Short A. D. T., Chincarini G., Campana S., Citterio O., Moretti A., et al., 2005, *Space Science Rev.*, 120, 165
- Carroll B. W., Ostlie D. A., 1996, *An Introduction to Modern Astrophysics*
- Casewell S. L., Braker I. P., Parsons S. G., Hermes J. J., Burleigh M. R., Belardi C., Chaushev A., Finch N. L., Roy M., Littlefair S. P., Goad M., Dennihy E., 2018, *MNRAS*, 476, 1405
- Casewell S. L., et al., 2012, *ApJL*, 759, L34
- Casewell S. L., et al., 2015, *MNRAS*, 447, 3218
- Chabrier G., Baraffe I., Allard F., Hauschildt P., 2000, *ApJL*, 542, L119
- Chabrier G., Johansen A., Janson M., Rafikov R., 2014, *Protostars and Planets VI*, pp 619–642
- Chandrasekhar S., 1931, *ApJ*, 74, 81
- Chandrasekhar S., 1935, *MNRAS*, 95, 207
- Cheng F. H., Sion E. M., Szkody P., Huang M., 1997, *ApJL*, 484, L149
- Ciardi D. R., Howell S. B., Hauschildt P. H., Allard F., 1998, *ApJ*, 504, 450
- Cooper C. S., Sudarsky D., Milsom J. A., Lunine J. I., Burrows A., 2003, *ApJ*, 586, 1320
- Cox J. P., 1980, *Sky & Telescope*, 60, 418
- Cushing M. C., et al., 2011, *ApJ*, 743, 50

Cushing M. C., Marley M. S., Saumon D., Kelly B. C., Vacca W. D., Rayner J. T., Freedman R. S., Lodders K., Roellig T. L., 2008, ApJ, 678, 1372

Cushing M. C., Rayner J. T., Vacca W. D., 2005, ApJ, 623, 1115

Cushing M. C., Vacca W. D., Rayner J. T., 2004, PASP, 116, 362

Dantona F., Mazzitelli I., 1985, ApJ, 296, 502

Debes J. H., 2006, ApJ, 652, 636

Debes J. H., Hoard D. W., Wachter S., Leisawitz D. T., Cohen M., 2011, ApJS, 197, 38

Debes J. H., López-Morales M., Bonanos A. Z., Weinberger A. J., 2006, ApJL, 647, L147

Dieterich S. B., Henry T. J., Jao W.-C., Winters J. G., Hosey A. D., Riedel A. R., Subasavage J. P., 2014, AJ, 147, 94

Dobbie P. D., et al., 2005, A&A, 439, 1159

Dupuy T. J., Liu M. C., 2012, ApJS, 201, 19

Eggleton P. P., 1983, ApJ, 268, 368

Eisenstein D. J., et al., 2006, ApJS, 167, 40

Evans P. A., Beardmore A. P., Page K. L., Osborne J. P., O'Brien P. T., Willingale R., Starling R. L. C., Burrows D. N., Godet O., Vetere L., Racusin J., et al., 2009, MNRAS, 397, 1177

Evans P. A., Beardmore A. P., Page K. L., Tyler L. G., Osborne J. P., Goad M. R., O'Brien P. T., Vetere L., Racusin J., Morris D., Burrows D. N., Capalbi M., Perri M., Gehrels N., Romano P., 2007, A&A, 469, 379

Faherty J. K., Rice E. L., Cruz K. L., Mamajek E. E., Núñez A., 2013, AJ, 145, 2

Farihi J., Burleigh M., Hoard D., 2008, The Astrophysical Journal, 674, 421

Farihi J., Christopher M., 2004, AJ, 128, 1868

Farihi J., Fossati L., Wheatley P. J., Metzger B. D., Mauerhan J., Bachman S., Gänsicke B. T., Redfield S., Cauley P. W., Kochukhov O., Achilleos N., Stone N., 2018, *MNRAS*, 474, 947

Farihi J., Gänsicke B. T., Steele P. R., Girven J., Burleigh M. R., Breedt E., Koester D., 2012, *MNRAS*, 421, 1635

Farihi J., Parsons S. G., Gänsicke B. T., 2017, *Nature Astronomy*, 1, 0032

Fontaine G., Brassard P., Bergeron P., 2001, *PASP*, 113, 409

Frank J., King A., Raine D. J., 2002, *Accretion Power in Astrophysics: Third Edition*

Fuhrmeister B., Schmitt J. H. M. M., Hauschildt P. H., 2005, *A&A*, 439, 1137

Gaia Collaboration Brown A. G. A., Vallenari A., Prusti T., de Bruijne J. H. J., Babusiaux C., Bailer-Jones C. A. L., 2018, *ArXiv e-prints*

Gaia Collaboration Prusti T., de Bruijne J. H. J., Brown A. G. A., Vallenari A., Babusiaux C., Bailer-Jones C. A. L., Bastian U., Biermann M., Evans D. W., et al. 2016, *A&A*, 595, A1

Gänsicke B. T., Marsh T. R., Southworth J., Rebassa-Mansergas A., 2006, *Science*, 314, 1908

Gentile Fusillo N. P., Girven J., Gänsicke B., 2013, in 18th European White Dwarf Workshop. Vol. 469 of *Astronomical Society of the Pacific Conference Series*, *White Dwarfs in the SDSS Photometric Footprint*. p. 217

Gillon M., Triaud A. H. M. J., Demory B.-O., Jehin E., Agol E., Deck K. M., Lederer S. M., de Wit J., Burdanov A., Ingalls J. G., Bolmont E., Leconte J., Raymond S. N., Selsis F., Turbet M., Barkaoui K., Burgasser A., et al., 2017, *Nature*, 542, 456

Girven J., Gänsicke B. T., Steeghs D., Koester D., 2011, *MNRAS*, 417, 1210

Greenstein J. L., ed. 1960, *Stellar atmospheres*.

Grether D., Lineweaver C. H., 2007, *ApJ*, 669, 1220

Hansen C. J., Kawaler S. D., 1994, *Stellar Interiors. Physical Principles, Structure, and Evolution*.

Harrison T. E., 2016, *ApJ*, 816, 4

Harrison T. E., Hamilton R. T., Tappert C., Hoffman D. I., Campbell R. K., 2013, *AJ*, 145, 19

Hayashi C., Nakano T., 1963, *Progress of Theoretical Physics*, 30, 460

Helling C., Casewell S., 2014, *A&AR*, 22, 80

Helling C., Lee G., Dobbs-Dixon I., Mayne N., Amundsen D. S., Khaimova J., Unger A. A., Manners J., Acreman D., Smith C., 2016, *MNRAS*, 460, 855

Hernández Santisteban J. V., Knigge C., Littlefair S. P., Breton R. P., Dhillon V. S., Gänsicke B. T., Marsh T. R., Pretorius M. L., Southworth J., Hauschildt P. H., 2016, *Nature*, 533, 366

Holberg J. B., Bergeron P., 2006, *AJ*, 132, 1221

Hubeny I., Lanz T., 1995, in Koester D., Werner K., eds, *White Dwarfs Vol. 443 of Lecture Notes in Physics*, Berlin Springer Verlag, Non-LTE Line Blanketed Model Atmospheres of Hot, Metal-Rich White Dwarfs. p. 98

Hubeny I., Lanz T., , 2011, *Synspec: General Spectrum Synthesis Program*, Astrophysics Source Code Library

Hubeny I., Lanz T., 2017, ArXiv e-prints

Iben Jr. I., Livio M., 1993, *PASP*, 105, 1373

Iben Jr. I., Renzini A., 1983, *ARA&A*, 21, 271

Izzo C., Kornweibel N., McKay D., Palsa R., Peron M., Taylor M., 2004, *The Messenger*, 117, 33

Kawka A., Vennes S., Dupuis J., Chayer P., Lanz T., 2008, *ApJ*, 675, 1518

Kepler S. O., Pelisoli I., Koester D., Ourique G., Kleinman S. J., Romero A. D., Nitta A., Eisenstein D. J., Costa J. E. S., Külebi B., Jordan S., Dufour P., Giommi P., Rebassa-Mansergas A., 2015, in Dufour P., Bergeron P., Fontaine G., eds, *19th European Workshop on White Dwarfs Vol. 493 of Astronomical Society of the Pacific Conference Series*, New White Dwarfs in the SDSS DR10. p. 449

- Kepler S. O., Pelisoli I., Koester D., Ourique G., Romero A. D., Reindl N., Kleinman S. J., Eisenstein D. J., Valois A. D. M., Amaral L. A., 2016, *VizieR Online Data Catalog*, 745
- Kilic M., von Hippel T., Leggett S. K., Winget D. E., 2006, *ApJ*, 646, 474
- King A. R., 1985, in Burke W. R., ed., *Recent Results on Cataclysmic Variables. The Importance of IUE and Exosat Results on Cataclysmic Variables and Low-Mass X-Ray Binaries Vol. 236 of ESA Special Publication, Accretion processes in the magnetic cataclysmic variables*
- Kirkpatrick J. D., Barman T. S., Burgasser A. J., McGovern M. R., McLean I. S., Tinney C. G., Lowrance P. J., 2006, *ApJ*, 639, 1120
- Kirkpatrick J. D., Looper D. L., Burgasser A. J., Schurr S. D., Cutri R. M., Cushing M. C., Cruz K. L., Sweet A. C., Knapp G. R., Barman T. S., Bochanski J. J., Roellig T. L., McLean I. S., McGovern M. R., Rice E. L., 2010, *ApJS*, 190, 100
- Kirkpatrick J. D., Reid I. N., Liebert J., Cutri R. M., Nelson B., Beichman C. A., Dahn C. C., Monet D. G., Gizis J. E., Skrutskie M. F., 1999, *ApJ*, 519, 802
- Kleinman S. J., Eisenstein D. J., Liebert J., Harris H. C., 2007, in Napiwotzki R., Burleigh M. R., eds, *15th European Workshop on White Dwarfs Vol. 372 of Astronomical Society of the Pacific Conference Series, The SDSS DR4 White Dwarf Catalog*. p. 121
- Koen C., Maxted P. F. L., 2006, *MNRAS*, 371, 1675
- Koester D., 2010, *Mem. S.A.It.*, 81, 921
- Konopacky Q. M., Barman T. S., Macintosh B. A., Marois C., 2013, *Science*, 339, 1398
- Kowalski P. M., Saumon D., 2006, *ApJL*, 651, L137
- Kreidberg L., Bean J. L., Désert J.-M., Line M. R., Fortney J. J., Madhusudhan N., Stevenson K. B., Showman A. P., Charbonneau D., McCullough P. R., Seager S., Burrows A., Henry G. W., Williamson M., Kataria T., Homeier D., 2014, *ApJL*, 793, L27
- Kroupa P., 2001, *MNRAS*, 322, 231

- Külebi B., Jordan S., Euchner F., Gänsicke B. T., Hirsch H., 2009, *A&A*, 506, 1341
- Kumar S. S., 1963, *ApJ*, 137, 1121
- Lanz T., Hubeny I., 2003, in Hubeny I., Mihalas D., Werner K., eds, *Stellar Atmosphere Modeling* Vol. 288 of *Astronomical Society of the Pacific Conference Series*, *Atomic Data in Non-LTE Model Stellar Atmospheres*. p. 117
- Lawrence A., Warren S. J., Almaini O., Edge A. C., Hambly N. C., Jameson R. F., Lucas P., Casali M., Adamson A., Dye S., Emerson J. P., Foucaud S., Hewett P., Hirst P., Hodgkin S. T., Irwin M. J., Lodieu N., McMahon R. G., et al., 2007, *MNRAS*, 379, 1599
- Lee G., Dobbs-Dixon I., Helling C., Bognar K., Woitke P., 2016, *A&A*, 594, A48
- Lee G., Helling C., Dobbs-Dixon I., Juncher D., 2015, *A&A*, 580, A12
- Littlefair S. P., Casewell S. L., Parsons S. G., Dhillon V. S., Marsh T. R., Gänsicke B. T., Bloemen S., Catalan S., Irawati P., Hardy L. K., Mcallister M., Bours M. C. P., Richichi A., Burleigh M. R., Burningham B., Breedt E., Kerry P., 2014, *MNRAS*, 445, 2106
- Littlefair S. P., Dhillon V. S., Marsh T. R., Gänsicke B. T., Baraffe I., Watson C. A., 2007, *MNRAS*, 381, 827
- Littlefair S. P., Dhillon V. S., Marsh T. R., Gänsicke B. T., Southworth J., Baraffe I., Watson C. A., Copperwheat C., 2008, *MNRAS*, 388, 1582
- Littlefair S. P., Dhillon V. S., Marsh T. R., Gänsicke B. T., Southworth J., Watson C. A., 2006, *Science*, 314, 1578
- Littlefair S. P., Savoury C. D. J., Dhillon V. S., Marsh T. R., Gänsicke B. T., Butterley T., Wilson R. W., Southworth J., Watson C. A., 2013, *MNRAS*, 431, 2820
- Longstaff E. S., Casewell S. L., Wynn G. A., Maxted P. F. L., Helling C., 2017, *MNRAS*, 471, 1728
- Luhman K. L., Joergens V., Lada C., Muzerolle J., Pascucci I., White R., 2007, *Protostars and Planets V*, pp 443–457

Luri X., Brown A. G. A., Sarro L. M., Arenou F., Bailer-Jones C. A. L., Castro-Ginard A., de Bruijne J., Prusti T., Babusiaux C., Delgado H. E., 2018, ArXiv e-prints

Luyten W. J., 1952, ApJ, 116, 283

Marley M. S., Saumon D., Goldblatt C., 2010, ApJL, 723, L117

Martín E. L., Basri G., Zapatero Osorio M. R., 1999, AJ, 118, 1005

Maxted P. F. L., et al., 2006, Nature, 442, 543

Maxted P. F. L., Marsh T. R., Moran C., Dhillon V. S., Hilditch R. W., 1998, MNRAS, 300, 1225

McAllister M. J., Littlefair S. P., Dhillon V. S., Marsh T. R., Gänsicke B. T., Bochinski J., Bours M. C. P., Breedt E., Hardy L. K., Hermes J. J., Kengkriangkrai S., Kerry P., Parsons S. G., Rattanasoon S., 2017, MNRAS, 467, 1024

McCook G. P., Sion E. M., 1999, VizieR Online Data Catalog, 3210, 0

Metchev S. A., 2006, PhD thesis, California Institute of Technology, California, USA

Meyer F., Meyer-Hofmeister E., 1979, A&A, 78, 167

Morley C. V., Marley M. S., Fortney J. J., Lupu R., Saumon D., Greene T., Lodders K., 2014, ApJ, 787, 78

Napiwotzki R., Christlieb N., Drechsel H., Hagen H.-J., Heber U., Homeier D., Karl C., Koester D., Leibundgut B., Marsh T. R., Moehler S., Nelemans G., Pauli E.-M., Reimers D., Renzini A., Yungelson L., 2001, Astronomische Nachrichten, 322, 411

Oppenheimer B. R., Kulkarni S. R., Matthews K., van Kerkwijk M. H., 1998, ApJ, 502, 932

Parsons S. G., Hermes J. J., Marsh T. R., Gänsicke B. T., Tremblay P.-E., Littlefair S. P., Sahman D. I., Ashley R. P., Green M., Rattanasoon S., Dhillon V. S., Burleigh M. R., Casewell S. L., Buckley D. A. H., Braker I. P., Irawati P., et al., 2017, MNRAS, 471, 976

Parsons S. G., Marsh T. R., Copperwheat C. M., Dhillon V. S., Littlefair S. P., Gänsicke B. T., Hickman R., 2010, MNRAS, 402, 2591

Patterson J., Richman H., Kemp J., Mukai K., 1998, PASP, 110, 403

Perna R., Heng K., Pont F., 2012, ApJ, 751, 59

Pineda J. S., Hallinan G., Kirkpatrick J. D., Cotter G., Kao M. M., Mooley K., 2016, ApJ, 826, 73

Preston G. W., et al., 1991, ApJS, 76, 1001

Rappaport S., Vanderburg A., Nelson L., Gary B. L., Kaye T. G., Kalomeni B., Howell S. B., Thorstensen J. R., Lachapelle F.-R., Lundy M., St-Antoine J., 2017, MNRAS, 471, 948

Rebassa-Mansergas A., Ren J. J., Parsons S. G., Gänsicke B. T., Schreiber M. R., García-Berro E., Liu X.-W., Koester D., 2016, MNRAS, 458, 3808

Rodrigo C., Solano E., Bayo A., , 2012, SVO Filter Profile Service Version 1.0, IVOA Working Draft 15 October 2012

Roming P. W. A., Hunsberger S. D., Gronwall C., Nousek J. A., Breeveld A. A., Mason K. O., UVOT PSU Team UVOT MSSL Team UVOT SwRI Team 2004, in American Astronomical Society Meeting Abstracts Vol. 36 of Bulletin of the American Astronomical Society, The Swift Ultra-Violet/Optical Telescope. p. 1612

Savoury C. D. J., Littlefair S. P., Dhillon V. S., Marsh T. R., Gänsicke B. T., Copperwheat C. M., Kerry P., Hickman R. D. G., Parsons S. G., 2011, MNRAS, 415, 2025

Scaringi S., Maccarone T. J., D'Angelo C., Knigge C., Groot P. J., 2017, Nature, 552, 210

Schmidt G. D., Szkody P., Silvestri N. M., Cushing M. C., Liebert J., Smith P. S., 2005, ApJL, 630, L173

Schmidt S. J., Cruz K. L., Bongiorno B. J., Liebert J., Reid I. N., 2007, AJ, 133, 2258

Schmidt S. J., Hawley S. L., West A. A., Bochanski J. J., Davenport J. R. A., Ge J., Schneider D. P., 2015, AJ, 149, 158

Schneider D. P., Greenstein J. L., Schmidt M., Gunn J. E., 1991, AJ, 102, 1180

- Schwöpe A. D., Brunner H., Hambaryan V., Schwarz R., 2002, in Gänsicke B. T., Beuermann K., Reinsch K., eds, *The Physics of Cataclysmic Variables and Related Objects* Vol. 261 of *Astronomical Society of the Pacific Conference Series*, LARPs – Low-accretion rate polars. p. 102
- Schwöpe A. D., Christensen L., 2010, *A&A*, 514, A89
- Schwöpe A. D., Staude A., Koester D., Vogel J., 2007, *A&A*, 469, 1027
- Shipman H. L., 1979, *ApJ*, 228, 240
- Showman A. P., Fortney J. J., Lewis N. K., Shabram M., 2013, *ApJ*, 762, 24
- Showman A. P., Lewis N. K., Fortney J. J., 2015, in *AAS/Division for Extreme Solar Systems Abstracts* Vol. 3 of *AAS/Division for Extreme Solar Systems Abstracts*, Atmospheric circulation of warm and hot Jupiters: effect of nonsynchronous rotation and stellar irradiation. p. 400.01
- Sing D. K., Fortney J. J., Nikolov N., Wakeford H. R., Kataria T., Evans T. M., Aigrain S., Ballester G. E., Burrows A. S., Deming D., Désert J.-M., Gibson N. P., Henry G. W., Huitson C. M., Knutson H. A., Lecavelier Des Etangs A., et al., 2016, *Nature*, 529, 59
- Sion E. M., Bond H. E., Lindler D., Godon P., Wickramasinghe D., Ferrario L., Dupuis J., 2012, *ApJ*, 751, 66
- Siverd R. J., Beatty T. G., Pepper J., Eastman J. D., Collins K., Bieryla A., Latham D. W., Buchhave L. A., Jensen E. L. N., Crepp J. R., Street R., Stassun K. G., Gaudi B. S., Berlind P., Calkins M. L., DePoy D. L., Esquerdo G. A., Fulton B. J., et al., 2012, *ApJ*, 761, 123
- Sorahana S., Suzuki T. K., Yamamura I., 2014, *MNRAS*, 440, 3675
- Southworth J., Tappert C., Gänsicke B. T., Copperwheat C. M., 2015, *A&A*, 573, A61
- Spiegel D. S., Burrows A., Milsom J. A., 2011, *ApJ*, 727, 57
- Steehhs D., Howell S. B., Knigge C., Gänsicke B. T., Sion E. M., Welsh W. F., 2007, *ApJ*, 667, 442

Steehgs D., Marsh T., Knigge C., Maxted P. F. L., Kuulkers E., Skidmore W., 2001, ApJL, 562, L145

Steele P. R., et al., 2011, MNRAS, 416, 2768

Steele P. R., et al., 2013, MNRAS, 429, 3492

Stelzer B., de Martino D., Casewell S. L., Wynn G. A., Roy M., 2017, A&A, 598, L6

Sterzik M. F., Pascucci I., Apai D., van der Blik N., Dullemond C. P., 2004, A&A, 427, 245

Sweigart A. V., Greggio L., Renzini A., 1990, ApJ, 364, 527

Szkody P., Anderson S. F., Hayden M., Kronberg M., McGurk R., Riecken T., Schmidt G. D., West A. A., Gänsicke B. T., Nebot Gomez-Moran A., Schneider D. P., Schreiber M. R., Schwope A. D., 2009, AJ, 137, 4011

Szkody P., Henden A., Agüeros M., Anderson S. F., Bochanski J. J., Knapp G. R., Mannikko L., Mukadam A., Silvestri N. M., Schmidt G. D., Stephanik B., Watson T. K., West A. A., Winget D., Wolfe M. A., Barentine J. C., Brinkmann J., et al., 2006, AJ, 131, 973

Szkody P., Mukadam A., Gänsicke B. T., Campbell R. K., Harrison T. E., Howell S. B., Holtzman J., Walter F. M., Henden A., Dillon W., Boberg O., Dealaman S., Perone C. S., 2010, ApJ, 716, 1531

Tappert C., Gänsicke B. T., Schmidtbreick L., Aungwerojwit A., Mennickent R. E., Koester D., 2007, A&A, 474, 205

Tappert C., Gänsicke B. T., Schmidtbreick L., Ribeiro T., 2011, A&A, 532, A129

Tremblay P.-E., Bergeron P., 2009, ApJ, 696, 1755

Tremblay P.-E., Bergeron P., Gianninas A., 2011, ApJ, 730, 128

Uthas H., Knigge C., Long K. S., Patterson J., Thorstensen J., 2011, MNRAS, 414, L85

Vacca W. D., Cushing M. C., Rayner J. T., 2003a, PASP, 115, 389

Vacca W. D., Cushing M. C., Rayner J. T., 2003b, PASP, 115, 389

- Vanderburg A., Johnson J. A., Rappaport S., Bieryla A., Irwin J., Lewis J. A., Kipping D., Brown W. R., Dufour P., Ciardi D. R., Angus R., Schaefer L., Latham D. W., Charbonneau D., Beichman C., Eastman J., et al., 2015, *Nature*, 526, 546
- Vanlandingham K. M., Schmidt G. D., Eisenstein D. J., Harris H. C., Anderson S. F., Hall P. B., Liebert J., Schneider D. P., Silvestri N. M., Stinson G. S., Wolfe M. A., 2005, *AJ*, 130, 734
- Vernet J., et al., 2011, *A&A*, 536, A105
- von Hippel T., Kuchner M. J., Kilic M., Mullally F., Reach W. T., 2007, *ApJ*, 662, 544
- Webbink R. F., Wickramasinghe D. T., 2005, in Hameury J.-M., Lasota J.-P., eds, *The Astrophysics of Cataclysmic Variables and Related Objects Vol. 330 of Astronomical Society of the Pacific Conference Series, A Model for Low Accretion Rate Polars*. p. 137
- Weights D. J., Lucas P. W., Roche P. F., Pinfield D. J., Riddick F., 2009, *MNRAS*, 392, 817
- Wheatley P. J., Ramsay G., 1998, in Howell S., Kuulkers E., Woodward C., eds, *Wild Stars in the Old West Vol. 137 of Astronomical Society of the Pacific Conference Series, EF ERI in a low accretion state*. p. 446
- Wood J. H., Saffer R., 1999, *MNRAS*, 305, 820
- Wyatt M. C., Farihi J., Pringle J. E., Bonsor A., 2014, *MNRAS*, 439, 3371
- Xu S., Jura M., Dufour P., Zuckerman B., 2016, *ApJL*, 816, L22
- York D. G., Adelman J., Anderson Jr. J. E., Anderson S. F., Annis J., Bahcall N. A., Bakken J. A., Barkhouser R., Bastian S., Berman E., Boroski W. N., Bracker S., Briegel C., Briggs J. W., Brinkmann J., Brunner R., Burles S., Carey L., et al., 2000, *AJ*, 120, 1579